UCLouvain

École polytechnique de Louvain

Thermodynamic and operational analysis of small-scale Brayton cycle based Carnot batteries

Authors: **Thomas Gallez, Thibault Servais**
Supervisor: **Francesco Contino**
Readers: **Yann Bartosiewicz, Antoine Laterre**
Academic year 2022–2023
Master [120] in Mechanical Engineering and Master [120] in Electro-mechanical Engineering

ABSTRACT

In the era of energy transition, there is an increasing need for electricity storage technology. A technology that has been drawing attention for the past few years is the Brayton cycle based pumped thermal electricity storage (PTES). Currently, the research on the thermo-economics of large-scale Brayton PTES systems is relatively well-developed. However, in the context of small-scale applications (i.e., less than 1 MW), the research is still limited and lacking. This thesis focuses on studying the thermodynamic and operational performance of small-scale packed bed Brayton PTES. The research starts with the development and validation of a thermodynamic model. An analysis of the system transient behavior over a charge/discharge cycle is carried out. The round trip efficiency of the reference design is found to be 32.7 %. A parametric analysis is then performed as well as an uncertainty quantification. The operational limits and control strategies of the packed bed PTES are discussed, and solutions for extending the operating time at rated power are proposed. Incomplete charge cycles are also studied. The difficulties of establishing an economic analysis are discussed, highlighting the need for further investigation. Overall, this thesis provides insights into the thermodynamic and operational performance of small-scale packed bed Brayton PTES systems, contributing to the development of packed bed PTES as an alternative solution for other small-scale electrical energy storage.

ACKNOWLEDGMENTS

We would like to express our gratitude to our supervisor, Prof. Francesco Contino, for his availability and guidance in teaching us effective scientific communication. His expertise and insights have greatly contributed to our learning and development in this field.

Thanks also go to our assistant, Antoine Laterre, for his numerous advice, and numerous proofreadings. His dedication and support have been very appreciated.

We would like to express our appreciation to Arnaud Gallez and Manon Wouters for their meticulous proofreading and their encouragement throughout the writing process of this master thesis.

We are also grateful to Bastien Massion, PhD student at the ICTEAM, for his valuable advice regarding the numerical implementation of the packed bed reservoir model.

We would also like to acknowledge our respective parents for their unwavering support and encouragement throughout our studies.

Lastly, we would like to extend our thanks to Victor Anciaux and Benoit Schoeps for their moral support during the process of writing this thesis. Their encouragement and positivity have been a source of motivation.

CONTENTS

Introduction **1**

1 Literature Review **4**
1.1 Rankine cycle based PTES 6
1.2 Brayton cycle based PTES 7
1.2.1 Molten Salts PTES (LBPTES) 8
1.2.2 Packed-bed PTES (SBPTES) 10
1.2.3 Ecologic aspect 11

2 Thermodynamic model **12**
2.1 Packed bed PTES general layout and characteristics 12
2.2 Models of the components 16
2.2.1 Packed bed reservoirs 16
2.2.2 Compressors 22
2.2.3 Expanders 22
2.2.4 Off-design model of the machines 23
2.2.5 Heat exchangers 24

3 Cyclic behavior analysis **26**
3.1 Performance metrics 26
3.2 Reference design 27
3.3 Cyclic transient behavior 30
3.3.1 Thermal inertia behavior in the reservoirs 30
3.3.2 Cyclic behavior 32
3.4 Exergy analysis of the reference design 36
3.4.1 Exergy analysis of the heat pump cycle 38
3.4.2 Exergy analysis of the packed bed heat transfer 38

3.4.3 Exergy analysis of the heat engine cycle 39

4 Parametric analysis **40**
4.1 Temperatures 41
4.2 Isentropic efficiency impact on the roundtrip efficiency 46
4.3 Compression ratios 47
4.4 Parametric analysis on the reservoirs design parameters 48
4.4.1 Length-to-diameter ratio impact on the heat transfer 50
4.4.2 Length-to-diameter ratio impact on the round trip efficiency 51
4.4.3 Impact of the particle diameter on the heat transfer 53
4.4.4 Impact of the particle diameter on the round trip efficiency . 55
4.5 Choice of working fluid 56
4.6 Uncertainty Quantification 57
4.6.1 Uncertainty analysis on the packed bed heat transfer 58
4.6.2 Uncertainty analysis on the round trip efficiency 61

5 Operational considerations **64**
5.1 Power limitations related to operating conditions 65
5.2 Constant power cyclic behavior 67
5.3 Design parameters to improve output stability 71
5.3.1 Oversizing the reservoirs 71
5.3.2 Length-to-diameter ratio of the reservoirs 72
5.4 Constant compressor outlet temperature during charge 74
5.4.1 Varying the compression ratio 74
5.4.2 Including the LPHX in the charging loop 78
5.5 Incomplete charge capabilities 81
5.6 Conclusions about operational considerations 83

6 Economic discussion **85**
6.1 Point of view of the literature 85
6.2 Point of view of the thermodynamic analysis 86

Conclusion **88**

Appendices **98**

A Performance map for the CST-T2-β case **99**

NOMENCLATURE

Acronyms

CB Carnot Battery

CDF Cumulative Density Function

CMFR Constant Mass Flow Rate

COP Coefficient Of Performance

CPWR Constant Power

CR Cold Reservoir

CSP Concentrated Solar Power

EES Electrical Energy Storage

ER Electrical Resistance

HE Heat Engine

HP Heat Pump

HPHX High Pressure Heat Exchanger

HR Hot Reservoir

HT High Temperature

HTF Heat Transfer Fluid

L/D Length-to-Diameter

LPHX Low Pressure Heat Exchanger

LT Low Temperature

MS Molten Salts

ORC Organic Rankine Cycle

OVS Oversize factor

PDE Partial Derivative Equation

PDF Probability Density Function

PHES Pumped Heat Energy Storage

PHS Pumped Hydro Storage

PTES Pumped Thermal Energy Storage

PV Photovoltaic

SOC State Of Charge

TES Thermal Energy Storage

UQ Uncertainty Quantification

INTRODUCTION

Electrical energy storage (EES) has always been an important issue since electricity has to rely on another vector to be stored. On a large scale, Pumped Hydro electricity Storage (PHS) has long been the most economical and flexible solution for storing large amounts of electricity [1]. However, with the growing demand for electricity and the recent development of intermittent energies, the demand for storage capacity has exploded [2]. In view of the geographical constraints necessary for PHS technology, other types of storage have started to be studied [3].

According to the definition proposed by Luo et al. [4]: "Electrical Energy Storage (EES) refers to a process of converting electrical energy from a power network into a form that can be stored for converting back to electrical energy when needed". EES systems can thus implement different type of energy transformations, as shown on fig. 1.

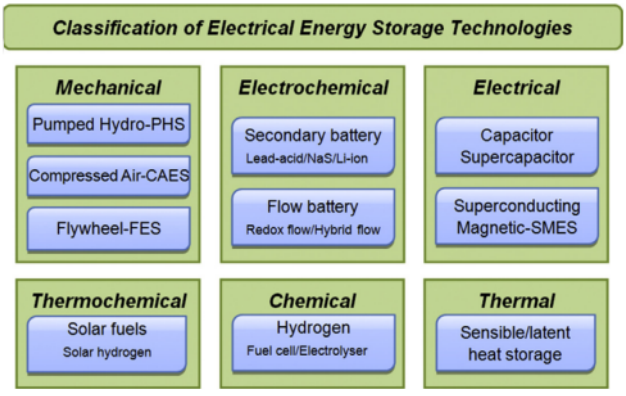

Figure 1: EES by type of intermediate form of energy from [4].

Pumped Thermal Energy Storage (PTES), also known as Carnot Battery, is among the various electrical energy storage technologies that have gained increased attention in the pursuit of alternative solutions.

PTES are thermal batteries that use heat storage as an energy carrier.
They are currently under development and their target application is mainly for large scale [5], for example for the management and regulation of wind farms or large photovoltaic power plants. PTES are among the technologies that do not have a lot of physical constraints and are easily scalable [6].

They can be broken down into two main families based on the thermodynamic cycles that they employ: Rankine PTES and Brayton PTES [7]. For small-scale applications (under 1 [MW] of peak power), Rankine-based Carnot batteries have already been investigated with existing machines as done by Staub et al. [8].
Although some demonstrators have been built [9, 10], Brayton cycle based Carnot batteries have yet to prove their technical, operational and economical feasibility at all scales[11]. As it is explained more in detail in the literature review of the following chapter, they can be divided into two main categories based on the thermal energy storage media employed: those employing a liquid media (typically molten salts) and those employing a solid media, typically reservoirs filled with a packed bed of solid material. For small-scale applications (i.e., rated power below 1 [MW]), packed bed PTES could be preferred due to the very high cost per installed kilowatt of molten salts PTES at small scale [12]. This thesis therefore focuses on the packed bed Brayton PTES systems. Its objective is to study their thermodynamic and operational characteristics on a small scale to understand the ins and outs of their development.

This thesis focuses on the the following research question:

What thermodynamic and operational performance can be expected from small-scale packed bed Brayton PTES systems? What are the key parameters influencing their performance?

The structure is as follows:

- A review of the literature on PTES technology.
- A presentation and validation of the thermodynamic model used to study the performance of Brayton PTES with packed-bed storage.
- A study of the system behavior and performance over a complete charge/discharge cycle.

- A parametric analysis as well as an uncertainty analysis about the impact of the different parameters on the system performance.
- The operational considerations about power limitations of the system.
- A discussion on the economic aspect of the packed bed PTES technology.

CHAPTER 1

LITERATURE REVIEW

The PTES concept is not new. In fact, Marguerre proposed the idea of combining a heat engine and a heat pump to store energy, as early as 1924 [13].

However, it is only recently that the literature has started to shift its focus towards studying PTES, exploring their potential for widespread utilization. The number of researches about them has then strongly increased in the last few years as shown on fig. 1.1.

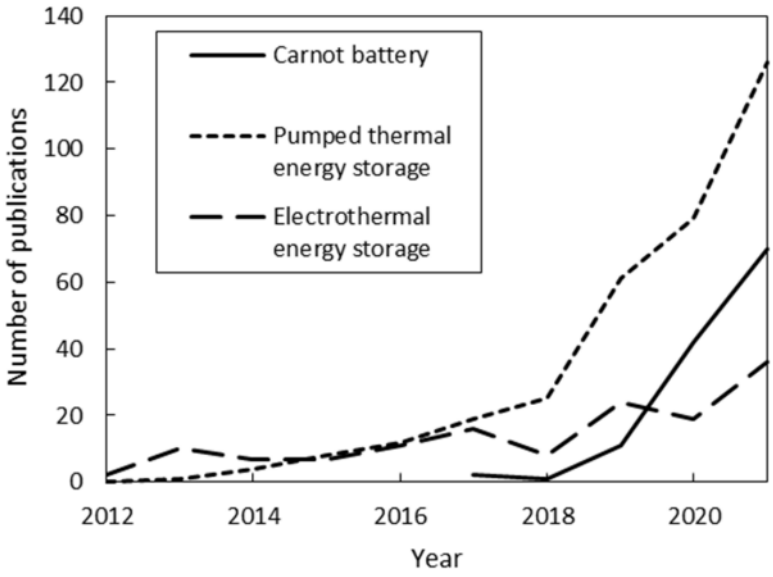

Figure 1.1: Number of publications on PTES over the past decade from [11].

The operating principle of PTES is shown on fig. 1.2. In a PTES, the electric energy is stored as thermal energy. The electric input is used to create a temperature difference between a low temperature (LT) and a high temperature (HT) reservoirs by means of a heat pump. In order to get an electrical output, the heat flow from the HT reservoir to the LT reservoir powers a heat engine which converts it into work and discharges the residual heat into the LT reservoir. Different subcategories of Pumped Thermal Energy Storage (PTES) can be determined by the choice of storage materials and the type of thermodynamic cycles employed.

Two main categories of PTES exist, those based on Rankine cycles and those based on Brayton cycles. In addition to using different thermodynamic cycles, they differ in the working fluids used and the materials employed for heat storage. Cycle temperature ranges are therefore determined by the machines, the working fluid and the storage materials utilized. Fig. 1.3 shows the possible temperature ranges, based on their different usage constraints, for different materials and for certain combinations of fluid and cycle.

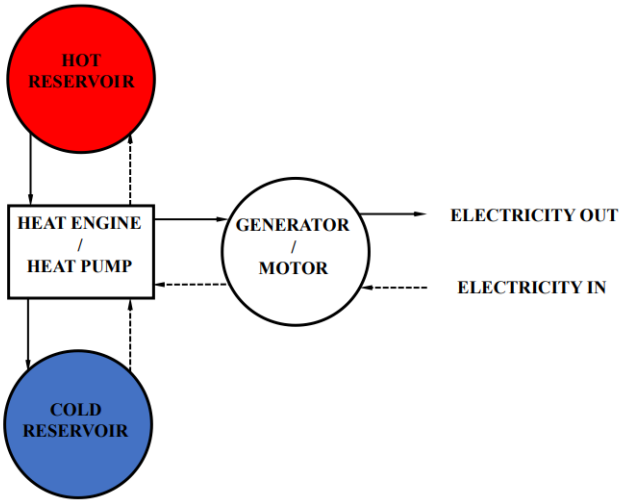

Figure 1.2: PTES principle from [14]

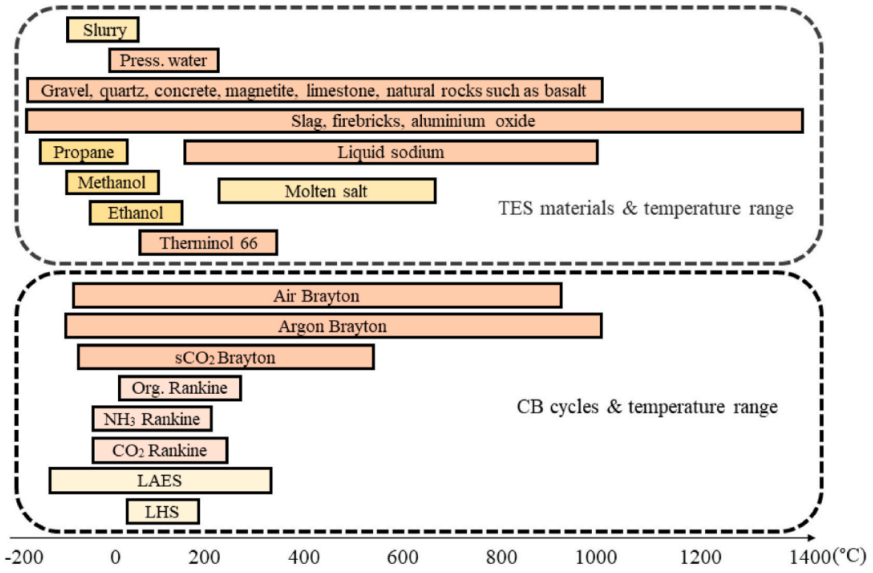

Figure 1.3: Thermal storage material and PTES cycles temperature ranges from [6].

1.1 Rankine cycle based PTES

Rankine based PTES is mostly based on steam Rankine cycle, Organic Rankine Cycle (ORC), super-critical and trans-critical CO2 cycles [7]. They operate with latent heat and sensible heat. The operating principle and the T-s diagrams related to the charge and discharge cycles are shown on fig. 1.4.
The Rankine PTES is characterized by a cycle where the working fluid undergoes a phase change. It can thus store both sensible and latent heat and operates within a narrower temperature range than Brayton PTES (generally under 200 [°C] instead of above 500 [°C] for Brayton [7]). Due to this low-temperature application, coupling with waste heat recovery can easily be envisaged [7].

During charging, the low pressure fluid is first evaporated ($1 \rightarrow 2$) before being compressed ($2 \rightarrow 3$). It then releases its latent and sensible heat to the hot reservoir ($3 \rightarrow 5$) before being expanded in the turbine and regaining its low pressure ($5 \rightarrow 1$).

During the discharge the fluid is pumped up to high pressure ($1' \rightarrow 2'$) and recovers sensible and latent heat from the hot tank ($2' \rightarrow 4'$). It is then expanded in the turbine before being condensed and returning to its saturated liquid state ($5' \rightarrow 1'$). Round trip efficiency of Rankine PTES vary from 40 [%] to 70 [%] [6].
Concerning the thermal energy storage system, if the heat is absorbed from

and rejected to the cold storage at a constant temperature, like in supercritical CO2 systems, then a phase change material, storing both latent and sensible heat, may be suited [7]. If the heat is absorbed from and rejected to the hot reservoir with a significant temperature glide, then a sensible liquid heat storage like water or pressurized water may be used [7, 6]. Table 1.1 presents some Rankine PTES designs and models from the literature.

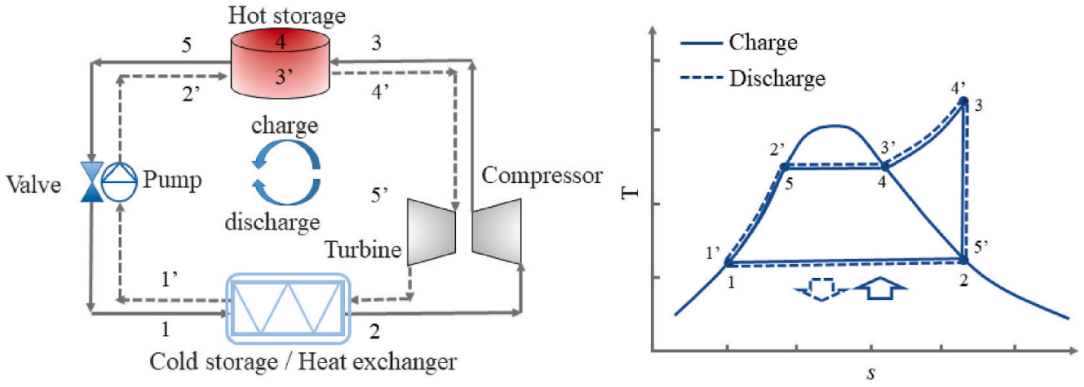

Figure 1.4: Rankine cycle based PTES and corresponding T-s diagram from [6].

Power/Capacity (MW/MWh)	Fluid	Hot/Cold Storage	Roundtrip efficiency [%]	Author and source
–/–	CO_2	Pressurized water/Ice slurry	60	M. Morandin et al., 2012 [15]
0.09/0.45	CO_2	Pressurized water/Ice slurry	67–75	Y.M. Kim et al., 2013 [16]
50/200	CO_2	Hot water/Ice slurry	51–65	M. Mercangoz et al., 2012 [13]
1/10	CO_2	Ground heat exchanger/Ice slurry	42–55	F. Ayachi et al., 2016 [17]
1/8	NH_3/CO_2	Therminol 66/Ice slurry	42–55	W.D. Steinmann., 2014 [18]

Table 1.1: Rankine PTES designs from the literature.

1.2 Brayton cycle based PTES

Brayton based PTES are usually made of a heat pump, a heat engine and two sensible heat thermal reservoirs. During the charging phase, the battery operates an inverse Brayton cycle. During the discharging mode, it operates a direct Brayton cycle.
Brayton-based PTES are generally working with a supercritical gas as the working fluid. The most common ones are argon and air. However, other fluids as helium, hydrogen and nitrogen have also been studied. In Brayton based PTES, the working fluid is not subject to a phase change. Therefore, to carry the same amount of heat as Rankine PTES, they work with important temperature differences (from 500 to over 1000 [°C] [6]).

There are two major types of Brayton based PTES based on the type of storage material used: liquid or solid. Liquid Brayton PTES (LBPTES) store sensible heat in a liquid media, usually molten salts, and use cryogenic fluids (e.g. methanol or hexane) for the cold storage. Solid Brayton PTES (SBPTES) store sensible heat in a solid media. These two types of Brayton PTES are presented in more detail in the following sections. Phase change materials can also be used but are not very present in the literature [19][20].

Table 1.2 summarizes some Brayton PTES models from the literature. As it can be seen, the range of round trip efficiency (26.9-85 [%]) is wide.

Power/Capacity (MW/MWh)	Fluid	Hot/Cold Storage	Roundtrip efficiency [%]	Author and source
100/600	Argon	Refractory material	66.7	Desrues et al., 2010 [21]
2/16	Argon	Particulated granite	72	Howes et al., 2012 [9]
2/16	Argon	Packed Fe_3O_4 pebbles	50–85	McTigue et al., 2015 [22]
-/-	Nitrogen	Molten salt and N-hexane / N-hexane	50–85	Laughlin et al., 2017 [23]
4/12	Air	Aluminium oxide spheres	26.9	Benato et al., 2018 [24]
4/12	Helium	Basalt	56.9	Wang et al., 2019 [25]
–/2	Nitrogen	Magnetite pebbles	57.4	Wang et al., 2019 [26]
2/16	Argon	Magnetite pebbles	40–53	Sapin et al., 2020 [27]
100/1000	Argon	Gravel	59–65	Davenne et al., 2020 [28]

Table 1.2: Brayton PTES designs from the literature.

1.2.1 Molten Salts PTES (LBPTES)

Molten salts PTES employs two pairs of tanks for the thermal storage (one for the hot storage and one for the cold storage), two pairs of compressors/expanders (one for the heat pump and one for the heat engine) as they operate at very different inlet temperatures [29] and heat exchangers. The heat exchanges are used to exchange heat between the working fluid and the storage medias or with the environment. A recuperator can also be included, allowing to increase the round trip efficiency and reduce the pressure ratios [29]. Fig. 1.5 shows the two different layouts, with or without recuperator.

During the charging phase, the working fluid is first compressed in order to reach a high temperature. It then exchanges heat with the hot storage media, the latter flowing from a colder temperature tank to a hot temperature one. The fluid is then expanded before gaining heat from the cold storage by flowing through the cold heat exchanger. In a similar yet opposite way as the hot storage, the cold storage media flows from the hotter to the colder tank in the process. In the discharging phase, the inverse cycle takes place. The state of charge of the system is characterized by the filling of the tanks.

Concerning the hot storage material, nitrate molten salts are the most common choice although chloride salts have also been studied [12]. In order to remain in

a liquid state, molten salts have to remain above their freezing temperature. For nitrate molten salts, this freezing temperature is usually located in the 200-300 [°C] range [30]. Molten salts are also limited by their degradation temperature, above which their thermal stability starts degrading. For nitrate molten salts, this temperature is in the 500-600 [°C] range while it can exceed 800 [°C] for chloride molten salts [30]. As the cold temperature of the hot storage has to remain above the salt's freezing temperature, the turbine work output becomes a significant fraction of the compression work, limiting the round trip efficiency of the system to about 35-40 [%] [12, 29]. Adding a recuperator transferring heat between the high- and low-pressure streams of the working fluid allows to solve this problem. The T-S diagrams corresponding to both configurations, with or without recuperator are shown on fig. 1.6.

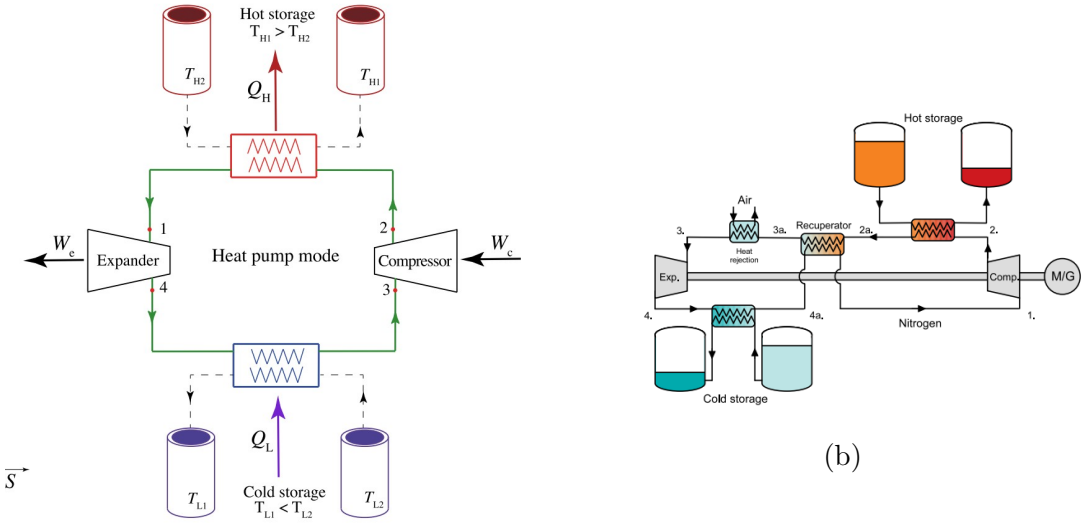

Figure 1.5: Schema of (a) Molten salts PTES during charge from [30] (b) Molten salts PTES with recuperator from [29]

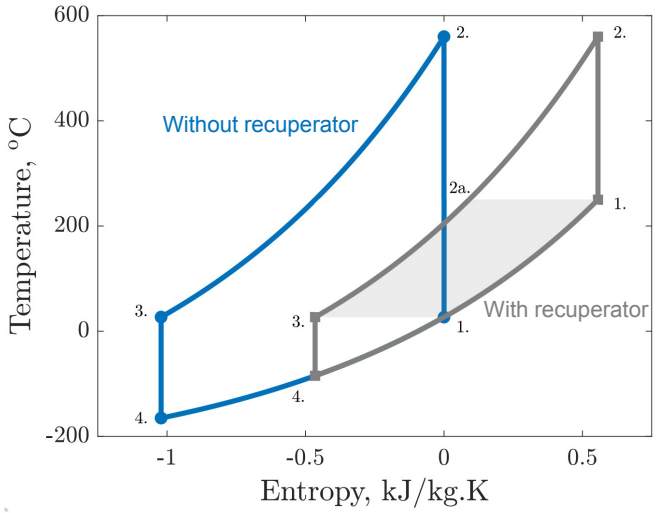

Figure 1.6: T-S diagrams comparison for reversible cycle: MS without recuperator, MS with recuperator (shading indicates recuperative heat transfer) from [29].

1.2.2 Packed-bed PTES (SBPTES)

Packed-bed PTES is the other most common technology for Brayton cycle-based PTES. It relies on vertical reservoirs filled with packed beds of solid material to store the thermal energy. The solid material used is often stone (e.g. basalt), but it can also employ other materials such as gravel or aluminum oxides. [31] Inside the reservoirs, the working fluid heats the solid by convective heat transfer. This solid stores the heat lost by the fluid, but not evenly throughout the reservoir. As the fluid gradually loses heat, it will heat the next layers of the reservoir less, resulting in a stratified temperature distribution inside the reservoirs. The reservoirs therefore contain a hot zone, a cold zone and a zone with a temperature gradient, known as the thermocline. All of this is described more in detail in chapter 2.
The profile of the thermocline will change during charging and discharging, and will move within the tanks. The tanks outlet temperatures will therefore vary during the cycle, making the operation of the system complex.
This particular type of storage means that only two tanks can be used, instead of four for molten salts storage.

As Frate et al. [12] suggests, packed-bed PTES seems to be the technology most likely to be interesting for small-scale applications from a techno-economic point of view compared to molten salts PTES.

1.2.3 Ecologic aspect

Oro et al. [32] investigated the environmental impact of each storage technology and detailed for each of them the quantity of each material required and its impact based on the EcoIndex 99 [33].
Their conclusions are clear, the packed-bed technology has the lowest environmental impact due to its simplicity, while the molten salts technology has the highest impact because it requires more materials and more complex equipment.
The overall impact per kilowatt-hour is, in the scenario with the largest temperature difference, 0.15 points for the packed bed and 5.67 for the molten salts. From their analysis we can see that the Molten Salts represent almost 94 [%] of the environmental balance for this technology. Wickramasinghe et al. [34] and Nahhas et al. [35] share the same conclusion that packed-bed technology has a significantly lower environmental impact compared to molten salts.

CHAPTER 2

THERMODYNAMIC MODEL

In this chapter, the layout and detailed operating principle of the Brayton-based packed bed PTES is presented. The numerical modeling of each component of the system is explained and a sensitivity analysis on the numerical parameters of the model is carried out.

2.1 Packed bed PTES general layout and characteristics

The general layout of the packed bed Brayton-based PTES is shown on fig. 2.1. The main components are the two packed bed reservoirs, one for the hot side (HR) and one for the cold side (CR), a pair of compressor and expander for the heat pump (HP) cycle and one for the heat engine (HE) cycle (so four machines in total), two heat exchangers, one on the high pressure side (HPHX) and one on the low pressure side (LPHX). A fan and an electrical resistance are also present for the initialization of the system. They are used to warm the HR and the CR at the desired temperatures. The buffer vessel and auxiliary compressor are present to store/release gas and adjust the pressure and mass flow rate in the system during the charge and discharge processes. The role and numerical modeling of each of these components is explained more in detail in this chapter.

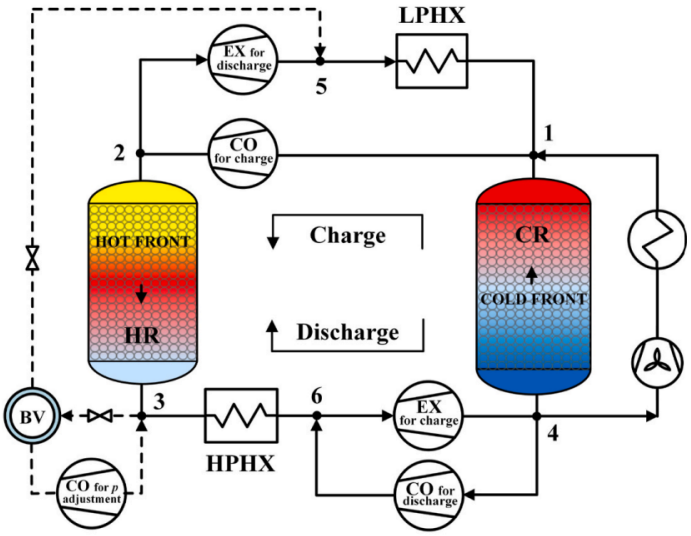

Figure 2.1: Layout of a Brayton-based PTES with packed-bed storage from [36].

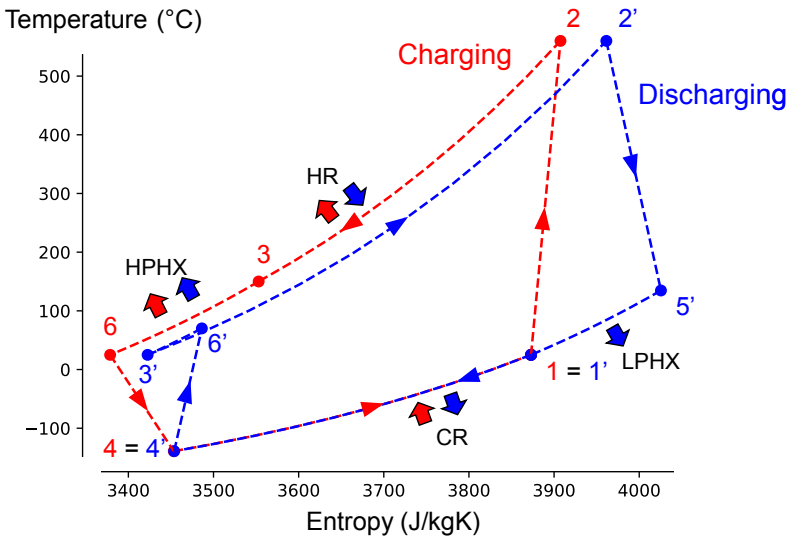

Figure 2.2: T-s diagram with argon as working fluid during charge (HP) and discharge (HE) of a Brayton based PTES system with packed bed storage. The numbered states correspond to the system presented on fig. 2.1. The red and blue arrows indicate a heat flux to/from a packed bed reservoir or the ambient in the case of the HPHX and LPHX during charge and discharge respectively.

Fig. 2.2 shows the temperature-entropy diagram of the charging and discharging cycles of the packed bed PTES. During the charging process (HP cycle), the working fluid is first compressed from the initial temperature of the CR to a high-temperature and high-pressure state (shown as $1 \rightarrow 2$ on the T-s diagram). It then flows through the HR, rejecting heat to the packed bed material and therefore displacing the thermal front inside it ($2 \rightarrow 3$). The heat exchange between the fluid and the packed bed material and the resulting temperature profiles inside the reservoirs are described more in detail later in this section. The residual heat is then evacuated through the HPHX ($3 \rightarrow 6$). Some designs also consider a layout without the HPHX in the HP cycle [37]. The fluid is then expanded to a low-pressure and low-temperature state through the expander ($6 \rightarrow 4$). It finally flows through the CR to come back to its initial state (state 1), absorbing heat from the packed bed material and therefore displacing the thermal front in the CR.

During the discharging process (HE cycle), the working fluid goes from its initial state to a low-temperature state by flowing through the CR, rejecting heat to the packed bed material ($1' \rightarrow 4'$). After being compressed to a higher temperature and high-pressure state ($4' \rightarrow 6'$), the heat generated by the irreversibilities of the compression is rejected to the environment through the HPHX ($6' \rightarrow 3'$). This also allows to control the inlet temperature of the fluid in the HR. The fluid then flows through the HR, absorbing heat from the packed bed material and exiting the HR at a high-temperature state ($3' \rightarrow 2'$). After being expanded to a low-pressure state ($2' \rightarrow 5'$), it returns to its initial state by flowing through the LPHX ($5' \rightarrow 1'$).

The packed bed reservoirs are vertical pressurized vessels filled with a packed bed of pebbles, storing energy in the form of sensible heat. A part of the volume is occupied by the solid material whereas the rest of the volume (the void fraction ϵ) is occupied by the moving fluid. In these reservoirs, the temperature is not uniformly distributed but presents a stratified temperature distribution along the lenght axis as shown on fig. 2.3. Three main zones can be identified: a hot zone where the temperature is almost uniformly hot, a cold zone where the temperature is almost uniformly cold and a thermocline region in between the hot and the cold zones where a temperature gradient makes the transition between the hot and the cold zones. In the hot and cold zones, the temperatures of the fluid and the solid material can be considered equal whereas in the thermocline zone there is a temperature difference between the fluid and the solid. It is in this thermocline zone that the heat transfer between the fluid and the solid occurs. During the charging/discharging of a reservoir, the convective heat transfer between the fluid and the solid material results in a displacement of the thermocline towards the cold/hot zone. Fig 2.4 shows the evolution of the fluid and solid temperature profiles during a charging/discharging process.

In these reservoirs, there is a direct contact between the working fluid and the solid material. Some designs considering an indirect heat exchange, with a heat exchanger between the working fluid and the fluid going through the packed bed reservoir have also been proposed [38, 39], showing that a PTES system with an indirect heat exchange could present lower installation cost than the direct PTES system when its electricity storage duration exceeds 6h. However, the indirect configuration leads to more exergy losses due to the additional heat exchangers, therefore degrading the round trip efficiency [38].

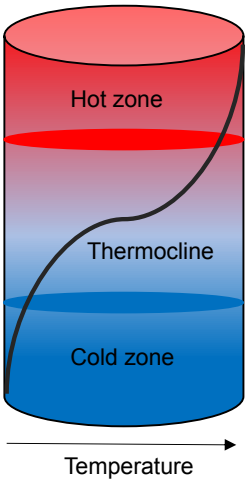

Figure 2.3: Temperature profile inside a packed bed reservoir.

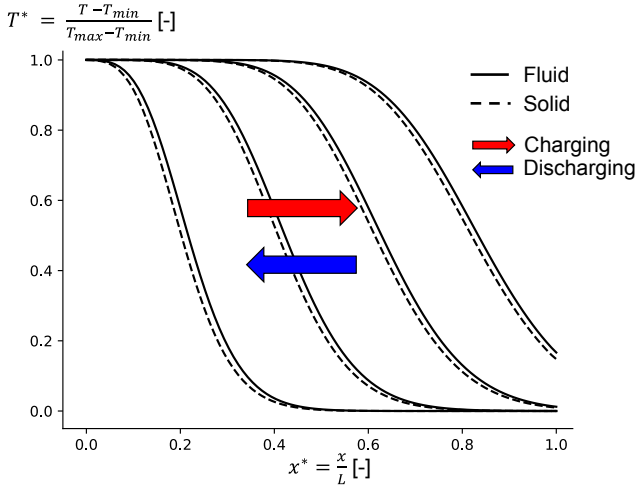

Figure 2.4: Evolution of the fluid and solid temperature profiles and displacement of the thermocline in a packed bed reservoir for a charging or discharging process.

An important aspect of packed bed PTES is their unsteady behavior while in operation. As the charging and discharging processes take place, the temperature profiles inside the reservoirs evolve, resulting in evolving fluid temperatures at the outlet of the reservoirs (as it can be seen on fig. 2.4). The operating conditions and therefore the performances of the HP and HE cycles thus vary throughout the charging and discharging processes. This transient behavior of the system during its operation is presented in chapter 3 about the cyclic behavior of the system.

2.2 Models of the components

2.2.1 Packed bed reservoirs

The following section details the model developed to simulate the packed bed reservoirs temperature profiles and the heat transfer occurring inside them.

The packed bed reservoirs are modeled as well-insulated cylindrical tanks (losses to the environment are therefore neglected) [36]. In order to solve the temperature profiles of the solid packed bed material and the fluid, the 1D Schumann model is considered. It consists of two coupled PDEs, one for the fluid phase (eq. 2.1) and one for the solid phase (eq. 2.2)[25]:

$$\frac{\partial T_f}{\partial t} + \frac{G}{\rho_f \epsilon}\frac{\partial T_f}{\partial x} = \frac{h_v}{\rho_f c_{pf} \epsilon}(T_s - T_f) \tag{2.1}$$

where ρ_f is the fluid density, c_{pf} is the fluid specific heat capacity at constant pressure, G the mass flow rate per unit area (defined at eq. 2.7), ϵ the void fraction (defined at eq. 2.5), h_v the volumetric heat transfer coefficient (defined at eq. 2.3) and T_s, T_f are respectively the temperature of the solid and the fluid.

$$\frac{\partial T_s}{\partial t} = \frac{h_v}{\rho_s c_s (1-\epsilon)}(T_f - T_s) + \frac{k_{s,eff}}{\rho_s c_s (1-\epsilon)}\frac{\partial^2 T_s}{\partial x^2} \tag{2.2}$$

where ρ_s is the solid density, c_s the solid specific heat capacity and $k_{s,eff}$ is the solid effective thermal conductivity (defined at eq. 2.6).

The assumptions of this model are the following:

- 1D Newtonian plug flow (condition: $\frac{D}{d_p} \geq 40$ [-] , with D being the reservoir diameter and d_p the particle diameter) [40].
- Heat transfer occurs based only on the temperature difference between the solid and the gas, and by conduction along the solid material.
- The temperature gradient in the radial direction is negligible [36].

- The heat losses through the well-insulated wall are negligible [25].
- Radiation heat transfer is neglected, as justified by the temperature level [40].

The volumetric heat transfer coefficient h_v is calculated based on the heat transfer coefficient α_p ,the void fraction ϵ and the solid particle diameter d_p [40]. The heat transfer coefficient α_p is computed with the correlation of Coutier and Farber [40, 41] and the correlation for the void fraction ϵ is taken from Zhang et al. [36]:

$$h_v = \frac{6(1-\epsilon)\alpha_p}{d_p} \tag{2.3}$$

$$\alpha_p = \frac{700}{6(1-\epsilon)} G^{0.76} d_p^{0.24} \tag{2.4}$$

$$\epsilon = 0.375 + 0.17\frac{d_p}{D} + 0.39\left(\frac{d_p}{D}\right)^2 \tag{2.5}$$

It is important to note that all three parameters depend on the particle diameter d_p. The influence of this parameter is studied more in detail in chapter 3.

The formula for the effective thermal conductivity in the solid phase is taken from Hänchen et al. [40]:

$$k_{s,eff} = \left[\epsilon k_f^{-1} + (1-\epsilon)k_s^{-1}\right]^{-1} \tag{2.6}$$

The mass flow rate per unit area G is defined as the mass flow rate divided by the cross-sectional area of the tank:

$$G = \frac{\dot{m}}{A} \tag{2.7}$$

The fluid properties are taken from the CoolProp library [42].

The packed beds reservoirs are discretized into N layers and eqs. (2.1) and (2.2) are solved using a semi-implicit scheme:

$$\frac{T_{f,i}^t - T_{f,i}^{t-1}}{\Delta t} = \left(\frac{-G}{\rho_f \epsilon}\right)\frac{T_{f,i}^t - T_{f,i-1}^t}{\Delta x} + \frac{h_v}{\rho_f c_f \epsilon}(T_{s,i}^t - T_{f,i}^t) \tag{2.8}$$

$$\frac{T_{s,i}^t - T_{s,i}^{t-1}}{\Delta t} = \frac{h_v}{\rho_s c_s (1-\epsilon)}(T_{f,i}^t - T_{s,i}^t) + \frac{k_{s,eff}}{\rho_s c_s (1-\epsilon)}\frac{T_{s,i+1}^t - 2T_{s,i}^t + T_{s,i-1}^t}{\Delta x^2} \tag{2.9}$$

The boundary conditions are the following; the fluid temperature at the inlet of the tank is considered constant. The solid material temperature gradient at the inlet and outlet of the tank is considered null (zero flux):

$$T_f^t(x=0) = T_f^{t=0}(x=0) \tag{2.10}$$

$$\frac{\partial T_s(x=0)}{\partial x} = \frac{\partial T_s(x=L)}{\partial x} = 0 \tag{2.11}$$

The pressure drop along each layer of length Δx of the discretized reservoir is computed with the Ergun equation [43]:

$$\Delta p_i = \frac{\Delta x G^2}{\rho_{g,i} d_p} \left(1.75 \frac{(1-\epsilon)}{\epsilon^3} + \frac{150(1-\epsilon)^2}{G d_p \epsilon^3} \mu_{g,i} \right) \tag{2.12}$$

The total pressure drop across the packed bed is calculated by summing the pressure drop across each layer:

$$\Delta p = \sum_{i=1}^{n_x} \Delta p_i \tag{2.13}$$

Due to variations of the gas density inside the reservoirs owing to the displacement of the thermocline and the subsequent variation of temperature profiles, a large amount of gas is stored or released in the pore volume of packed beds. This causes an imbalance of mass flow rate between the inlet and the outlet of the reservoirs, described by the following equation:

$$\epsilon \frac{\partial \rho}{\partial t} + \frac{\partial G}{\partial x} = 0 \tag{2.14}$$

The buffer vessel and auxiliary compressor are therefore present to store/release gas and adjust the pressure in the system, balancing the mass flow rate variations in the two packed bed reservoirs. Wang et al. [26] also proposed a self-balancing PTES system without buffer vessel, obtaining a round-trip efficiency 0.12 [%] higher than the buffer vessel balancing PTES system. He also showed that these mass flow variations in the HR represent at most 0.62 [%] of the inflow mass flow rate for a PTES system similar to the one described here. Therefore and for the sake of simplicity, these mass flow variations are neglected and the mass flow rate in the packed bed is assumed constant.

In order to validate this model, we compared it to the experimental results of Hänchen et al. [40]. Results are shown on fig. 2.5. It can be observed that the simulated profiles fit well with the experimental results. Fig. 2.6 shows the relative difference $\delta = \frac{T_{sim} - T_{exp}}{T_{exp}}$ x100 [%] between the simulated temperature and the experimental results. As it can be seen, the maximum relative difference is 10.01 [%] and 88 [%] of the results are in the ± 5[%] range. A possible explanation for this small difference between simulated and experimental temperature can be the

plug flow assumption inherent to our model. In the experimental setup of Hänchen et al., the small size of the reservoir induces a ratio between reservoir diameter and particles diameter $\frac{D}{d_p} = 7.4$ [-]. The plug flow assumption therefore introduces inaccuracies because of wall effects (the plug flow assumption is only valid for $\frac{D}{d_p} \geq 40$ [-] [40], which is the case of the PTES systems analyzed in the following chapters). Hänchen therefore introduces a bypass flow close to the wall to account for this effect. As an approximation, it is assumed that the bypass flow (by-)passes the reservoir without thermally interacting with the packed bed. He achieved good agreement between his numerical model and experimental results with a bypass flow rate equivalent to 15 [%] of the total mass flow rate. We therefore used the same value for the validation of our model. However, due to the differences in the two models, this value could be adapted to find better agreement between our model and the experimental results. Furthermore, most models used to model the temperature profiles in the packed bed reservoirs of PTES systems show similar difference with these experimental results [36, 25, 14].

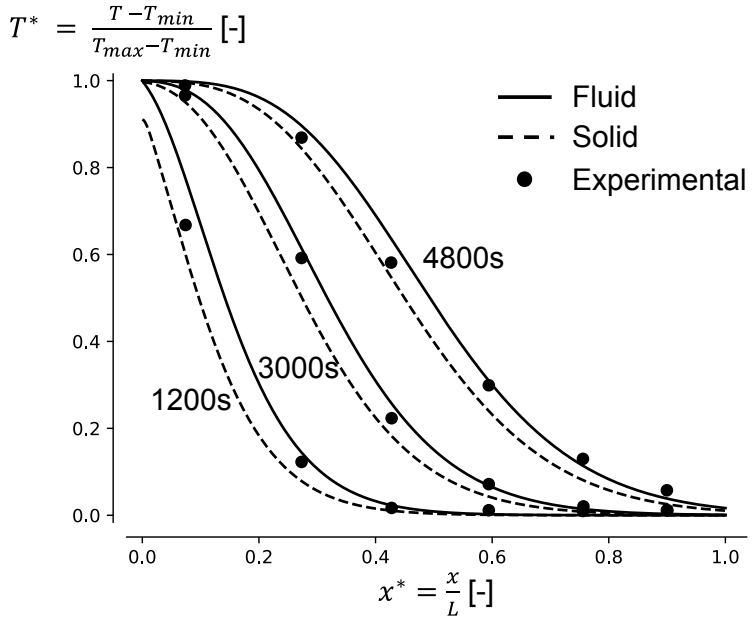

Figure 2.5: Comparison of the fluid and solid temperature profiles in the reservoir with the experimental data from Hänchen et al. [40].

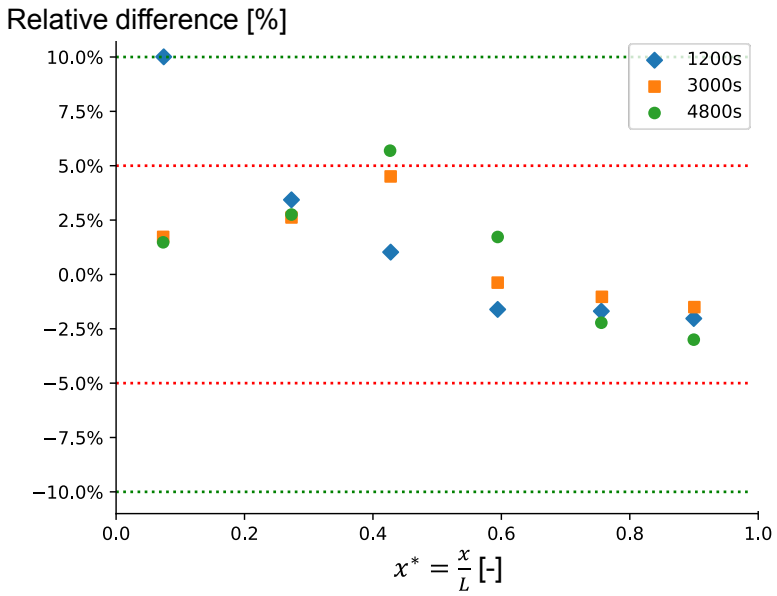

Figure 2.6: Relative difference between the simulated temperature of the model and the experimental results of Hänchen et al. [40]

The spatial step size $\Delta x = \frac{L}{n_x}$ and the time step Δt in eqs. 2.8 and 2.9 both have an influence on the resulting temperature profiles. Fig. 2.7 shows the solid temperature profiles after 4800 seconds of a charging process with the parameters of Hänchen et al. [40], for values of $n_x = \frac{L}{\Delta x}$ ranging from 25 to 400. Fig. 2.8 shows the maximum relative differences of solid temperature and energy stored in the packed bed material when doubling n_x. For values of $n_x \geq 100$, the maximum relative difference in temperature and energy stored when doubling n_x is less than 1 [%]. Therefore, $n_x = 100$ is chosen as the default parameter for further analysis and simulations in order to have relatively low computational times while keeping relatively accurate results.

In the same way as the analysis on the influence of n_x, fig. 2.9 shows the maximum relative difference of temperature and energy stored in the packed bed material between the model with Δt in a range of 0.1 [s] to 240 [s] and the model with $\Delta t = 0.1$ [s]. As it can be seen, in order to keep the relative difference below 1 [%], Δt should be kept below 100 [s].

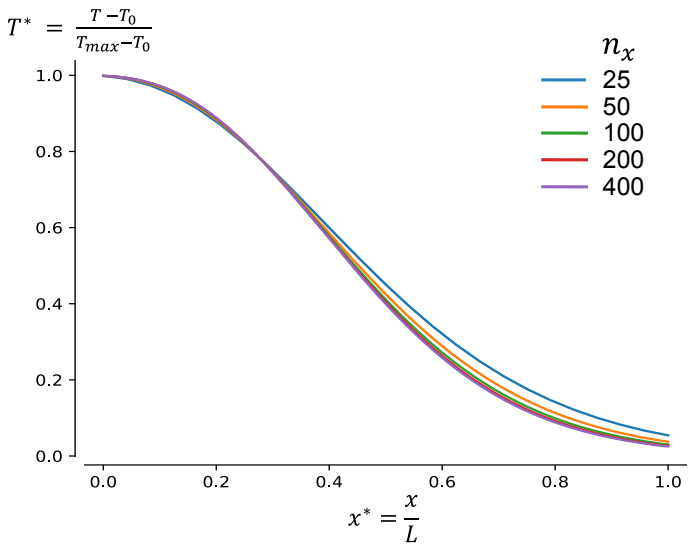

Figure 2.7: Fluid temperature profile in a packed bed reservoir for a charging process with $n_x = 25, 50, 100, 200, 400$ after 4800 [s] with the parameters of Hänchen et al. [40].

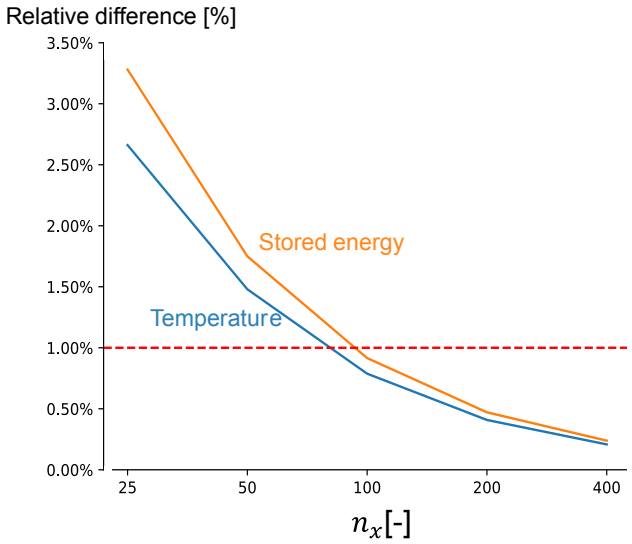

Figure 2.8: Max temperature and stored energy relative difference when doubling n_x.

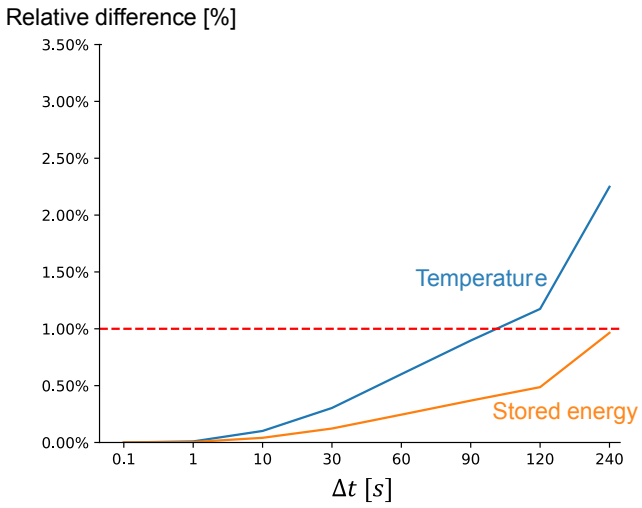

Figure 2.9: Max temperature and stored energy relative difference for different Δt compared with the case with $\Delta t = 0.1$ [s].

2.2.2 Compressors

The compressors are characterized by an isentropic efficiency. The isentropic efficiency is defined in the usual fashion as the ratio between the compression work of an ideal isentropic process and the compression work of the real process.

$$\eta_{isC} = \frac{W_{C,is}}{W_C} = \frac{h_{out,is} - h_{in}}{h_{out} - h_{in}}$$

As it is explained in chapter 4 about the parametric analyses of the system, the isentropic efficiency of the machines has a crucial impact on the round trip efficiency of the system. As is shown, in some operating conditions, an isentropic efficiency lower than 70 [%] would even result in a round trip efficiency of 0 [%]. Hence, our model only considers turbo-machines, as their isentropic efficiency is superior to that of other compressor types (volumetric machines rarely achieve a isentropic efficiency of 70 [%] as explained by Dumont et al. [44]) .

2.2.3 Expanders

The expanders are, alike the compressors, characterized by an isentropic efficiency. For an expander, the isentropic efficiency is defined as the ratio between the expansion work of the real process and the expansion work of the ideal isentropic process.

$$\eta_{isE} = \frac{W_E}{W_{E,is}} = \frac{h_{in} - h_{out}}{h_{in} - h_{out,is}}$$

For the same reason as for the compressors, we only consider turbo-machines for the expanders.

2.2.4 Off-design model of the machines

The system does not always operate at nominal conditions, especially at the start or the end of the charge or the discharge processes as it is shown in the following chapter (section 3.3.2). Therefore, the mass flow rates, compression/expansion ratios, inlet temperatures and pressures of the compressors and the expanders vary according to the operating conditions of the system, resulting in variations of isentropic efficiencies. The off-design model of the machines used to model this variation of the isentropic efficiency is taken from Wang et al. [45] and is the same for both the expanders and compressors. This model is widely used in the literature [25, 36, 38]. A performance map showing the ratio between the isentropic efficiency and the nominal isentropic efficiency $\frac{\eta_{is}}{\eta_{is,nom}}$ for different normalized reduced mass flow rates $\frac{G_c}{G_{cd}}$ (as defined at eq. 2.15) and normalized compression/expansion ratios $\frac{\beta}{\beta_{nom}}$is illustrated on fig. 2.10.

For a given set of operating parameters, the off-design efficiency of a machine is found by solving eqs. 2.15 to 2.19 where β_c is the pressure ratio, n_c is the rotational speed, $\bar{G_c}$ is the reduced mass flow rate and η_c is the isentropic efficiency. The subscripts d refers to the design values of the parameters.

$$\dot{G}_{\mathrm{c}} = \bar{G}_{\mathrm{c}}/\bar{G}_{\mathrm{c,d}}, \bar{G}_{\mathrm{c}} = \frac{\dot{m}_{\mathrm{c}}\sqrt{T_{\mathrm{c,in}}}}{P_{\mathrm{c,in}}} \tag{2.15}$$

$$\dot{n}_{\mathrm{c}} = \bar{n}_{\mathrm{c}}/\bar{n}_{\mathrm{c,d}}, \bar{n}_{\mathrm{c}} = \frac{n_{\mathrm{c}}}{\sqrt{T_{\mathrm{c,in}}}} \tag{2.16}$$

$$\beta_{\mathrm{c}} = \beta_{\mathrm{c,d}}\left(c_1\dot{n}_{\mathrm{c}}\dot{G}_{\mathrm{c}}^2 + c_2\dot{n}_{\mathrm{c}}\dot{G}_{\mathrm{c}} + c_3\dot{n}_{\mathrm{c}}\right) \tag{2.17}$$

$$\eta_{\mathrm{c}} = \eta_{\mathrm{c,d}}\left[1 - c_4\left(1-\dot{n}_{\mathrm{c}}\right)^2\right]\frac{\dot{n}_{\mathrm{c}}}{\dot{G}_{\mathrm{c}}}\left(2 - \frac{\dot{n}_{\mathrm{c}}}{\dot{G}_{\mathrm{c}}}\right) \tag{2.18}$$

$$\begin{cases} c_1 = \frac{\dot{n}_{\mathrm{c}}}{p\left(1-\frac{m}{\dot{n}_{\mathrm{c}}}\right)+\dot{n}_{\mathrm{c}}\left(\dot{n}_{\mathrm{c}}-m\right)^2} \\ c_2 = \frac{p-2m\dot{n}_{\mathrm{c}}^2}{p\left(1-\frac{m}{\dot{n}_{\mathrm{c}}}\right)+\dot{n}_{\mathrm{c}}\left(\dot{n}_{\mathrm{c}}-m\right)^2} \\ c_3 = \frac{-\left(pm\dot{n}_{\mathrm{c}}-m^2\dot{n}_{\mathrm{c}}^3\right)}{p\left(1-\frac{m}{\dot{n}_{\mathrm{c}}}\right)+\dot{n}_{\mathrm{c}}\left(\dot{n}_{\mathrm{c}}-m\right)^2} \\ c_4 = 0.3 \end{cases} \tag{2.19}$$

The values of m and p are set at $m = p = 1.8$. These values are chosen based on the results of Wang et al. [45] who found them especially to fit single-shaft radial compressor and radial micro turbine behavior and validated them with

experimental results.

Although there are limits for a real machine (chock and surge lines), these are not taken into account by the off-design model as it does not fit a specific machine. However, as explained in the subsequent chapters using this off-design model, the objective is to derive trends from the system when operating under non-nominal conditions rather than accurately modeling its precise limits.

Examples of the performance maps of the machines for one of the cases presented in chapter 5 are available in appendix A.

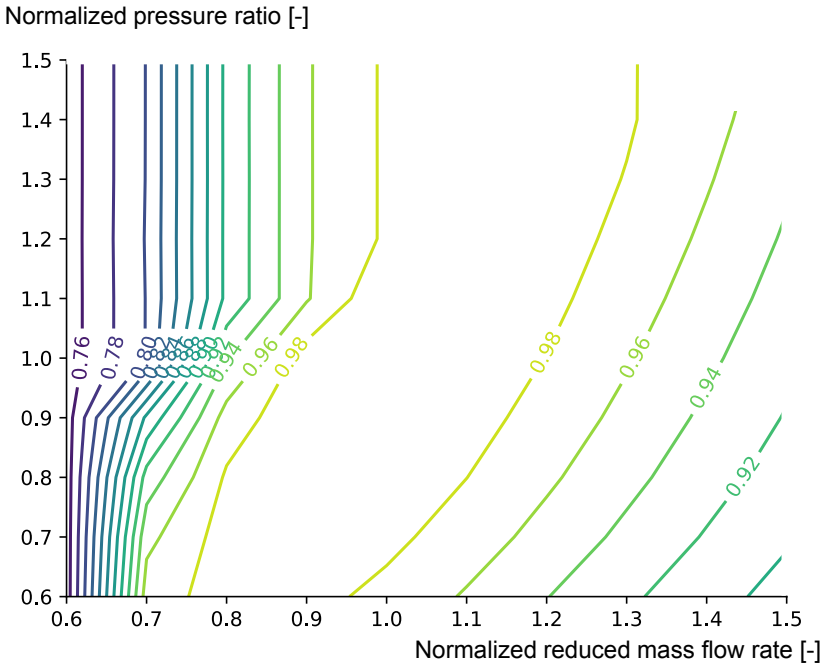

Figure 2.10: Normalized isentropic efficiency map at different normalized reduced mass flow rate and normalized pressure ratio.

2.2.5 Heat exchangers

The heat exchangers HPHX and LPHX play an important role in the cycle. They make it possible to control the temperatures at certain points of the cycle in order to ensure a good operation of the latter.
During the charging process, as the hot front progresses in the HR, the outlet temperature of the fluid T_3 will rise. The HPHX allows to evacuate the excess heat resulting from this increase and maintain a constant temperature at the inlet of

the turbine. This allows to operate it close to its nominal conditions and keep a low turbine exit temperature. As it is explained in section 4 about the impact of the cycle temperatures on the round trip efficiency, keeping a low turbine outlet temperature during charge is also beneficial for the round trip efficiency of the system as it avoids degrading the performances of the discharge cycle.

During the discharging process, the HPHX allows to evacuate the heat generated by the irreversibilities of the compression and therefore keeping the HR inlet temperature constant. The LPHX allows to evacuate the remaining heat of the working fluid at the outlet of the turbine to return to the initial state of the fluid and ensure a cyclic behavior.

In both the HPHX and LPHX, the heat transfer phenomenon is a rejection of heat from the working fluid to the ambient. Since the HEX inlet and outlet temperatures of the working fluid are known, and for the sake of simplicity, it is considered that the heat exchangers are sized to meet the rate of heat rejection of the working fluid but without doing the full sizing.

The heat exchangers are therefore only characterized by a relative pressure drop Δp undergone by the working fluid:

$$\Delta p = \frac{p_{in} - p_{out}}{p_{in}} \tag{2.20}$$

The values of Δp in the analyses of the following chapters are based on values taken from the literature as it is explained in the following chapter (section 3.2).

CHAPTER 3

CYCLIC BEHAVIOR ANALYSIS

Key results from this chapter

- At constant mass flow rate, the design case of 100 [kW]/6 [h] nominal discharge power and duration achieves a round trip efficiency $\eta_{rt} = 32.7[\%]$ and an energy density $\rho_E = 15.9[kWh_e/m^3]$.
- When operated at constant mass flow rate, due to temperature variations at the tanks outlets, power output/input experience important variations throughout the cycle and never reach nominal power during discharge.
- The average discharge and charge powers are respectively 80.7 [kW] and 247.2 [kW].

In this chapter, the performances of the Brayton-based packed bed PTES for a given set of design parameters are analyzed. The cyclic behavior, its characteristics and limitations are presented. Finally, an exergy analysis is carried out.

3.1 Performance metrics

In this section, some of the main performance metrics used in the upcoming analyses are defined.

The first performance metric of interest is the round trip efficiency. It is defined as the ratio between the total delivered energy during discharge E_{dis} and the total energy consumption during charge E_{ch} over a single charge-discharge cycle:

$$\eta_{RT} = \frac{E_{dis}}{E_{ch}} = \frac{\int_0^{t_{dis}} P_{e,dc}\, dt}{\int_0^{t_{ch}} P_{e,ch}\, dt} \tag{3.1}$$

The energy density is defined as the ratio of the energy delivered during discharge to the total packed bed reservoirs volume:

$$\rho_E = \frac{E_{dis}}{V_{HR} + V_{CR}} \tag{3.2}$$

The coefficient of performance of the heat pump or COP is defined as the ratio between the useful energy provided to the HR and the required energy. As it is explained later in this section, the variations of operating conditions during the cycle lead to variations of performances. Therefore, the COP is defined as the integral of the energy provided to the HR to required energy over the whole charging process:

$$COP = \frac{\int_0^{t_{ch}} \dot{Q}_{HR}\, dt}{\int_0^{t_{dc}} \dot{W}_{m,C} - \dot{W}_{m,T}\, dt} \tag{3.3}$$

The heat engine efficiency is defined as the ratio of useful work to energy provided from the HR. For the same reason as the COP, the useful work and energy provided are integrated over the whole discharging time:

$$\eta_{HE} = \frac{\int_0^{t_{dc}} \dot{W}_{m,T} - \dot{W}_{m,C}\, dt}{\int_0^{t_{dc}} \dot{Q}_{HR}\, dt} \tag{3.4}$$

The thermal energy density of a reservoir is defined as the ratio of its maximum energy capacity (based on given minimum and maximum temperature values) to its volume:

$$\rho_{E,th} = \frac{V \rho_s (1-\epsilon) \bar{c}_s (T_{max} - T_{min})}{V} = \rho_s (1-\epsilon) \bar{c}_s (T_{max} - T_{min}) \tag{3.5}$$

where $\bar{c}_s$ is the average specific heat capacity of the solid material over the $T_{min} - T_{max}$ interval. The other parameters are defined in section 2.2.1 about the modeling of the packed bed reservoirs.

The thermal energy density of the whole system is defined as the sum of the energy capacities of both reservoirs to the sum of their volumes.

3.2 Reference design

In order to keep consistency in our analyses and not confuse the reader, we have chosen a reference design on which all the analyses of the following sections are performed. Its main design parameters are shown in table 3.1.

Reference case	**Value**	**Unit**
Charge/discharge duration	6	hours
Rated discharge power	100	kW
Discharge compression ratio	6	-
Isentropic efficiency of compressors	80	%
Isentropic efficiency of expanders	85	%
Length-to-diameter ratio of HR and CR	1.5	-
Initial temperature of HR, $T_{\text{init,HR}}$	25	°C
Initial temperature of CR, $T_{\text{init,CR}}$	25	°C
Maximum temperature, $T_{\max}$	560	°C
Working fluid	Argon	-
Pressure loss of LPHX	5	%
Pressure loss of HPHX	5	%
Solid thermal energy storage material	Nonporous basalt	-
Density of solid material, ρ_{s}	3350	kg/m^3
Specific heat capacity, c_s	$2.01 \cdot T\,(°\text{C}) + 778.7$	$\text{J/Kg} \cdot \text{K}$
Average thermal conductivity, k_{s}	2.177	$\text{W/m} \cdot \text{K}$
Diameter of solid particles, d_p	30	mm

Table 3.1: Reference case design parameters.

Charging and discharging times have been set at 6 hours. Indeed, one of the potential applications of the battery is load shifting of renewable sources such as PV panels. Steinmann [18] and Tassenoy et al. [46] demonstrated that the optimal charge/discharge time for PV coupling typically falls within the range of 6 to 10 hours.

The nominal isentropic efficiencies of the compressors and expanders are based on the Turbec T100 properties from [47] that fit for this range of power, mass flow rate and compression/expansion ratios. The characteristics of the machines of the heat pump do not exactly correspond to those of the T100 (the temperature at the outlet of the heat pump compressor for example is higher than the Turbec T100 compressor). However, due to the lack of an existing machine specifically designed for this type of application, and under a conservative assumption, the isentropic efficiencies are assumed to be equal to those of the T100.

The maximum temperature (heat pump compressor outlet temperature) is set at 560 [°C]. This kind of temperature is relatively common in the literature [25, 38, 48]. Although this is too high for the compressor of the Turbec T100 and existing heat pumps, such temperatures can be achieved by modern aeroderivative

turbine compressors [48, 7]. It is therefore conceivable that in the near future this kind of temperature could be achieved in Brayton heat pump applications.

The pressure losses for the exchangers are based on the Turbec T100 recuperator from the results of Laterre [49]. Indeed, although their role is different from the latter, they are designed for the same range of mass flow rate and temperature differences as this recuperator.

Concerning the sizing of the reservoirs, the minimum size of a reservoir can be computed based on the input energy from the fluid during charging:

$$V_{min} = \frac{\dot{m}\bar{c}_{p,g}t_N}{\rho_s(1-\epsilon)\bar{c}_s} \tag{3.6}$$

where $\dot{m}$ is the mass flow rate of the working fluid; $\bar{c}_{p,g}$ is the fluid average constant pressure heat capacity over the temperature range considered in the reservoir; t_N is the nominal charging time; ρ_s the density of the storage material; ϵ is the packed-bed void fraction; $\bar{c}_s$ is the average specific heat capacity of the solid material.

As it is shown later in this chapter, oversizing the reservoirs allow to increase the efficiency of the system by improving their thermal efficiency. However, oversizing too much the reservoirs decreases the energy density and increases the capital cost of the system. The size of the reservoirs is therefore set to be two times the minimum size as done by Wang et al. [25].

Reference case	**Value**	**Unit**
Roundtrip efficiency, η_{rt}	32.7	%
Coefficient of performance, COP	1.28	-
HE effiency, η_{HE}	24.9	%
Mean charge power, $P_{e,ch}$	247.2	kW
Charge mass flow, $\dot{m}_{ch}$	1.25	kg/s
Mean discharge power, $P_{e,dc}$	80.7	kW
Discharge mass flow, $\dot{m}_{dc}$	1.26	kg/s
Charged energy	1492	kWh_e
Discharged energy	487	kWh_e
HR volume, V_{HR}	10.2	m^3
CR volume, V_{CR}	20.5	m^3
Energy density, ρ_E	15.9	kWh_e/m^3
Thermal energy density, $\rho_{E,th}$	179.8	kWh_{th}/m^3

Table 3.2: Reference case output parameters and performances.

Table 3.2 shows the performances of the reference case when operated over a complete charge-discharge cycle at a constant mass flow rate. The details of this analysis are presented in the next section. As it is explained, the power is not constant during the whole discharging process. This explains the fact that the average discharge power is lower than the nominal power. This also explains why the discharged energy is lower than the product of the nominal power and the discharge time.

During the charging process, the LPHX heat exchanger is not present, meaning that the pressure losses are lower than during discharge. Therefore, the required mass flow rate is slightly smaller during charge than discharge. It can also be observed that the mass flow rates, even though higher, are of similar magnitude as those of the Turbec T100 (0.75 [kg/s][47]). This observation confirms that the pressure losses in the HPHX and LPHX can be approximated to be similar to those of the recuperator in the Turbec T100.

3.3 Cyclic transient behavior

As explained earlier in section 2.1 about the modeling of a packed bed PTES system, due to the evolution of the temperatures in the packed bed reservoirs, the thermodynamic properties of the working fluid such as temperature and pressure vary over time. Therefore, the performances of the charging and discharging cycles do not remain constant over time. This section aims to describe this cyclic transient behavior for the reference design system over a whole 6h charging-6h discharging cycle. Since the thermal storage is the component with the biggest thermal inertia in the system, the thermodynamic cycle is considered in a quasi-steady state.

3.3.1 Thermal inertia behavior in the reservoirs

For a series of charging-discharging cycles, the temperature profiles in the packed bed reservoirs after charge and after discharge do not remain the same due to thermal inertia. The evolution of the temperature profiles in the HR for 10 cycles is shown in fig. 3.1. As it can be seen, the profiles after each cycle are not the same but tend to converge after several cycles. In order to analyze this convergence, we can compute the maximum temperature difference and the maximum difference in energy stored between a profile and the profile at the end of the previous cycle:

$$\Delta T_N = |T_N - T_{N-1}|_{max} \tag{3.7}$$

$$\Delta E_{stored,N} = \frac{|E_{stored,N} - E_{stored,N-1}|}{E_{stored,N}} \tag{3.8}$$

The stored thermal energy in the solid material for a given temperature profile is given by:

$$E_{stored} = A(1-\epsilon)\int_0^L \int_{T_{min}}^{T(x)} c_s(T)(T - T_{min})\, dT\, dx \tag{3.9}$$

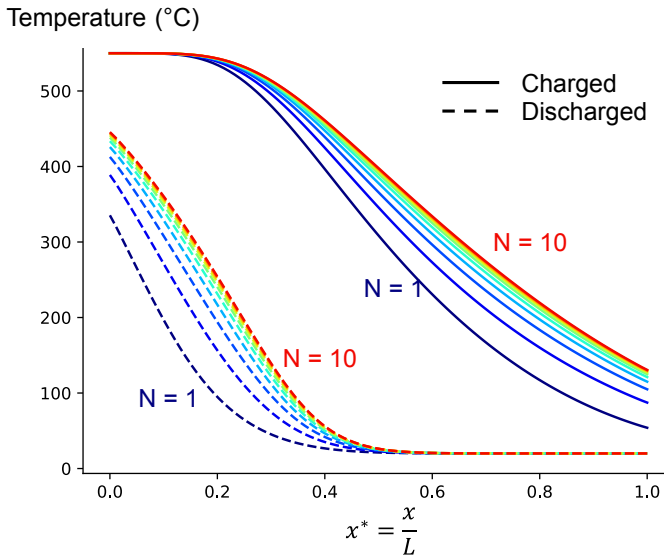

Figure 3.1: Evolution of the reference design HR charged and discharged temperature profiles from one to ten cycles.

Fig. 3.2a shows the decreases of ΔT_N and $\Delta E_{stored,N}$ with the number of cycles for the reservoirs of the reference design. For both reservoirs, the decrease of ΔT_N and $\Delta E_{stored,N}$ is exponential with the number of cycles. As it is explained later in this chapter, the state of charge of the battery is computed based on the thermal energy stored in the HR (eq. 3.10). It is therefore decided to consider the system cyclically stable when $\Delta E_{stored,N} \leq 0.1[\%]$ in the HR. In the reference design case, this is achieved after 17 cycles. It can also be observed that after 17 cycles, $\Delta E_{stored,N} < 0.1[\%]$ in the CR and $\Delta T_N < 0.1[°C]$ in both the HR and the CR. The cyclic analysis of the system over a full charging-discharging cycle therefore considers the discharged temperature profiles after the 17th cycle as the initial reservoirs temperature profiles. The oscillations observed for large numbers of cycles are most likely related to the tolerance limits of the numerical solver.

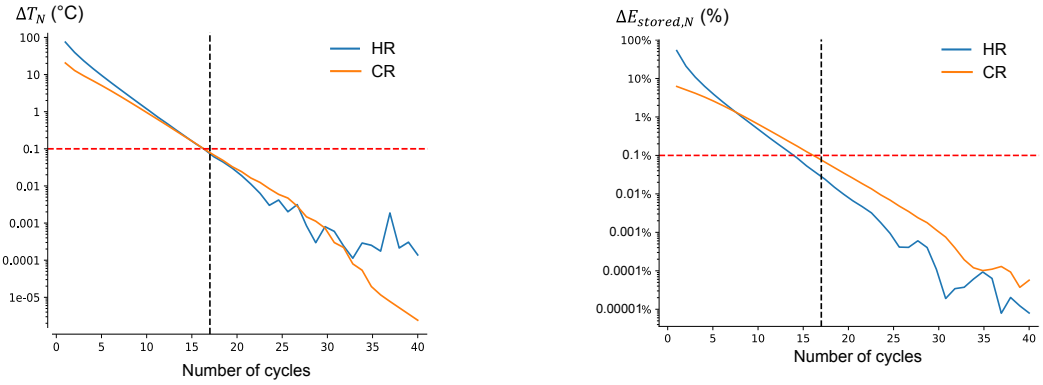

(a) (b)

Figure 3.2: Decrease of (a) $\Delta T_N = |T_N - T_{N-1}|_{max}$ (b) $\Delta E_{stored,N} = \frac{|E_{stored,N} - E_{stored,N-1}|}{E_{stored,N-1}}$ with the number of cycles for the HR and CR.

3.3.2 Cyclic behavior

The system is operating at constant nominal mass flow rate and compression ratio. This is done in order to keep the operating conditions of the compressors and expanders as close as possible to their nominal design conditions. This approach is widely used in the literature to analyze the cyclic transient behavior of packed bed PTES and their performance [36, 25, 14, 50] as it also simplifies the operational control strategy since operating at constant power instead of constant mass flow rate is not always possible, as it is explained in chapter 5 about operational considerations. However, with this kind of analysis, the powers and the total discharged energy are a result of the other parameters of the system and not an input variable.

The transient powers, pressure ratios and isentropic efficiencies of the machines as well as the pressures losses, inlet and outlet temperatures and temperature profiles of the packed bed reservoirs during the charge-discharge cycle are all shown on fig. 3.5. The initial and final temperature-entropy diagrams for both the charging and discharging processes are displayed on fig. 3.3. The evolution of the state of charge is shown on fig. 3.4. The SOC is defined such as to be 0% for an energy stored in the HR corresponding to the initial temperature profile in the reservoir (dashed red line in fig. 3.1). A SOC of 100% corresponds to an energy stored in the HR with the charged profile of fig. 3.1 (red solid line). The SOC at any moment t is computed based on the temperature profile in the HR:

$$SOC(t) = \frac{E_{stored,HR}(T_t) - E_{stored,HR}(T_{discharged})}{E_{stored,HR}(T_{charged}) - E_{stored,HR}(T_{discharged})}[\%] \tag{3.10}$$

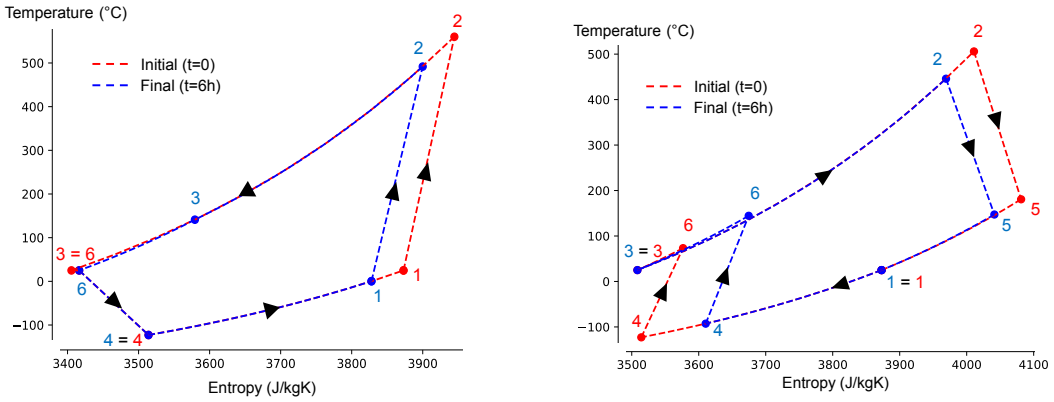

(a) (b)

Figure 3.3: Initial (t=0) and final (t=6h) T-s diagrams during (a) charge and (b) discharge.

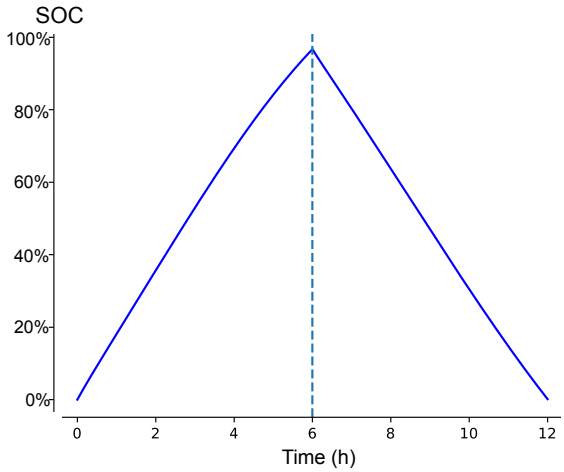

Figure 3.4: Evolution of the SOC during the charge-discharge cycle.

During the charging process, the shaft power (or net electrical power, displayed on fig. 3.5a in absolute value) remains stable for the first few hours of the charge, after what it gradually decreases. As the charge process proceeds, the cold front in the CR progresses towards the outlet of the reservoirs as it can be seen on fig. 3.5e. After approximately 2 hours, the temperature at the outlet of the CR starts to decrease, initially at a slow pace and subsequently accelerating (fig. 3.5d). Since the compressor is located directly after the CR in the charging process, the decrease in CR outlet temperature results in a decrease of the compressor inlet temperature. The compressor being set to operate at a constant pressure ratio, this results in a decrease of the compressor outlet temperature. The outlet temperature of the compressor also corresponds to the inlet temperature of the HR. This decrease can therefore be seen on fig. 3.5c. Since the system is set to operate at constant mass flow rate, this results in a decrease of the compressor power. The power at the turbine however remains constant, resulting in a decreasing net shaft power.

Another interesting consequence of the decrease of the compressor outlet temperature (HR inlet temperature) is the resulting temperature profile in the HR after charge. As it can be seen on fig. 3.5e, this results in a bell-shaped profile near the HR inlet.

The isentropic efficiency of the compressor also decreases due to the change in inlet temperature. However, as it can be seen on fig. 3.5f, the variation of isentropic efficiency is only in the order of a few tenth of percent and has therefore little influence on the system performance.

Due to the change in temperature in the HR and CR throughout the charging process, the properties of the fluid in the reservoirs also vary. Therefore, the pressure losses evolve throughout the charging process, as displayed in fig. 3.5b. In the HR for instance, as the hot front progresses, the average temperature in the tank increases. Therefore, the average density decreases and the pressure losses increase as predicted by eq. 2.12. The opposite phenomenon happens in the CR. It can also be observed that due to the relatively low mass flow rate, the pressure losses in the reservoirs are only in the order of a few dozens of Pa. Consequently, the pressure ratio in the expander remains relatively constant throughout the charging process even though the inlet and outlet pressures slightly vary.

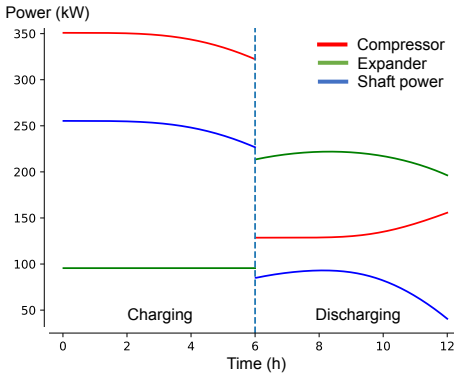

(a) Transient powers.

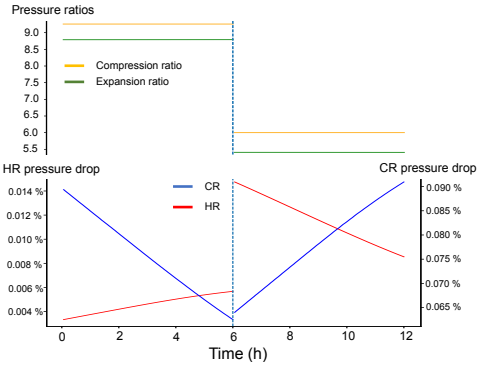

(b) Pressure ratios of the machines and pressure losses in the reservoirs.

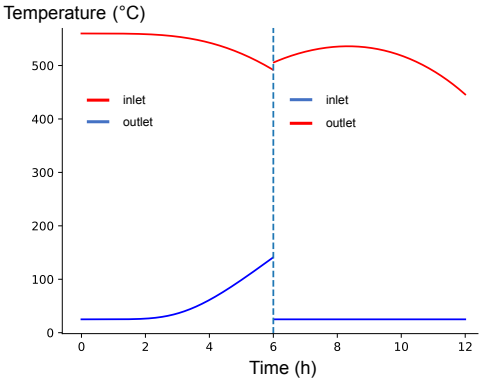

(c) Inlet and outlet temperatures of the HR.

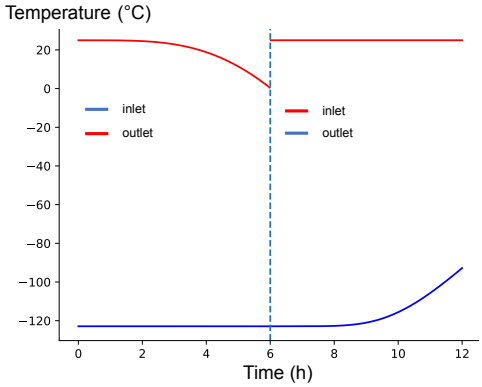

(d) Inlet and outlet temperatures of the CR.

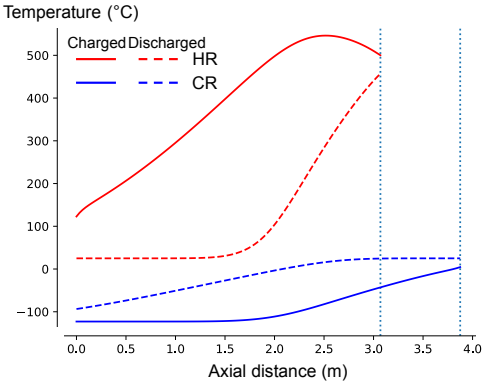

(e) Charged and discharged HR and CR temperature profiles.

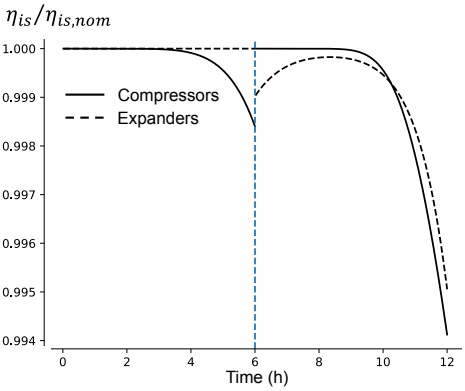

(f) Normalized isentropic efficiency of the compressors and expanders.

Figure 3.5: Transient behavior of the PTES system.

During the discharge phase, the inlet temperature of the turbine (HR outlet temperature) initially shows an upward trend, followed by a subsequent decline. This is a direct consequence of the temperature profile in the HR at the end of the charge phase. Again, due to the relatively small pressure losses in the reservoirs, the inlet pressure and pressure ratio of the turbine remains almost constant. As a consequence, and since the mass flow rate is also set to be constant, the isentropic efficiency and power of the turbine both follow the same trend as its inlet temperature. On the compressor side, the inlet temperature (CR outlet temperature) remains constant for the first half of the discharge. Subsequently, as the hot front progresses and reaches the outlet of the CR, this temperature shows an upward trend. Similarly to the turbine, since the inlet pressure, pressure ratio and mass flow rate of the compressor all remain constant, the compressor power follows the same trend as its inlet temperature. The isentropic efficiency of the compressor exhibits a comparable yet inverse pattern, declining as the inlet temperature rises. This is because an increase in the inlet temperature deviates the compressor from its nominal operating conditions. As a result of the transient powers of the compressor and turbine, the net shaft power first follows an upward trend, subsequently followed by a decline.

The pressure losses in the HR and CR follow a similar yet inverse trend as in the charging phase. As the cold front progresses in the HR, the average temperature decreases leading to a increase of the average density and therefore to a decline of the pressure losses. The opposite phenomenon happens in the CR.

3.4 Exergy analysis of the reference design

In this section, an exergy analysis of the reference system over a full cycle is presented, in order to identify where the exergy losses are located. To facilitate the analysis, the heat pump and heat engine cycles, as well as heat transfer within the packed bed, are studied as separate subsystems of the system. Since the cycle interacts with the ambient through the heat exchangers HPHX and LPHX, the reference state for exergy computations is established at the ambient temperature of 15 [°C] and atmospheric pressure.

Table 3.3 shows the exergy efficiencies of the various sub-systems. The exergy efficiency is defined as the fraction of useful exergy output over the fraction of exergy input of the sub-system. As it can be observed, the heat engine is the subsystem with the worst performance.

Since we are studying a Power to Power system, the exergy efficiency of the system is the same as the electrical efficiency. Indeed, the global exergy efficiency

of the system is defined as follows:

$$\eta_{ex,overall} = \eta_{ex,HP} * \eta_{ex,HT} * \eta_{ex,HE} = \frac{E_{dis}}{E_{ch}} \tag{3.11}$$

where $\eta_{ex,HP}$, $\eta_{ex,HP}$, $\eta_{ex,HP}$, E_{dis} and E_{ch} are respectively the exergy efficiencies of the heat pump, of the heat transfer in the packed bed reservoirs, of the heat engine and the discharged and charged energies over the full cycle.

All the numerical values shown on the Grassmann diagrams of the following figures are expressed as a percentage of the exergy supplied to the system, and therefore in this case of electrical energy, since exergy is equal to energy in the case of electricity. The numbering of the different states are shown on fig. 3.6.

Subsystem	Exergy efficiency [%]
Heat pump, $\eta_{ex,HP}$	72.7
Heat transfer through packed bed, $\eta_{ex,HT}$	92.3
Heat engine, $\eta_{ex,HE}$	48.6
Total, $\eta_{ex,overall}$	32.6

Table 3.3: Exergy efficiency of the different subsystems

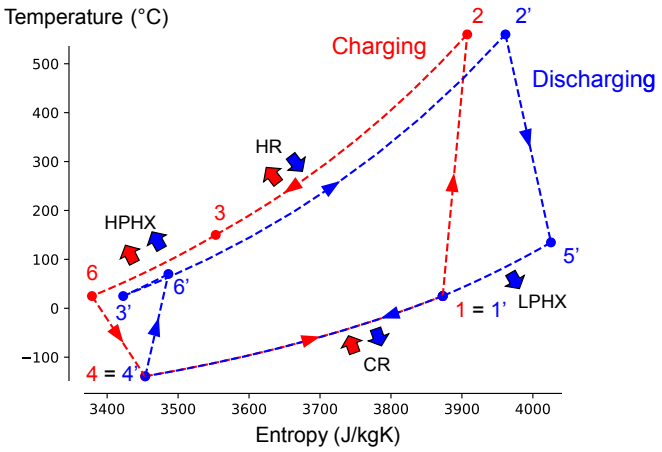

Figure 3.6: T-s diagram with the numbering of the different states.

3.4.1 Exergy analysis of the heat pump cycle

The various exergy losses of the heat pump cycle can be written as:

$$L_{HPHX} = \dot{m}_{ch}(e_{3,ch} - e_{6,ch}) \tag{3.12}$$

$$L_{Expander} = (e_{6,ch} - e_{4,ch}) - \dot{W}_{mT,ch} = \dot{m}_{ch}((e_{6,ch} - e_{4,ch}) - (h_{6,ch} - h_{4,ch})) \tag{3.13}$$

$$L_{Compressor} = \dot{W}_{mC,ch} - (e_{2,ch} - e_{1,ch}) = \dot{m}_{ch}((h_{2,ch} - h_{1,ch}) - (e_{2,ch} - e_{1,ch})) \tag{3.14}$$

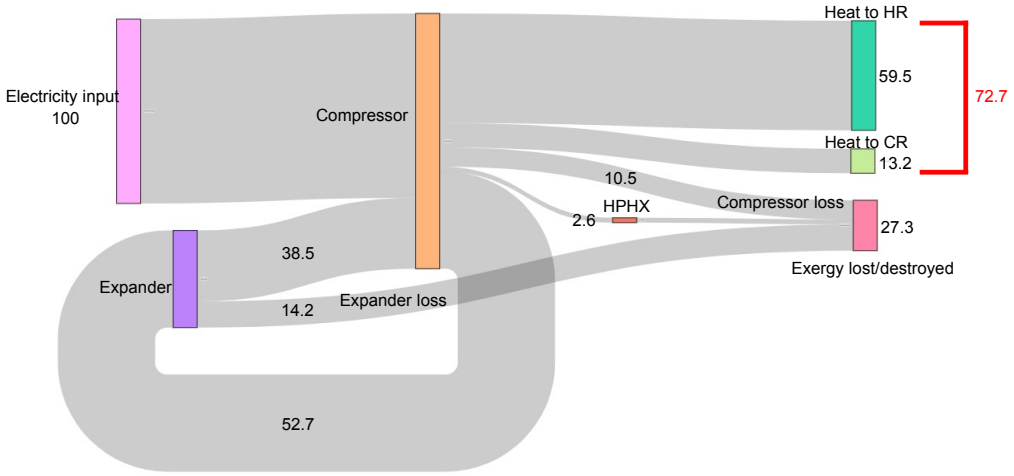

Figure 3.7: Grassmann diagram of the heat pump cycle (exergy is expressed as a percentage of the initial exergy).

3.4.2 Exergy analysis of the packed bed heat transfer

The heat transfer through packed beds leads to different types of exergy losses: pressure losses, conductive losses, convective losses and wall losses [36]. As explained in section 2.2.1, the walls of the reservoirs are considered perfectly insulated, therefore neglecting losses through them. In this study, the distinction between the various types of losses is not explicitly made, and they are collectively treated as a single overall loss for each tank. These losses are calculated using an exergy balance, as the difference between the output exergy of the fluid during discharge and the input exergy of the fluid during charge:

$$L_{HT,HR} = \dot{m}_{dc} * (e_{4,dc} - e_{1,dc}) - \dot{m}_{ch} * (e_{4,ch} - e_{1,ch}) \tag{3.15}$$

$$L_{HT,CR} = \dot{m}_{dc} * (e_{2,dc} - e_{3,dc}) - \dot{m}_{ch} * (e_{2,ch} - e_{3,ch}) \tag{3.16}$$

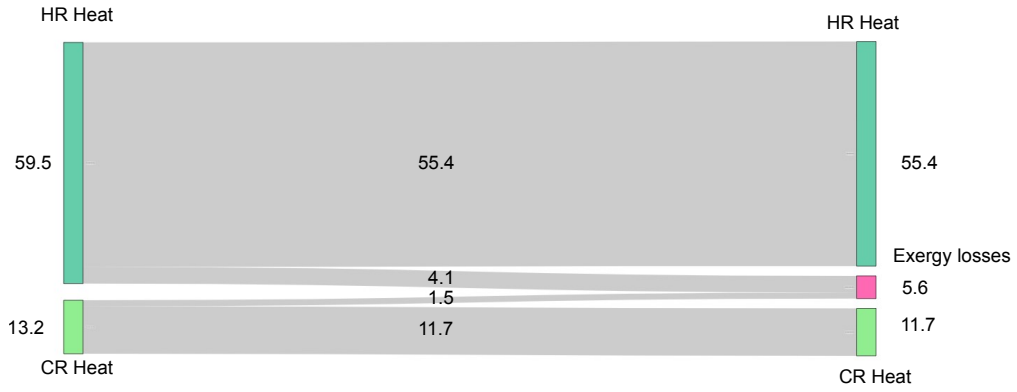

Figure 3.8: Grassmann diagram for the heat transfer inside the packed bed reservoirs (exergy is expressed as a percentage of the initial exergy).

3.4.3 Exergy analysis of the heat engine cycle

The various exergy losses of the heat engine cycle are shown below:

$$L_{HPHX} = \dot{m}_{dc}(e_{6,dc} - e_{3,dc}) \tag{3.17}$$

$$L_{LPHX} = \dot{m}_{dc}(e_{5,dc} - e_{1,dc}) \tag{3.18}$$

$$L_{Expander} = \dot{W}_{mT,dc} - (e_{2,dc} - e_{5,dc}) = \dot{m}_{dc}((h_{2,dc} - h_{5,dc}) - (e_{2,dc} - e_{5,dc})) \tag{3.19}$$

$$L_{Compressor} = \dot{W}_{mC,dc} - (e_{6,dc} - e_{4,dc}) = \dot{m}_{dc}((h_{6,dc} - h_{4,dc}) - (e_{6,dc} - e_{4,dc})) \tag{3.20}$$

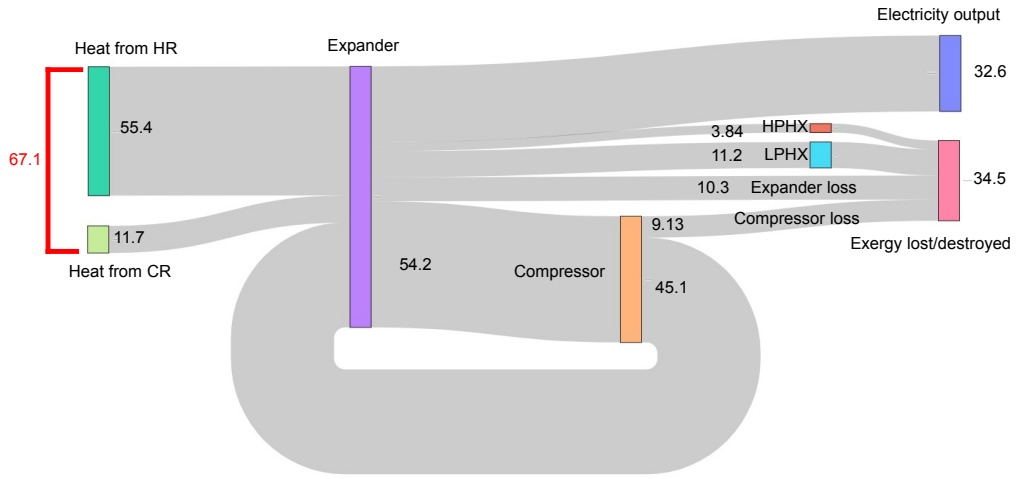

Figure 3.9: Grassmann diagram of the discharging cycle (exergy is expressed as a percentage of the initial exergy).

CHAPTER 4

PARAMETRIC ANALYSIS

Key results from this chapter

- The initial temperatures of the packed bed reservoirs (inlet temperatures of the heat pump machines) have a significant impact on the round trip efficiency and should both be set close to ambient temperature.
- For a 1 [%] drop of isentropic efficiency of expanders and compressors, the round trip efficiency is reduced by 2.64 [%].
- The length-to-diameter ratios and particle diameter d_p of the packed bed reservoirs have an important impact on the heat transfer efficiency and the pressures losses inside them.
- The impact of the L/D ratio on the round trip efficiency is not significant. An optimization of d_p can bring a slight gain.
- Air should be preferred as working fluid over argon, given its similar performances (η_{RT}=32.0[%] vs 32.7[%]), lower cost and easier operation. Helium should be avoided given its poor performances (η_{RT}=19.5 [%]).
- Uncertainties about bed properties do not play a significant role in the round trip efficiency uncertainty.

4.1 Temperatures

In this section the impact of the cycle temperatures on the performance of the PTES system is analyzed. It is first important to analyze which temperatures can be chosen as design variables and which ones are a result of the other variables. In order to get a better understanding of the following analysis, fig. 4.1 shows the temperature-entropy diagram of both the charging and discharging cycle . When looking at the charging cycle, three temperatures can be chosen as design variables: the temperature at the inlet of the compressor T_1 (corresponding to the initial temperature of the CR), the temperature at the outlet of the compressor T_2 (corresponding to the temperature at the inlet of the HR) and the temperature at the outlet of the HPHX T_6, corresponding to the initial temperature of the HR. The temperature T_3 at the outlet of the HR will varies throughout the operation of the system owing to the displacement of the thermocline inside the HR. The temperature T_4 at the outlet of the turbine is a result of the temperature T_6 and the turbine's pressure ratio (fixed by the compressor pressure ratio and the pressure losses in the system) and isentropic efficiency.

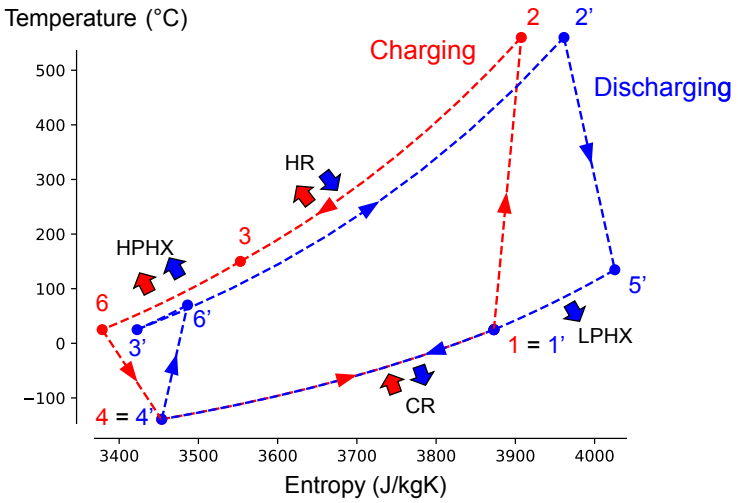

Figure 4.1: Temperature-entropy diagram during the charging and discharging processes. The red and blue arrows indicate a heat flux to/from a packed bed reservoir or the ambient in the case of the HPHX and LPHX during charge and discharge respectively.

During the discharging process, the temperatures T_4' and T_2' are decided by the outlet temperature of the CR and HR respectively. The outlet temperatures T_6' and T_5' of the compressor and the turbine are respectively a result of the

inlet temperatures T_4' and T_2', the pressure ratios and the isentropic efficiencies of the machines. The temperatures T_1' and T_3' are set to be equal to the charging temperatures T_1 and T_6 in order to ensure a cyclic operation of the system. Indeed, the discharge temperature T_1' corresponding to the inlet temperature of the CR sets the temperature of the CR at what will be the outlet of the CR during the following charging process, therefore deciding the temperature T_1 of the latter. Therefore, the temperatures of the discharging cycle are all resulting from other variables such as the charging cycle temperatures, the isentropic efficiencies of the machines, the compression ratio and the pressure drops in the packed bed reservoirs and the heat exchangers. The three design temperatures are therefore the inlet and outlet temperature of the compressor during charge T_1 and T_2 and the initial temperature of the HR T_6.

Fig. 4.2 shows the impact of the temperatures $T_1 = T_1'$ and $T_6 = T_3'$ on the round trip efficiency, COP of the HP, efficiency of the HE and temperature-entropy diagrams of both the HP and HE cycles. As a reminder, as explained in section 3.1 about the performance metrics, the COP/efficiency are the mean values integrated over the whole charge/discharge process. As it can be observed, increasing both T_1 and T_6 results in a decrease of the round trip efficiency. Since the round trip efficiency is directly proportional to the product of the COP of the HP cycle and the efficiency of the HE cycle, this trend can be explained by looking at the variation of the two latters with T_1 and T_6.

As it can be seen, increasing T_6 decreases the COP of the cycle. On the contrary, increasing T_1 results in an increase of the COP. The other important consequence of an augmentation of T_1 is the resulting augmentation of T_4 owing to the reduction of the compressor pressure ratio. Indeed, since T_2 is considered constant whatever T_1, increasing T_1 results in a decrease of the pressure ratio as it can be seen on fig. 4.2c.

Concerning the HE cycle, increasing $T_3' = T_6$ results in a decrease of the efficiency. Increasing the temperature T_1 also results in a decrease of the HE efficiency. However, this is not in direct consequence of the increase of T_1' in the HE cycle but results from the increase of T_4 in the HP cycle. As explained earlier, the temperature T_4' of the HE cycle is equal to the temperature T_4 of the HP cycle. Therefore, the increase of T_4 with T_1 in the HP cycle results in a similar increase of T_4' in the HE cycle, resulting in a decrease in efficiency of the latter.

It can therefore be concluded that minimizing both $T_1 = T_1'$ and $T_6 = T_3'$ is beneficial for the system round trip efficiency. However, in the HE cycle, these temperatures correspond to the outlet temperature of the LPHX and HPHX respectively. Since the exchangers operate with ambient air, these temperatures can not be realistically lowered below the ambient temperature.

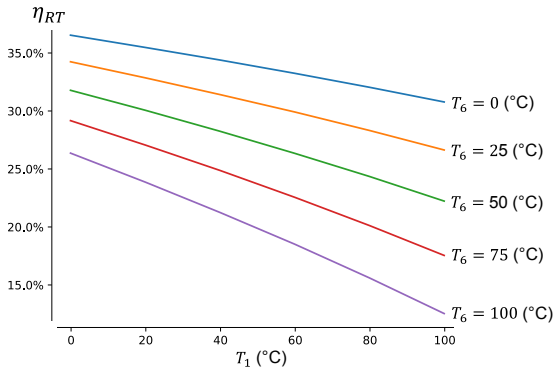

(a) Round trip efficiency.

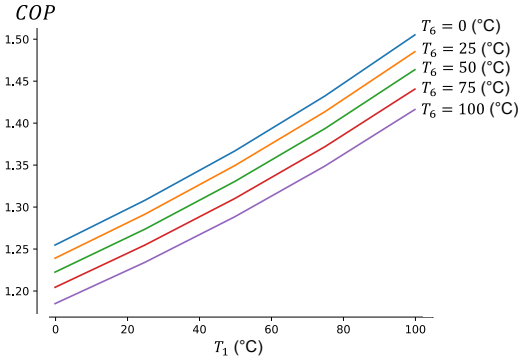

(b) COP of the HP cycle.

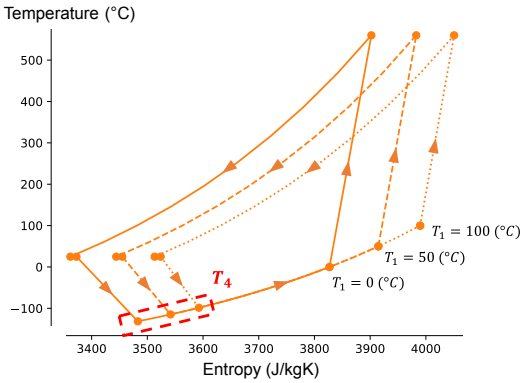

(c) T-s diagram of the HP cycle. The temperature T_6 and $T_3' = T_6$ are 25 [°C].

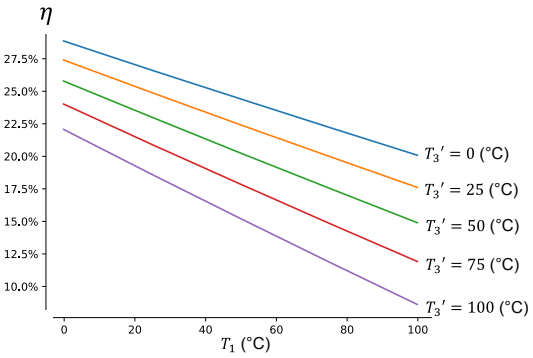

(d) Efficiency of the HE cycle.

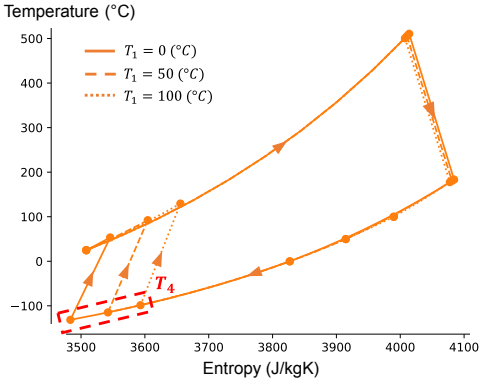

(e) T-s diagram of the HE cycle. The temperature T_6 and $T_3' = T_6$ are 25 [°C].

Figure 4.2: Impact of the temperatures T_1 and T_6 on the system performance.

Fig. 4.3 shows the impact of temperature $T_2 = T_2'$ on the round trip efficiency, COP of the HP, efficiency of the HE and temperature-entropy diagrams of both the HP and HE cycles. Again, since the COP of the HP and efficiency of the HE both vary throughout the charging and discharging processes, the displayed values are the average values over a whole charging/discharging cycle. As it can be observed, increasing T_2 is beneficial for the round trip efficiency. Again, this can be understood by looking at the impact of T_2 on the HP and HE performances.

In the case of the HP cycle, increasing T_2 results in a decrease of the COP. It can also be observed that increasing T_2 results in a decrease of T_4, unlike the case of the previous analysis on the impact of T_1.

On the contrary, the increase of T_2 shows to be very beneficial for the efficiency of the HE cycle, because of the increase of T_2' itself but also as a result of the decrease of T_4 owing to the increase of T_2 in the HP cycle.

It can therefore be concluded that increasing the temperature $T_2 = T_2'$ is beneficial for the round trip efficiency. However, this temperature corresponding to the outlet temperature of the compressor in the HP cycle, it is limited by the maximum outlet temperature of the machine.

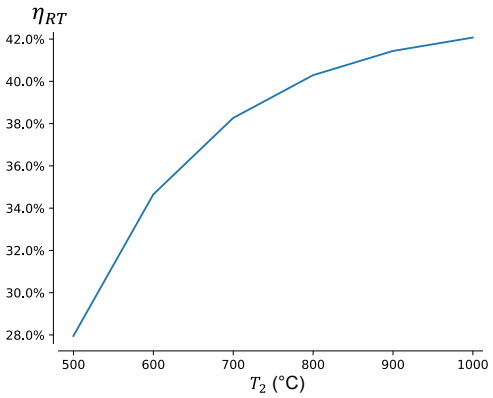

(a) Round trip efficiency

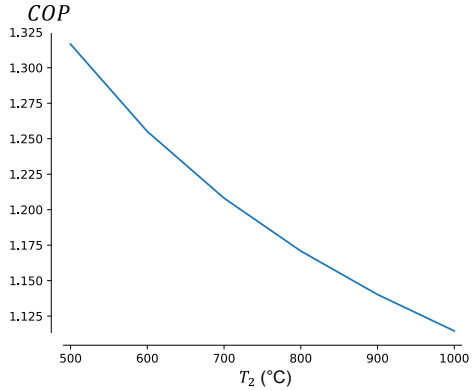

(b) COP of the HP cycle

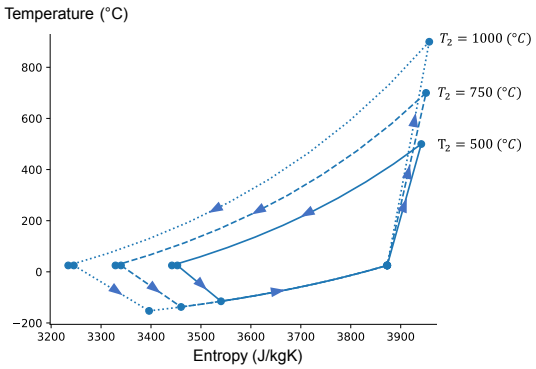

(c) T-s diagram of the HP cycle

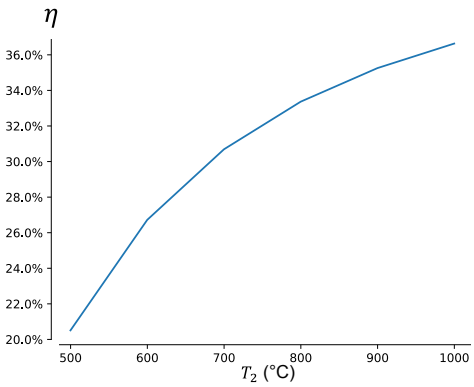

(d) Efficiency of the HE cycle

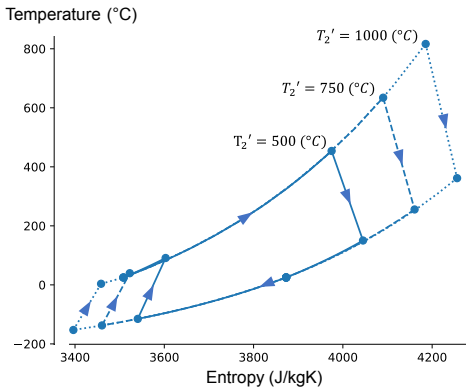

(e) T-s diagram of the HE cycle

Figure 4.3: Impact of the temperature T_2 on the system performance. The other temperatures are set is in the reference design.

4.2 Isentropic efficiency impact on the roundtrip efficiency

In an attempt to understand in more detail the impact of the machines' isentropic efficiency, the impact of the isentropic efficiency on the round trip efficiency in our reference design case is studied by setting the same isentropic efficiency for all the machines both at charge and at discharge.
The model (fig. 4.4) shows a strong linear dependence between the isentropic efficiency and the round trip efficiency. For a 1 [%] variation of isentropic efficiency, the round trip efficiency varies by 2.64 [%]. This analysis shows the critical importance of having compressors and expanders that have high isentropic efficiencies in a Brayton-based PTES system.

The round trip efficiency drops to 0 [%] for isentropic efficiencies below 70 [%]. We therefore confirm that only turbo-machines are suitable for our application.

On figs. 4.5a and 4.5b, the influence of the machines' isentropic efficiencies on the COP of the HP cycle and the efficiency of the HE cycle can be seen. The theoretical Carnot limits based on the cycle temperatures are located at 1.558 [-] for the COP and 64.17 [%] for the HE efficiency.

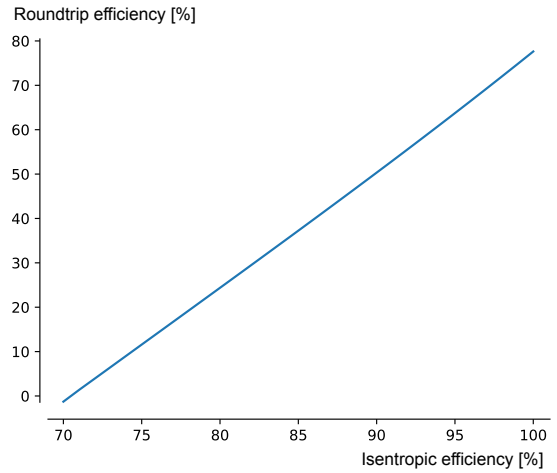

Figure 4.4: Effect of isentropic efficiency on the roundtrip efficiency

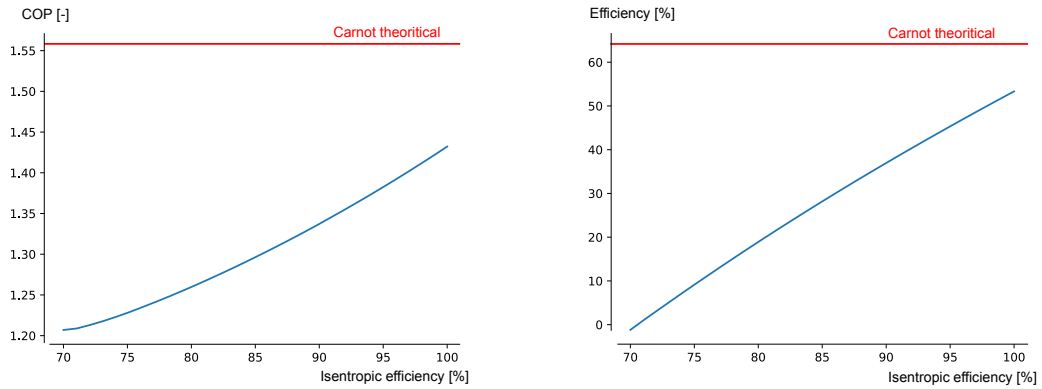

(a) (b)

Figure 4.5: Impact of the isentropic efficiency on (a) the HP COP (b) the HE efficiency.

4.3 Compression ratios

Fig. 4.6 shows the influence of the discharge compression ratio on the round trip efficiency for the reference design. Since the latter has no influence on the HP cycle, this trend actually reflects the impact of the compression ratio on the efficiency of the HE cycle. As expected for a Brayton cycle, the efficiency first rises as the compression ratio increases and reaches an optimum, subsequently decreasing for higher compression ratios. The optimum is found for a compression ratio $\beta = 4.8$ [-] with a round trip efficiency $\eta_{RT} = 33.15[\%]$.

As the charging compression ratio is not a design variable but a result of the compressor inlet and outlet temperatures and isentropic efficiency (the three latter being design variables), its influence on the system performances is not analyzed directly but can be deduced from the analysis on these temperatures.

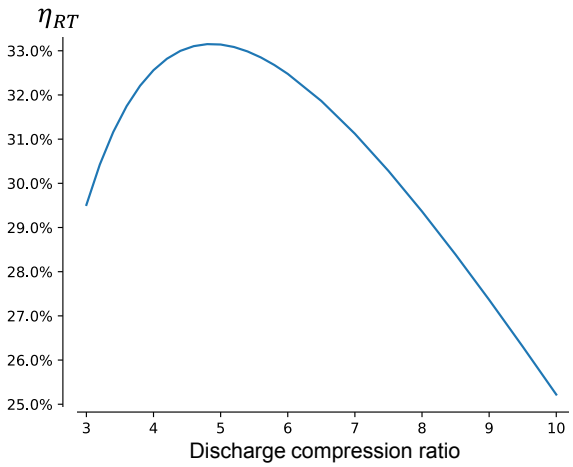

Figure 4.6: Influence of the discharge compression ratio on the round trip efficiency.

4.4 Parametric analysis on the reservoirs design parameters

The design parameters of the packed-bed reservoirs also influence the performance of the PTES system. In this section, the impact of these parameters is analyzed in order to determine which ones are important to optimize.
The system can be decomposed into two subsystems: the reservoirs which are modeled on the basis of the heat transfer and the rest of the cycle which considers the reservoirs as "black-boxes" with inlet and outlet temperatures and pressures.
We therefore first analyze the important parameters that have an impact on the heat transfer inside the packed-bed reservoirs. We then look at the overall system to analyze the impact of these parameters on the system's overall performances.
As the volume of the reservoirs are fixed and calculated according to the desired power and energy, their length and diameter can not be chosen independently. This L/D ratio can nevertheless be varied.
So for the reservoirs, two design parameters have to be studied, namely the choice of the length-to-diameter ratio L/D and the choice of the particle diameter d_p.

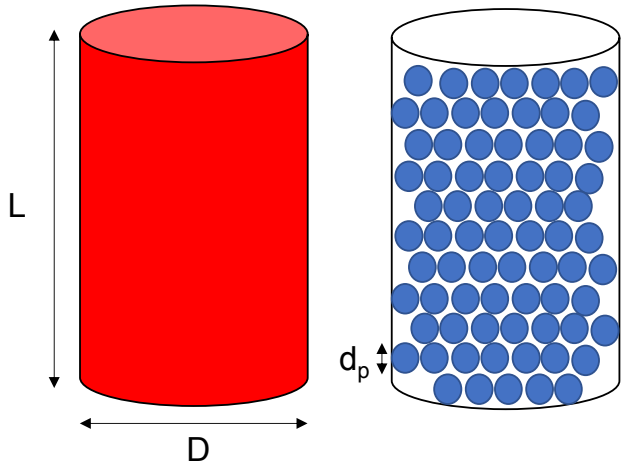

Figure 4.7: Design variables for reservoirs

When looking at the impact of these parameters on the heat transfer inside the reservoirs, the performance of the packed bed during charge and discharge can be expressed by the thermal efficiency. The overall energy balance in the control volume containing the reservoirs shown on fig. 4.8 between charge and discharge gives:

$$\begin{cases} E_{input,charge} = E_{stored} + E_{loss,exit,charge} + E_{loss,wall} \\ E_{stored} = E_{outflow,discharge} + E_{loss,wall} \end{cases} \tag{4.1}$$

As explained in chapter 2 about the modeling of the reservoirs, the walls are considered perfectly insulated and therefore $E_{loss,wall} = 0$.

The energy of the input and output flows is given by:

$$E_{input/output} = \dot{m}_f \int_0^{t_{charge/discharge}} \int_{T_{f,0}}^{T_{f,in/out}(t)} c_p(T)\, dT\, dt \tag{4.2}$$

The thermal efficiency is defined as the ratio between the energy extracted from the reservoir during discharge and the input energy of the fluid during charge:

$$\eta_{th} = \frac{E_{outflow}}{E_{input}} \tag{4.3}$$

A low value of η_{th} indicates an ineffective heat transfer or energy lost by hot fluid leaving the reservoir.

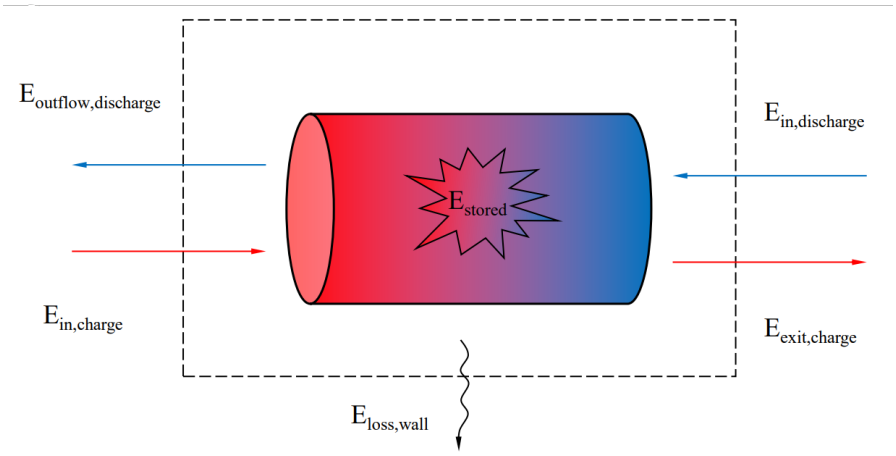

Figure 4.8: Energy balance inside a packed bed reservoir from S. Sava [14]

4.4.1 Length-to-diameter ratio impact on the heat transfer

The physical dimensions of the storage tanks are one of the design parameters that have an impact on the heat transfer inside them. By playing on the length-to-diameter ratio (L/D) of both reservoirs, the impact of the latter on the thermal efficiency and on the pressure losses can be analyzed. The results shown on the following figures are again for the reference design case.

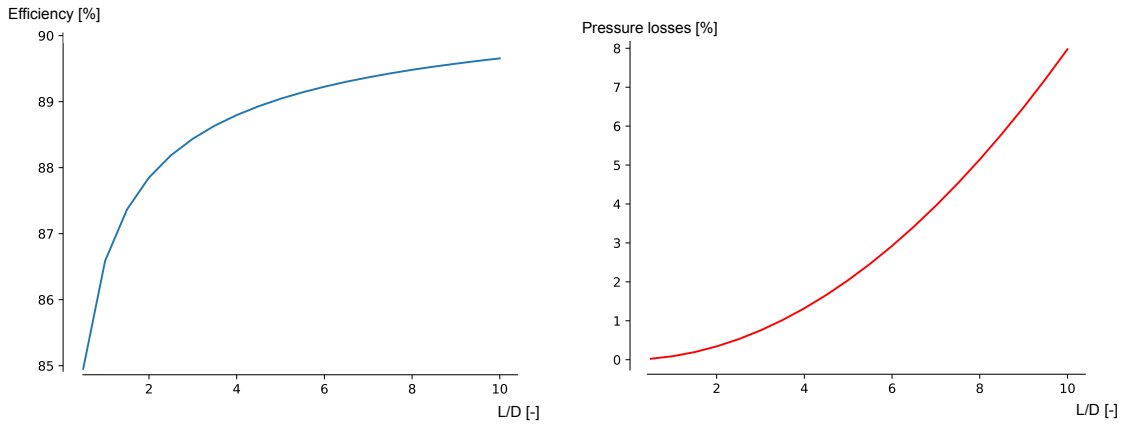

(a) (b)

Figure 4.9: (a) Impact of L/D ratio on the heat transfer efficiency (b) on the pressure losses (CR reservoir - end of discharge)

It can be observe on figs. 4.9a and 4.9b that the efficiency and the pressures

losses increase with the L/D ratio.

Indeed, increasing the L/D ratio while keeping the volume constant results in a decreasing cross-sectional area and therefore higher flow velocities and mass flow rate per unit area G. This results in a better heat transfer coefficient as predicted by eq. 2.3, resulting in a better heat transfer and a steeper thermocline inside the reservoirs, therefore decreasing the exit losses of eq. 4.1.

However, as increasing the L/D ratio increases both G and the length of the reservoir, this results in higher pressure losses as predicted by eq. 2.12.

Therefore a trade off will have to be found based on the round trip efficiency in order to limit the pressure losses while having a good thermal efficiency in the reservoirs.

4.4.2 Length-to-diameter ratio impact on the round trip efficiency

In order to optimize the L/D ratio to get the best round trip efficiency, we can try varying independently the L/D ratios of the two tanks and try to optimize them. This is done while keeping the volumes of the reservoirs constant at the values of the reference design, $V_{HR} = 10.21[m^3]$ and $V_{CR} = 20.49[m^3]$.

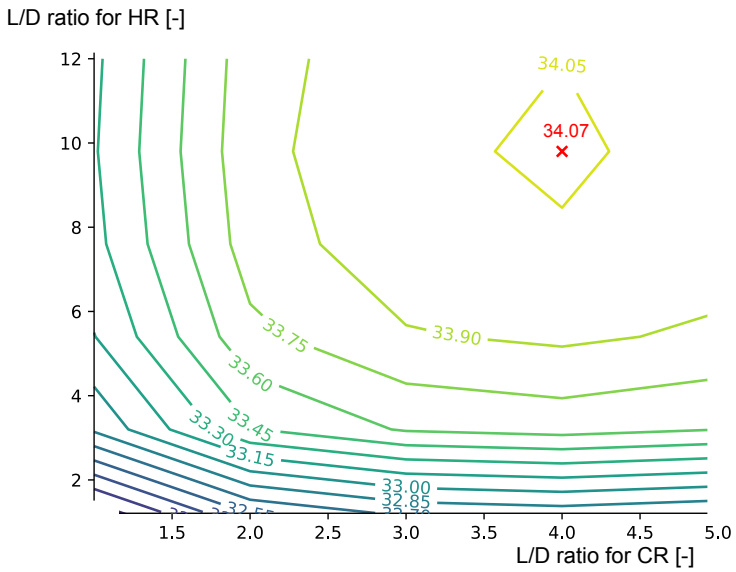

Figure 4.10: Round trip efficiency for different L/D ratios of the HR and CR. The red cross marks the optimum.

On fig. 4.10, it can be seen that there is an optimum at L/D HR= 9.8 [-] and L/D CR= 4 [-]. However, the optimum for the HR is probably overestimated.
Indeed, one of the main hypothesis of the Schumann equations is that the fluid flow is a 1D Newtonian plug flow, therefore allowing the neglect the wall effects in the equations. The condition for which this assumption remains valid is $\frac{D}{d_p} \geq 40$ [-] [40]. If we calculate the maximum L/D ratio for $d_p = 30$ [mm] we obtain:

$$\frac{D}{d_p} \geq 40 \rightarrow D \geq 1.2[m]$$

$$V_{HR} = 10.21[m^3] = \frac{L}{D}\frac{\pi D^3}{4}$$

$$(\frac{L}{D})_{max} = \frac{40.84}{\pi D^3} = 7.52[-]$$

The 1D Newtonian plug flow is therefore not valid for L/D HR = 9.8 [-] and the optimum value is probably lower, between 7.5 and 9.8.
Since the pressure drops in the HR are very small and given the findings of the subsection 4.4.1, it is not surprising to see that the L/D ratio for the HR is larger than for the CR. Indeed, the gain brought by the increase in length outweighs the losses due to pressure drops for L/D ratios below 10.
It should be noted that the maximum gain compared to the reference case 3.1 is only a little more than 1 [%] for reservoir choices that can be quite restrictive.

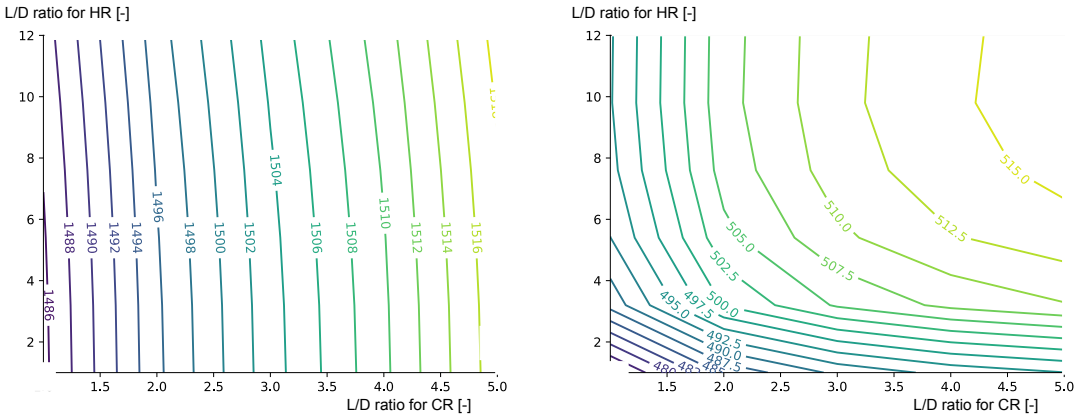

(a) (b)

Figure 4.11: (a) Energy input $[kWh_e]$ for different L/D ratios (b) Energy discharged $[kWh_e]$ for different L/D ratios

On figs. 4.11a and 4.11b, we can see respectively the energy input and the

energy output for each ratio. As it can be observed, the HR L/D ratio has almost no influence on the input energy. This phenomenon can be attributed to the fact that the input energy is affected by the power of the compressor during charge. The compressor power, in turn, is influenced by the variations in the outlet temperature of the CR and, consequently, its length-to-diameter (L/D) ratio. However, the outlet temperature of the HR has no impact on the charging power since the working fluid always releases excess heat from the outlet of the HR in the high-pressure heat exchanger (HPHX) to maintain a constant turbine inlet temperature.

Concerning the output energy, The HR and CR both have an impact on the output power profile as their respective outlet correspond to the inlet of the turbine and the compressor.

It is important to keep in mind that these analyses take into account perfect insulation of the reservoirs and therefore zero wall losses. Results may differ slightly in reality. Indeed, as the surface-to-volume ratio changes with the L/D ratio, parietal losses would also vary.

4.4.3 Impact of the particle diameter on the heat transfer

Fig. 4.12 shows the impact of the particle diameter d_p on the temperature profiles of the packed bed material during a charging process.
As it can be seen on figs. 4.12,4.13a,4.13b, d_p has a non-negligible impact on the behavior of the temperature profiles and on the behavior of the packed-bed.
In fig. 4.13a, we see that a smaller particle size will increase the thermal efficiency between the fluid and the packed bed (especially by increasing the volumetric heat transfer coefficient h_v in eq. 2.3), resulting in a steeper temperature profile as it can bee seen on fig. 4.12.
On the other hand, the pressure losses inside the CR increase rapidly as the particle diameter decreases. The displayed pressure losses of the CR are the pressure losses at the end of the discharge, because due to the higher fluid velocity owing to the lower pressure, they are bigger than in the HR and also reach their maximum at the end of the discharge. The impact of the particle diameter is therefore easier to visualize. We can see that they are quite small compared to those present in the HPHX and LPHX exchangers (below 2 [%] against 5 [%] for the heat exchangers). Thus a trade-off between a better efficiency and low pressure losses should be performed to optimize the system. To perform this trade-off, it is necessary to study the influence of the particle diameter on the round-trip efficiency, as done in the next subsection.

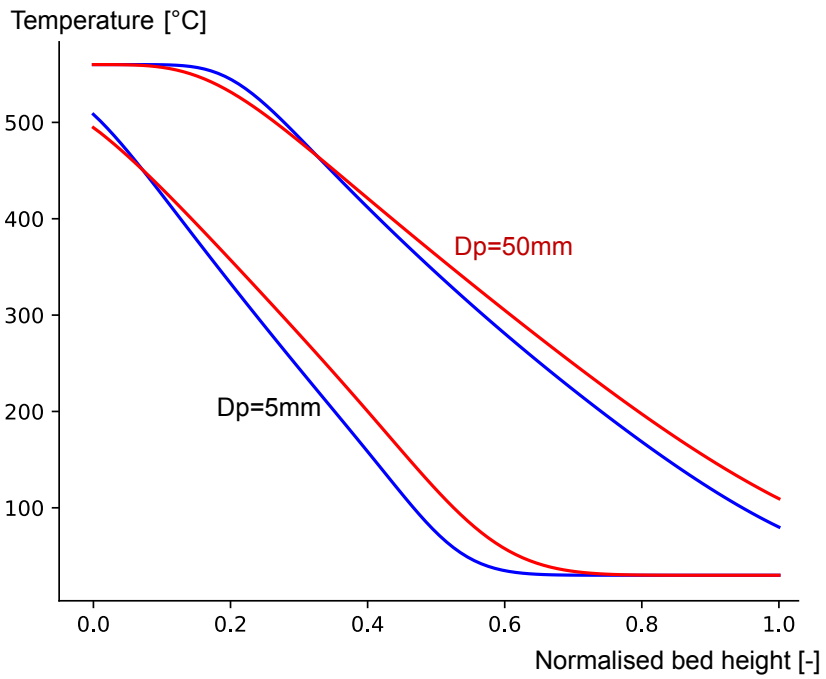

Figure 4.12: Charged and discharged temperature profiles of the solid material inside the HR for different particle diameters: $d_p = 5$ [mm] and $d_p = 50$ [mm].

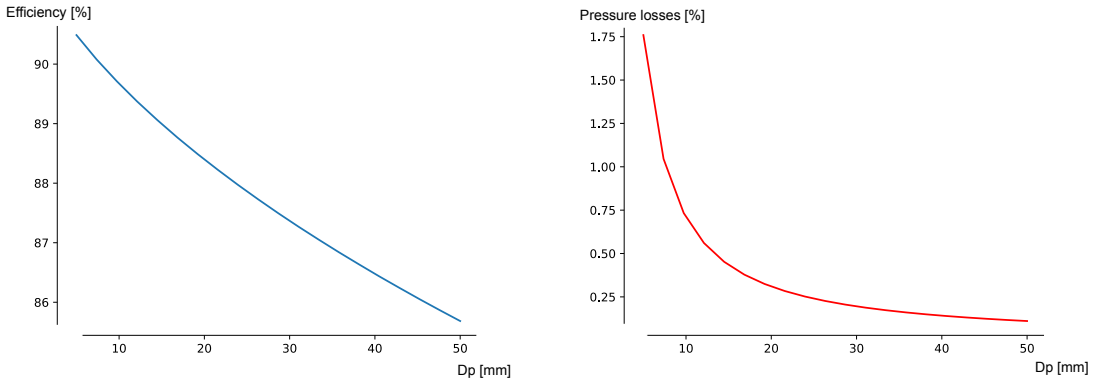

(a) (b)

Figure 4.13: Impact of the particle diameter on (a) the thermal efficiency (b) the pressure losses (CR reservoir - end of the discharge).

4.4.4 Impact of the particle diameter on the round trip efficiency

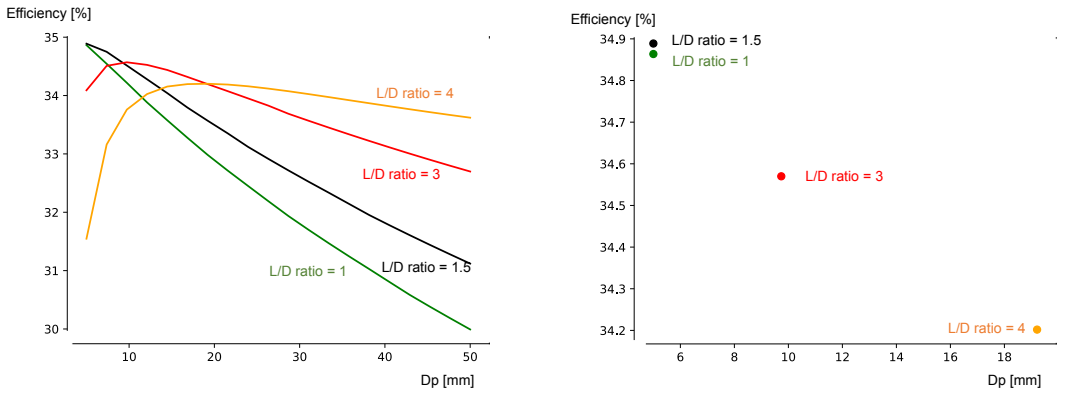

(a) (b)

Figure 4.14: (a) Impact of the particle diameter on the round trip efficiency (b) Optimum particle diameter for different L/D ratios.

If we look at the impact of the particle diameter on the round trip efficiency, we can see that for the design case (L/D ratio = 1.5) and for a small L/D ratio, there is an interest to work with small particle (under 5 [mm] in theory). As we work at low power (100 [kW]) we have relatively small mass flows rates (0.5-2 [kg/s]). The pressure drops in the tanks are therefore relatively small, allowing to work with small particles. If the L/D ratio are increased, the pressure losses increase as shown in the previous analysis. Due to this increase, the pressure losses for small particles become too high and the cycle efficiency deteriorates. The optimum for d_p increases with the increase of the L/D ratio, as shown on fig. 4.14b.

In view of the very small size of the particles (optimal d_p around 5mm for the reference case) we can ask ourselves if eq. 2.12 of the pressure losses inside the packed bed is still valid for this size of particles. According to the work of Li [51], it can be concluded that the pressure losses are underestimated when dealing with non-perfectly spherical particles within this size range, which is likely the case in reality. It is therefore necessary to calculate an equivalent diameter according to the shape of the particles so that eq. 2.12 correctly assess the pressure losses [51]. The optimum found is therefore probably overestimated and the real optimum will be for particles a little larger than those found by our optimization.
It should be noted that the variation in round trip efficiency is of the order of 3 [%] over the d_p ranges considered. The gain is therefore interesting in view of the ease of particle size selection.

All these conclusions about the L/D ratio and d_p analysis are in agreement with the work of Sava [14] and Zhang et al. [36].

4.5 Choice of working fluid

The choice of working fluid used also has an impact on the system performance. From the literature, mainly three different fluids have been studied and proposed: argon, helium and air. In this section, the impact of these three fluids is studied for the reference design case.

The fluid properties are evaluated with the CoolProp library [42]. The properties at 25 [°C] are shown in table 4.1, as well as the round trip efficiency obtained with each of the studied fluids. As it can be seen, argon and air yield similar round trip efficiencies while the use of helium results in a poor efficiency, lower than 20 [%].

As the heat capacity of helium is approximately 10 times higher than that of argon, the mass flow rates required in the cycles are about 10 times lower. This results in a very low heat transfer coefficient between the working fluid and the packed bed material as it can be seen in table 4.1. The volumetric heat transfer coefficient is defined in eq. 2.4 in chapter 2. As a result, the thermoclines inside the reservoirs have a very "flat" profile and the temperatures at the outlet of the reservoirs (inlet of the machines) experience big variations. Fig. 4.15 shows the CR/HR outlet temperatures during charge/discharge when using air, argon or helium.

As previously explained in this chapter, these variations of reservoirs outlet temperature lead to poor HP COP and HE efficiency, leading to a poor round trip efficiency. For the case of air, the mass flow rate and therefore the heat transfer coefficient is lower than with argon, but still remains high enough to avoid degrading too much the performances.

These findings contradict the trends observed in the literature concerning large-scale systems. Indeed, in most of the studies, helium was found to be the working fluid yielding the best efficiency. Wang et al. [25] found a round trip efficiency of 56.9 [%] with helium and 39.3 [%] with argon for a 10 [MW]/4 [h] system. Zhao et al. [52] arrived to similar conclusions for a 10 [MW]/6 [h] system. For these large-scale systems, the mass flow rates are way higher than for the small-scale design studied in this thesis. For his 10 [MW]/4 [h] design for example, Wang et al. considers a mass flow rate of 85.1 [kg/s] when working with argon and 8.6 [kg/s] when working with helium. With such mass flow rates, the problematically low heat transfer coefficient is avoided. Furthermore, since the pressure losses in the packed bed reservoirs become relatively important for mass flow rates of this

order, working with helium yields a better efficiency as it considerably reduces the pressure losses in the packed bed reservoirs compared with argon.

Another interesting observation is that the round trip efficiency with air is only a few tenths of percent lower than with argon. As it is cheaper, more available and gas leakages and infiltrations to/from the outside of the system would have practically no impact on the performances, air seems a more suitable fluid than argon. Frate et al. share the same conclusions [12].

Fluid	Heat capacity $c_{p,f}$ [J/KgK]	Density ρ $[kg/m^3]$	Mass flow rate [kg/s]	h_v in HR [W/m^3K]	Round trip efficiency η_{rt} [%]
Argon	521.55	1.63	1.26	4858	32.7
Helium	5193.20	0.163	0.13	850	19.5
Air	1006.31	1.18	0.64	2855	32.0

Table 4.1: Fluid properties, mass flow rate, heat transfer coefficient and round trip efficiency for Argon, Helium and Air.

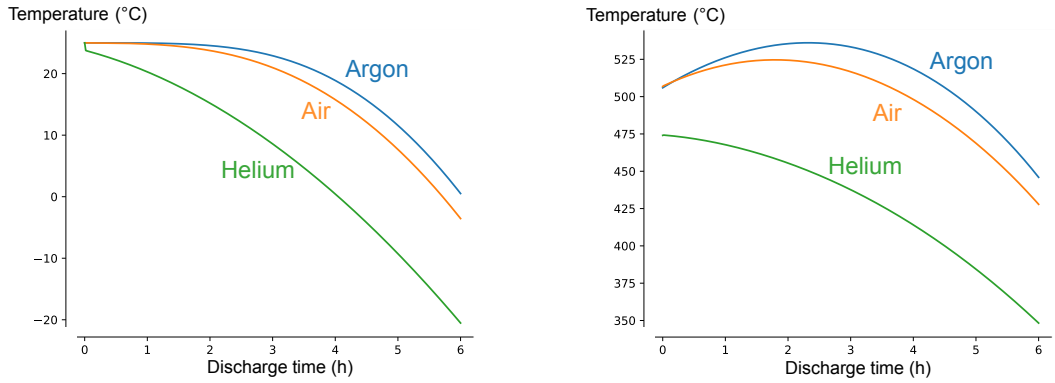

(a) CR outlet (compressor inlet) temperature during charge.

(b) HR outlet (turbine inlet) temperature during discharge.

Figure 4.15: CR/HR outlet temperatures during charge/discharge when using argon, air and helium.

4.6 Uncertainty Quantification

All systems are subject to uncertainties. In order to have a plausible estimate of the real performances of the system, it is essential to investigate the uncertainties associated with each design parameter and quantify their respective impacts.
In this section, we therefore study the uncertainties in the performance and pressure losses within the exchangers as well as the uncertainty in the cycle performance.

In the Schumann eqs. (2.1) and (2.2), several parameters can have uncertainties.

First, the fluid properties (ρ,c_p,k) are well known and evaluated with CoolProp [42] at each time and space step so the uncertainty of these parameters can be neglected. Solid properties on the other hand are subject to many uncertainties. Basalt is used for the nominal design packed bed material and the properties are taken from Zhang et al. [38]. The properties of basalt can vary in different ways. The source of the basalt has an influence on its properties: for example, basalt from Germany does not have the same properties as basalt from Austria [53]. Then, within a batch of basalt, the particles do not all have the same size [54]. The properties also undergo changes over time as the material goes through a certain amount of cycles during which it is alternatively heated and cooled over wide temperature ranges [53].

The void fraction ϵ and the volumetric heat transfer coefficient h_v both depend on other parameters such as the solid particle diameter d_p. It is therefore considered that any uncertainty on these parameters come from the other parameters and their uncertainty is not evaluated directly.

Finally, the pressure losses inside the HPHX and LPHX are also subject to uncertainties.

Table 4.2 shows the nominal values and related uncertainties of the parameters that are subjects to uncertainties.

Parameter	Nominal value	Absolute uncertainty	Source for value - uncertainty
Compressor isentropic efficiency	80 [%]	+/- 3 [%]	[47] - [55]
Expander isentropic efficiency	85 [%]	+/- 3 [%]	[47] - [55]
Particle diameter (d_p)	30 [mm]	+/- 2 [mm]	[38] - [56]
HX pressure losses	5 [%]	+/- 0.0025 [%]	[49] - [57]
Bed thermal conductivity (k)	2.177 [W/mK]	+/- 30 [%]	[38] - [53]
Bed specific heat capacity (c_p)	$2.01 * (T - 273.15) + 778.7$ [J/kgK]	+/- 30 [%]	[38] - [53]
Bed density (ρ)	3350 [kg/m^3]	+/- 30 [%]	[38] - [53]

Table 4.2: Nominal value and linked uncertainty of uncertain model parameters.

4.6.1 Uncertainty analysis on the packed bed heat transfer

The impact of the uncertainty of the packed bed parameters on the uncertainty of the thermal efficiency (eq. 4.3) as well as on the pressure drop are studied. Since some parameters such as the isentropic efficiency of the machines could significantly influence the inlet and outlet temperatures and pressures of the tanks, the uncertainties of the 4 physical parameters related to the bed (ρ_s, c_p, d_p and k_s) are the only ones considered.

The analysis is divided into 2 cases. Case 1 considers the same uncertainties as those listed in table 4.2.
In case 2, the uncertainty on the thermodynamic properties of the packed bed is reduced to +/- 10 [%]. According to the results of Knobloch et al. [53], this case corresponds to a stabilization of the thermodynamic properties of the packed bed after a certain amount of cycles.
The Sobol indices related to each parameter are shown in table 4.3. They indicate the effect of the uncertainty of each parameter on the uncertainty of the reservoir thermal efficiency. Since the analysis takes into account 4 parameters, the relevance threshold is set at $1/4 = 0.25$ and the uncertainty related to the parameters in red can be considered as negligible.

Parameter	Sobol index for case 1	Sobol index for case 2
Solid material density (ρ)	0.468675	0.304130
Solid material specific heat capacity (c_s)	0.468041	0.303335
Particle diameter (d_p)	0.067140	0.393260
Solid material thermal conductivity (k)	0.000024	0.000001

Table 4.3: Sobol indices of the parameters related to the thermal efficiency of the reservoirs.

It can be seen in table 4.3 that in case 1, the uncertainty on the density and on the heat capacity of the packed-bed explains almost all the uncertainty on the thermal efficiency.
In case 2, on the other hand, the uncertainty on the particle diameter plays a greater role, contributing more than the density or than the heat capacity for a fairly small variation (+/- 2 [mm]) in particle size. In both cases the uncertainty on the thermal conductivity does not influence the uncertainty on the heat transfer efficiency.

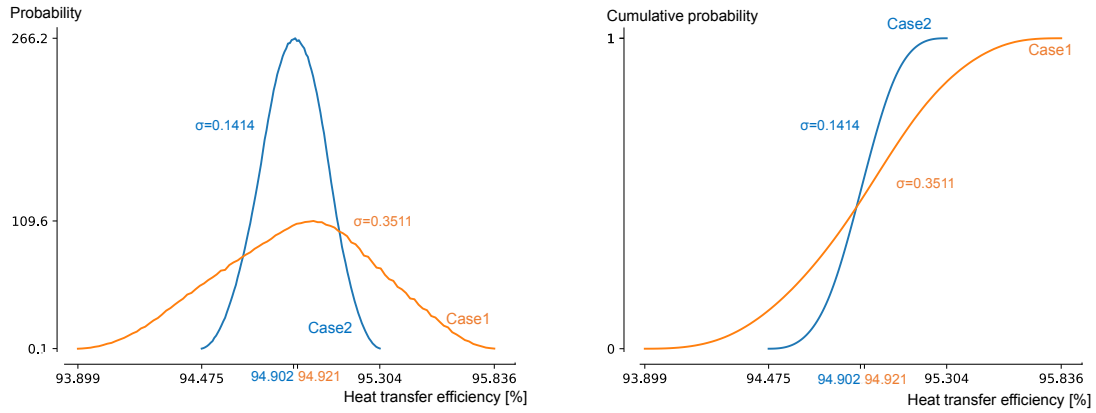

(a) (b)

Figure 4.16: (a) PDF for heat transfer efficiency (b) CDF for heat transfer efficiency

Figs. 4.16a and 4.16b respectively show the PDF and CDF of the thermal efficiency. As the uncertainties are reduced in case 2, the distribution is more spread out than in case 1.
The means and standard deviations for cases 1 and 2 are respectively equal to $\mu = 94.921[\%]$, $\sigma = 0.3511[\%]$ and $\mu = 94.902[\%]$, $\sigma = 0.1414[\%]$.

The second uncertainty study focuses on the pressure losses for which the Sobol indices are shown in table 4.4 and the PDF and CDF are shown on figs. 4.17a and 4.17b respectively.

Parameter	Sobol index for case 1	Sobol index for case 2
Bed density (ρ)	0.487484	0.364839
Bed specific heat capacity (c_p)	0.487155	0.364857
Particle diameter (d_p)	0.040064	0.272663
Bed thermal conductivity (k)	0.000007	0.000001

Table 4.4: Parameter' Sobol indices for pressures losses

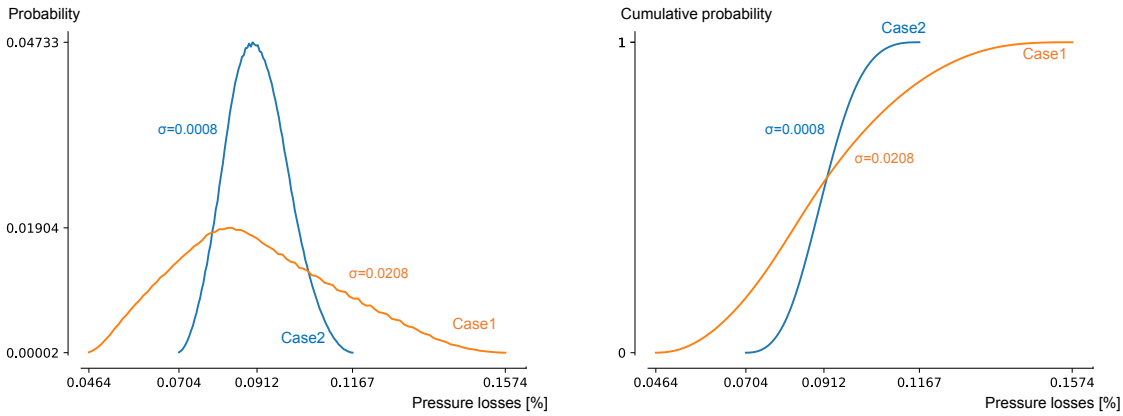

(a) (b)

Figure 4.17: (a) PDF for pressure losses (b) CDF for pressure losses

The pressure losses inside the CR are evaluated at the end of the discharge, when they are maximum. It can be seen that the pressure losses are very small, as it is already shown in section 3.3.2. The conclusions on the pressure losses are identical to those on the thermal efficiency except that the uncertainty on the particle diameter is not the one that has the greatest impact in case 2.
The means and standard deviations for cases 1 and 2 are respectively equal to $\mu = 0.0912[\%]$, $\sigma = 0.0228[\%]$ and $\mu = 0.0912[\%]$, $\sigma = 0.0008[\%]$.

4.6.2 Uncertainty analysis on the round trip efficiency

In this section, the impact of the parameters uncertainties on the uncertainty of the round trip efficiency is studied. The uncertainties considered for this analysis are summarized in table 4.2. Since the analysis takes into account 7 parameters, the relevance threshold is set at $1/7 = 0.14$. The parameters in the red part of the table are the one for which the Sobol indices are lower than this threshold. The uncertainty related to these parameters can be considered as negligible.

Parameter	Sobol index
Expander's isentropic efficiency	0.733511
Compressor's isentropic efficiency	0.154342
Bed density (ρ)	0.007828
Bed specific heat capacity (c_p)	0.007763
HX pressure losses	0.001552
Particle diameter (d_p)	0.000797
Bed thermal conductivity (k)	0

Table 4.5: Parameter' Sobol indices

It can be seen that only 2 parameters influence the uncertainty of the round trip efficiency in an important way, the isentropic efficiency of the expanders and the isentropic efficiency of the compressors. Reducing the uncertainty on these parameters would allow to consolidate the estimation of the round trip efficiency. The uncertainty on the isentropic efficiency of the expander is more significant than the uncertainty on the isentropic efficiency of the compressor. Fig. 4.18 shows that a variation of the isentropic efficiency of the expander has a stronger impact on the round trip efficiency than the efficiency of the compressor. Therefore, for the same uncertainty, the impact of the uncertainty of the expander isentropic efficiency on the uncertainty of the round trip efficiency will be greater. The isentropic efficiencies of the compressors and expanders are both set at 85 [%] on fig. 4.18 for a better visualization.

We can also see that the uncertainty on the thermodynamic properties of the cycle does not influence the uncertainty on the round trip efficiency. Only the uncertainty related to the machines have a significant influence. We can therefore conclude that no matter how uncertain the behavior of the packaged bed is, it will not influence the uncertainty on the round trip efficiency.

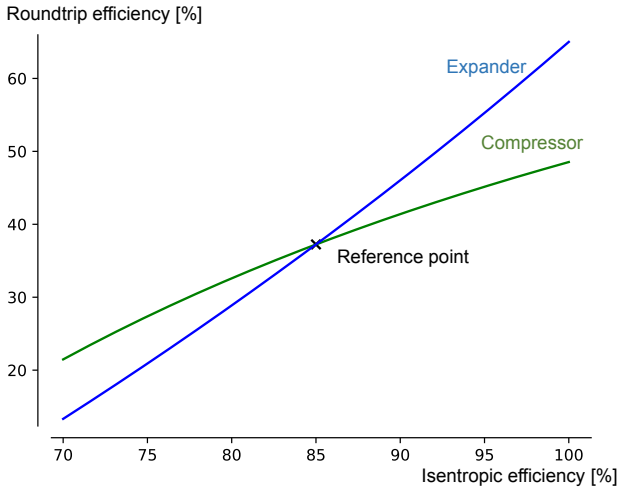

Figure 4.18: Effect of machine isentropic efficiency on round-trip efficiency when one is fixed at reference point and the other changes

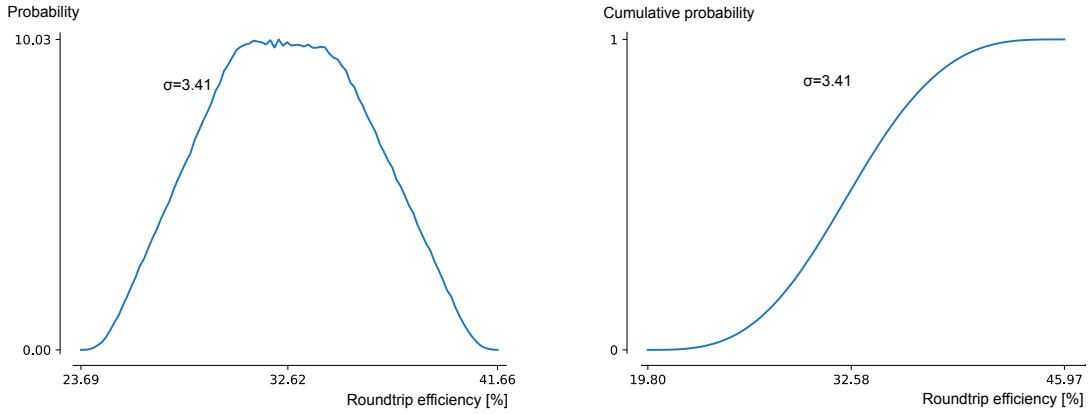

(a) (b)

Figure 4.19: (a) PDF for roundtrip efficiency (b) CDF for roundtrip efficiency

Figs. 4.19a and 4.19b show the PDF and CDF for the heat transfer efficiency. The means and standard deviations for the roundtrip efficiency are equal to : $\mu = 32.82[\%]$ and $\sigma = 3.41[\%]$.

CHAPTER 5

OPERATIONAL CONSIDERATIONS

Key results from this chapter

- In the reference design case, the part load capabilities of the system during charge are strongly limited by the off-design behavior of the machines.
- When trying to operate at constant nominal power during discharge, the system is only able to maintain the nominal power during 38.7 [%] of the time. This limitation arises from the decrease of the turbine inlet (HR outlet) temperature.
- Oversizing the reservoir or increasing their length-to-diameter ratio improves the discharge time operated at nominal power to respectively 62.9 [%] and 52.9 [%].
- Keeping the compressor outlet temperature constant during charge, by either varying the compression ratio or warming the fluid at the outlet of the CR, leads to improved discharge times operated at nominal power of 60.5 [%] and 56.5 [%] respectively.
- For incomplete charge cycles, the round trip efficiency is improved. The time operated at nominal power during discharge is improved for charge-discharge durations of 3h and longer.

In the previous chapter, the cyclic analysis of the PTES system is carried out with a constant mass flow rate. As explained, this approach is widely used in the literature. Some of the advantages are that it greatly simplifies the operational aspect and the machines operate close to their nominal design conditions. However, the resulting charge and discharge power profiles are dependent of this mass flow rate and the other system parameters and can not be chosen. Furthermore, due to the variations of cycle temperatures owing to the variations of temperatures at the inlet/outlet of the reservoirs, the powers are not constant. However, if the battery is to be used for load following or to accept surplus power from a constant production source, it must able to operate at a constant set power and vary this set power accordingly to the load.

The lack of research about the operational control strategy of the system was already highlighted in the literature, e.g. by Frate et al. (2021) [48] and most recently by Zhang et al. (may 2023) [58]. In this chapter, an analysis of the cyclic performance of the system with set power profiles and varying mass flow rate is carried out. The power limitations resulting from the operating conditions throughout the cycle are described. The resulting limitations on the system flexibility and performances are subsequently presented. An analysis of the parameters that can play a role in improving the output stability is then carried out. Finally, the incomplete charge/discharge capabilities and performances of the system are investigated.

5.1 Power limitations related to operating conditions

For a HP or HE cycle, the shaft power (in absolute value) is simply given by the product of the mechanical work and the mass flow rate:

$$P = \dot{m}|W_{m,C} - W_{m,E}| \tag{5.1}$$

where $W_{m,C}$ and $W_{m,E}$ are the mechanical work of the compressor and the expander respectively in $[\frac{J}{kg}]$. For an ideal HP or HE cycle in which the mechanical power is constant whatever the mass flow rate, the power varies linearly with the mass flow rate. This would be the case for a system in which the mass flow rate does not have an impact on the pressures and temperatures of the cycle. However, in a more realistic system as the one in this work, a variation of mass flow rate results in a variation of pressure losses in the components and isentropic efficiencies of the machines, as explained in section 2.2.4 about the off-design performances of the compressors and expanders. Therefore, the mechanical work of the cycle varies

with the mass flow rate and the variation of the shaft power with the latter is not linear. Fig. 5.1 shows the mass flow rate-power curves for the HP and HE of the reference design presented in the previous chapter (section 3.2). The curves for different compressor and turbine inlet temperatures are displayed as these also have an impact on the cycle mechanical work and off-design efficiency of the machines.

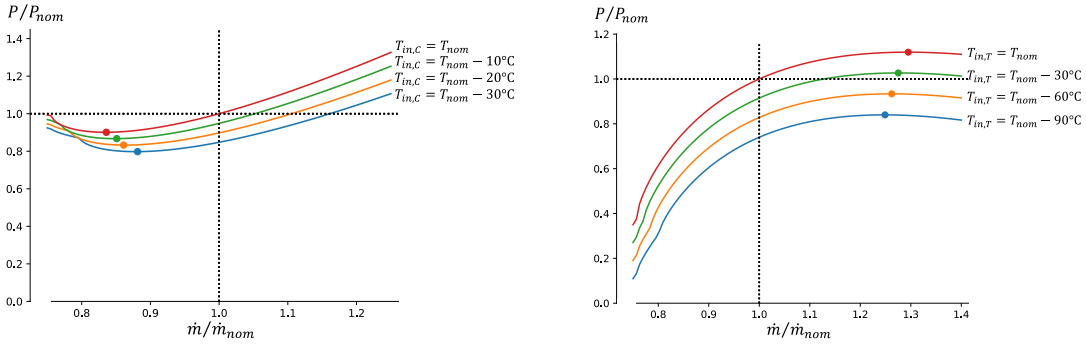

(a) (b)

Figure 5.1: Normalized shaft power as a function of the normalized mass flow rate for the (a) HP cycle for different compressor inlet temperatures (b) HE cycle for different turbine inlet temperatures. The minimum/maximum powers are indicated with a dot on each curve.

Concerning the HP, as can be observed, the power is limited by a minimum power, the value of the latter and the mass flow rate at which it is achieved depending on the operating conditions of the machines. As it can be seen on fig. 5.1a, for the reference design case operating at nominal temperatures, the power can not go below a fraction of about 0.9 [-] of the nominal power, limiting strongly the part load charging capabilities of the system. As it is shown in the previous chapter, the temperatures of the cycle evolve during the charging process. As it can be seen on the same figure, the decrease of compressor inlet temperature throughout the charging process would allow to decrease the minimum operating power of the HP.

Concerning the HE cycle, a similar yet opposite trend as the HP appears, as shown on fig. 5.1b. In this case, the power is not limited by a minimum power but a maximum power. Again, the value of the latter and the mass flow rate at which it is achieved depend on the operating conditions of the machines. As it can be seen, when the turbine inlet temperature gets too low compared to the nominal one, the maximum power is lower than the nominal power of the system. Since as shown in the previous chapter, the inlet temperature of the turbine decreases throughout

the discharging process due to the decrease of the HR outlet temperature, this strongly limits the capability of the system to operate at constant nominal power during the whole discharging process.

5.2 Constant power cyclic behavior

In the previous chapter, the performances and behavior of the reference design system were studied when operating at a constant mass flow rate. In this chapter, the performances and behavior of the system are studied when keeping the power constant and adapting the other parameters of the system in accordance with the power. As explained before, the charging power is only limited by a minimum power that decreases when the compressor inlet temperature decreases. Therefore, it is possible to operate the system at nominal power throughout the whole charging phase. During discharge, the system is set to operate at nominal power when the operating conditions allow it. When the maximum power is below the nominal power due to the operating conditions, the power is set to the max available power. If during the discharge, the maximum power falls below 0 [kW] or if the SOC gets to 0 [%] (meaning that the energy stored in the HR has returned to its initial state, see eq. 3.10), the discharge is stopped. For the rest of this chapter, the operating mode at constant power (or max power when the operating conditions do not allow it) is designated as CPWR and the operating mode at constant mass flow rate as in the previous chapter as CMFR.

The resulting performances at CPWR are displayed in table 5.1 and compared with the CMFR case. As it can be seen, the CPWR mode shows a round trip efficiency 2.4 [%] lower than the CMFR mode, owing to the lower HE mean efficiency over the discharging process. The COP are identical in both cases. Both the mean charge and discharge powers are higher in CPWR mode than in CMFR mode.

Performance metric	**CPWR**	**CMFR**	**Unit**
Roundtrip efficiency, η_{rt}	30.3	32.7	%
Mean HP coefficient of performance, COP	1.29	1.29	-
Mean HE efficiency, η_{HE}	23.2	24.9	%
Mean charge power, $P_{e,ch}$	255.3	247.2	kW
Mean discharge power, $P_{e,dc}$	88.4	80.8	kW
Energy input	1536	1491	kWh_e
Energy output	465	487	kWh_e
Energy density	15.2	15.9	kWh_e/m^3

Table 5.1: Reference design performances over a 6h charge-6h discharge cycle at nominal constant powers (CPWR) and constant mass flow rates (CMFR).

In order to better understand these differences, it is necessary to understand the behavior of the system in CPWR mode during charge and discharge. Fig. 5.2 shows the evolution of the powers, mass flow rates, inlet and outlet temperatures of the HR and CR, isentropic efficiencies of the machines and state of charge of the system throughout the whole 6h charge-6h discharge cycle.

Concerning the charging cycle (HP cycle), as expected, the power remains constant at nominal power during the whole process. In a similar way as the CMFR case of the previous chapter, the outlet temperature of the CR (compressor inlet) decreases in the second half of the charging process, owing to the progression of the thermocline inside it, resulting in a decrease of the mechanical work of the compressor since it is operating at constant compression ratio. In order to keep the shaft power constant, the mass flow rate progressively increases. This results in a decrease of the isentropic efficiencies of the machines due to the divergence of the operating conditions compared to the nominal ones. They however remain above 99 [%] of the nominal isentropic efficiencies.

During the discharging cycle (HE cycle), the behavior is not as straightforward. At the initial step of the process, as in the CMFR mode, the turbine inlet temperature (HR outlet temperature), is lower than the nominal one. The resulting max power of the cycle is lower than the nominal power of 100 [kW] as can be observed on fig. 5.2a. The turbine inlet temperature, following the same trend as in the CMFR case, subsequently increases, increasing the max power. After some time, the max power reaches the nominal power and the system starts operating at constant nominal power. As the turbine inlet temperature continues increasing, getting closer to the nominal one, the mass flow rate decreases to keep the power constant and the isentropic efficiencies of the machines both increase. Subsequently, the turbine inlet temperature starts decreasing and the opposite trend happens. After some time, the turbine inlet temperature reaches a point where the max power drops below the nominal power. The system therefore starts operating at the maximum power given by the operating conditions and the power starts declining. As it can be seen on fig. 5.1b, the lower the turbine inlet temperature, the lower the mass flow rate at which the max power is achieved. Therefore, as the turbine inlet temperature continues dropping, the mass flow rate starts decreasing towards the nominal one, increasing the isentropic efficiencies of the machines. After a bit more than 5h of discharge, the SOC reaches 0 [%], stopping the discharge.

Comparing the CPWR and CMFR mode during charge, the evolution of the temperatures and isentropic efficiencies of the machines are relatively similar, explaining the similar COP. However, in the CPWR mode, the power remains constant whereas in the CMFR mode, it declines at the end of the charge. This

explains the higher energy input in the CPWR mode as shown in table 5.1. During discharge, the isentropic efficiencies are lower in the CPWR case than in the CMFR case. In the latter, the minimum isentropic efficiency stays close to the nominal ones with as minimum $\frac{\eta_{is}}{\eta_{is,nom}} = 99.4[\%]$. The HE efficiency is therefore lower in the CPWR case than in the CMFR case, giving a lower energy output even with a higher energy input. As the round trip efficiency is defined as the ratio between energy output and energy input, this explains the lower round trip efficiency. The HR and CR volumes being identical in both cases, the energy density is logically lower in the CPWR case.

It can also be noted on fig. 5.2 that the evolution of the isentropic efficiencies, mass flow rate and compressor and expander powers is a oscillating in the second half of the discharge, when the max power is below the nominal power. This likely comes from the numerical resolution of the system of equations linking mass flow rate, isentropic efficiency, pressure losses in the reservoirs and powers. However, the curves remain stables and the trends remain clear. The curve of the shaft power also remains smooth throughout the whole discharging phase.

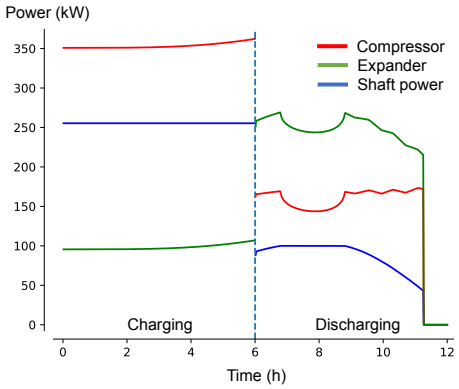

(a) Transient power.

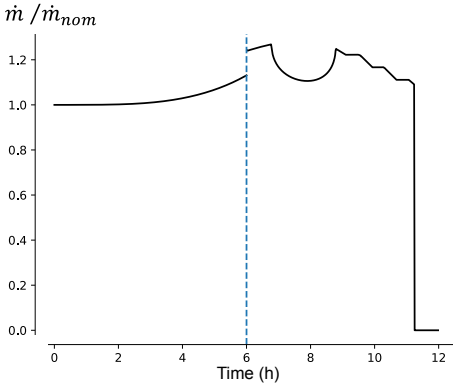

(b) Normalized mass flow rate $\frac{\dot{m}}{\dot{m}_{nom}}$.

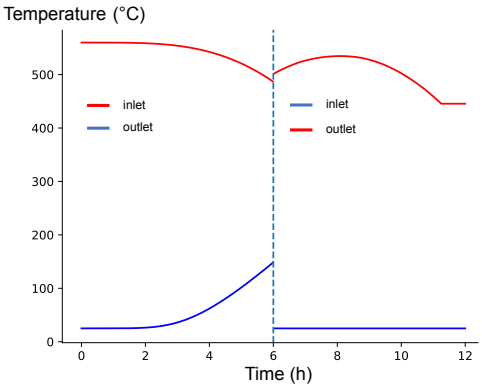

(c) Inlet and outlet temperatures of the HR.

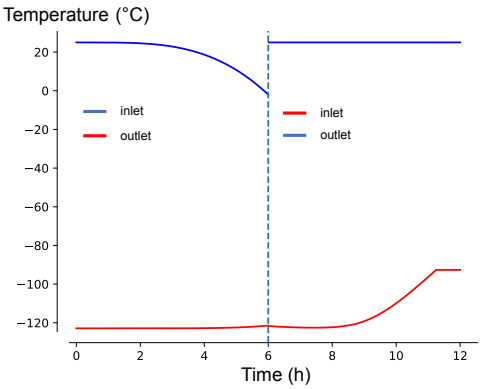

(d) Inlet and outlet temperature of the CR.

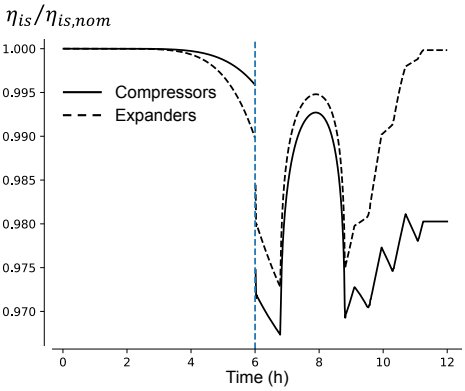

(e) Isentropic efficiencies of compressors and expanders.

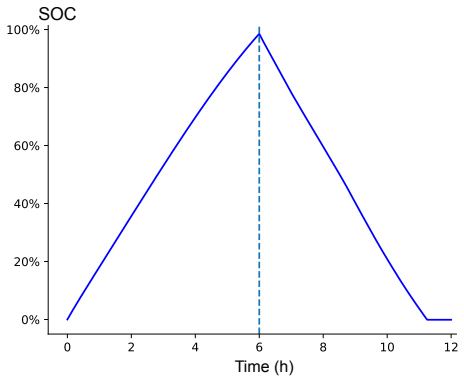

(f) State of charge.

Figure 5.2: Behavior of the PTES system over a full charging-discharging cycle with constant nominal power and varying mass flow rates (CPWR mode).

5.3 Design parameters to improve output stability

As seen in the previous section, the system can not operate at constant nominal power during discharge due to the power limitations owing to the variations of turbine inlet temperature. In this section, different possible solutions to increase the duration of operation at nominal power during discharge are presented. A new performance metric is introduced; the duration of discharge operated at nominal power over the total discharge duration, $\tau_{P_{nom}} = \frac{t_{dc,P_{nom}}}{t_{dc}}$ [%]. The impact on other performance indicators of the system is also analyzed.

5.3.1 Oversizing the reservoirs

As already explained in the previous chapter, oversizing the reservoirs results in more stable outlet temperatures and therefore a better thermal efficiency of the reservoirs and a better round trip efficiency. The oversize factor OVS is defined as the ratio between the reservoirs volume and their minimum volume defined in equation 3.6; $OVS = \frac{V_R}{V_{R,min}}$ [-].

Table 5.2 shows the performances of the PTES system for different OVS values. figs. 5.3a and 5.3b respectively show the shaft power and HR outlet temperature during discharge for these OVS values. Ref-CPWR refers to the case presented just before, with the reference design OVS=2 [-]. As expected, increasing the OVS increases $\tau_{P_{nom}}$ due to the higher and more stable HR outlet (turbine inlet) temperature allowing to operate the discharge at nominal power for longer durations. The mean discharge power logically also increases and as a result, so does the output energy E_{output}. The charge power remains practically constant, slightly decreasing because of the higher pressure losses in the reservoirs when their volume increases, resulting in a slight decrease of input energy E_{input}. All of this leads to a higher round trip efficiency for a higher OVS.

However, increasing the size of the reservoirs also has its downsides. The energy density drastically decreases when increasing the OVS. Larger reservoirs also mean higher costs. Increasing the volume of the reservoirs to such extends could therefore be complicated in reality.

Performance metric	Ref-CPWR	OVS=3	OVS=4	OVS=5	Unit
η_{rt}	30.3	32.9	33.8	34.3	%
$\tau_{P_{nom}}$	38.7	58.4	61.2	62.9	%
Mean COP	1.29	1.32	1.33	1.34	-
Mean η_{HE}	23.2	24.8	25.3	25.5	%
Mean $P_{e,ch}$	255.3	255.2	255.2	255.1	kW
Mean $P_{e,dc}$	88.4	93.3	95.0	95.9	kW
E_{input}	1536	1536	1535	1535	kWh_e
E_{output}	465	505	519	525	kWh_e
ρ_E	15.2	11.0	8.5	6.9	kWh_e/m^3

Table 5.2: Performances over a 6h charge-6h discharge cycle at nominal constant powers of the reference design case for which OVS=2 [-] (Ref-CPWR) and different oversizes of the HR and CR.

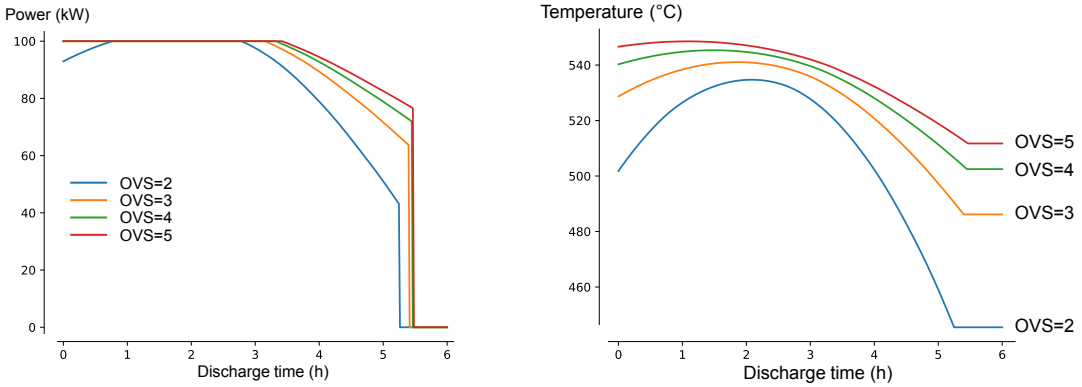

(a) (b)

Figure 5.3: (a) Shaft power and (b) HR outlet temperature (turbine inlet temperature) during discharge for OVS=2 [-] (Ref-CPWR), OVS=3 [-], OVS=4 [-], OVS=5 [-].

5.3.2 Length-to-diameter ratio of the reservoirs

Again, as explained in the previous chapter, increasing the length-to-diameter ratio of the reservoirs results in more stable outlet temperatures. The L/D ratios optimizing the round trip efficiency were found to be 9.8 [-] and 4 [-] for the HR and CR respectively, even though as explained, the optimum for the HR is probably overestimated due to the plug flow assumption of the Schumann model which stops being valid for L/D ratios above 7.5 [-].

Table 5.3 shows the performances of the PTES system for different L/D values, ranging from the reference design L/D = 1.5 [-] to L/D = 5 [-]. The L/D ratios of both reservoirs are set to the same value. As the HR outlet temperature during discharge remains higher and more constant when increasing L/D, as it can be seen on fig. 5.4b, $\tau_{P_{nom}}$ drastically increases when going from the reference design case with L/D=1.5 [-] to L/D=3 [-]. As already shown in the previous chapter, increasing the L/D ratio also gives rise to an increase of round trip efficiency. Further increasing L/D still increases $\tau_{P_{nom}}$ but in a lesser extent. As $\tau_{P_{nom}}$ increases, the mean discharge power $P_{e,dc}$ increases and as a result so does the output energy E_{output}. Therefore, increasing L/D might appear as a better solution than oversizing the reservoirs since the improvement of $\tau_{P_{nom}}$, even tough smaller, is still significant and increasing L/D does not decrease the energy density since the volume is kept constant.

Performance metric	**Ref-CPWR**	**L/D=3**	**L/D=4**	**L/D=5**	**Unit**
η_{rt}	30.3	31.7	32.0	32.1	%
$\tau_{P_{nom}}$	38.7	50.6	52.2	52.9	%
COP	1.29	1.30	1.31	1.31	-
η_{HE}	23.2	24.1	24.2	24.3	%
$P_{e,ch}$	255.3	256.1	256.8	257.8	kW
$P_{e,dc}$	88.4	91.1	91.7	92.0	kW
E_{input}	1536	1541	1545	1551	kWh_e
E_{output}	465	489	495	498	kWh_e
ρ_E	15.2	15.9	16.1	16.2	kWh_e/m^3

Table 5.3: Performances over a 6h charge-6h discharge cycle at nominal constant powers for the reference design case Ref-CPWR (L/D = 1.5 [-]) and various L/D ratio of the HR and CR.

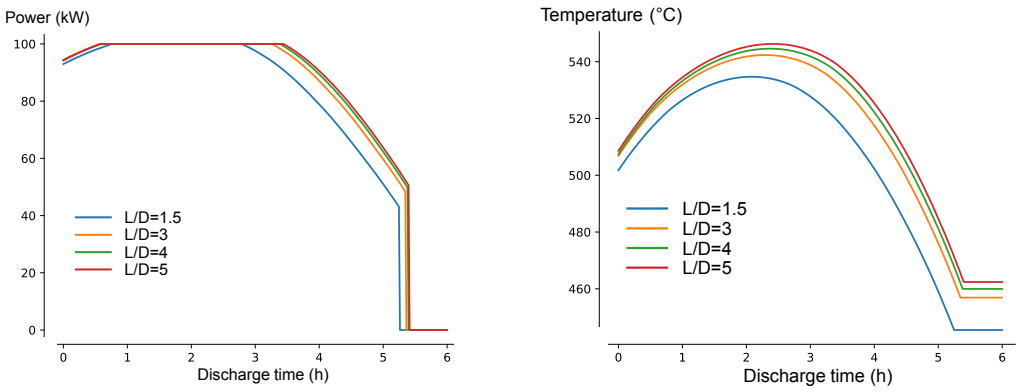

(a) (b)

Figure 5.4: (a) Shaft power and (b) HR outlet temperature (turbine inlet temperature) during discharge for L/D=1.5 [-] (Ref-CPWR), L/D=3 [-], L/D=4 [-], L/D=5 [-].

5.4 Constant compressor outlet temperature during charge

Another type of solution to improve the constant nominal power capabilities of the system during discharge would be to keep the compressor outlet (HR inlet) temperature constant during charge. In this section, two ways of achieving this are explored, namely varying the compression ratio and including the LPHX and an electrical resistance in the charging loop.

5.4.1 Varying the compression ratio

In all the previous analysis in this work, the charging process is carried out at constant compression ratio. However, another possible operating mode would be keeping the compressor outlet (HR inlet) temperature (T_2) constant during charge and varying the compression ratio and mass flow rate. This would result in a constant charging inlet temperature in the HR, therefore avoiding the lower turbine inlet temperature at the beginning of the discharge and improving the performance. However, varying the compression ratio and mass flow rate during charge would result in lower isentropic efficiencies of the machines, affecting negatively the system performances.

Fig. 5.6 shows the evolution of the powers, mass flow rates, inlet and outlet temperatures of the HR and CR, isentropic efficiencies of the machines and compression/expansion ratios of the system throughout the whole 6h charge-6h discharge

cycle. The compressors and expanders maps showing the variations of isentropic efficiency with the reduced mas flow rate and pressure ratio are shown in Appendix A. As it can be seen, when the inlet temperature of the compressor (outlet temperature of the CR) decreases at the end of the charging process, the compression ratio increases in order to keep the outlet temperature (inlet temperature of the HR) constant. Logically, the expansion ratio of the expander follows the same trend to keep the system in a cyclic behavior. As a result, the isentropic efficiencies of both machines decrease. The mass flow rate slightly decreases to keep the shaft power constant. As a result of the constant compressor outlet (HR inlet) temperature during charging, the turbine inlet (HR outlet) temperature remains stable at the nominal temperature for a relatively long time during discharging, resulting in stables isentropic efficiencies and a stable nominal output power. As always, the temperature eventually starts decreasing, until a point when the nominal power can not be achieved anymore, therefore continuously decreasing the output power until the end of the discharge.

As it can be seen in table 5.4, the increase in τ_{Pnom} when operating at constant compressor outlet (HR inlet) temperature is significant. Concerning the round trip efficiency, the positive effect of the higher turbine inlet (HR outlet) temperature during the discharge outweighs the negative effect of the lower isentropic efficiency during charge. The round trip efficiency shows an increase of a bit less than 2 [%]. The energy density ρ_E is also subject to a slight increase.

Performance metric	**Ref-CPWR**	**CST-T2-β**	**Unit**
η_{rt}	30.3	32.05	%
$\tau_{P_{nom}}$	38.7	60.5	%
COP	1.29	1.28	-
η_{HE}	23.2	24.5	%
$P_{e,ch}$	255.3	255.3	kW
$P_{e,dc}$	88.4	89.8	kW
E_{input}	1536	1536	kWh_e
E_{output}	465	492	kWh_e
ρ_E	15.2	16.0	kWh_e/m^3

Table 5.4: Performances over a 6h charge-6h discharge cycle at nominal constant powers of the reference design case at constant charging compression ratio (Ref-CPWR) and constant compressor outlet temperature with varying compression ratio (CST-T2-β).

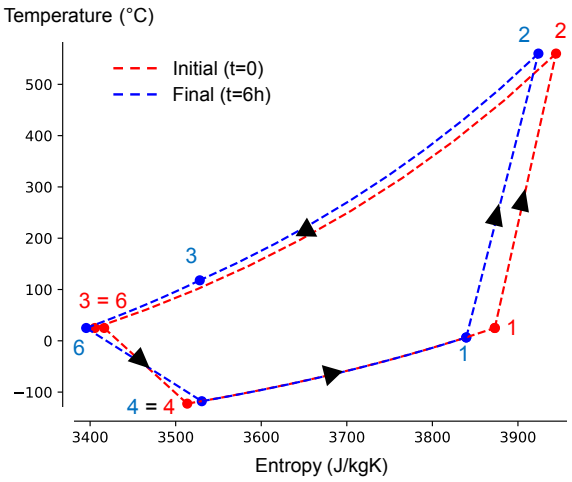

Figure 5.5: Initial and final charging T-s diagrams for the system operated at constant T_2 and varying compression ratio (CST-T2-β).

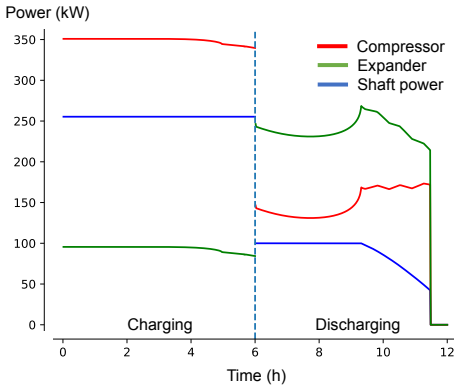

(a) Transient power.

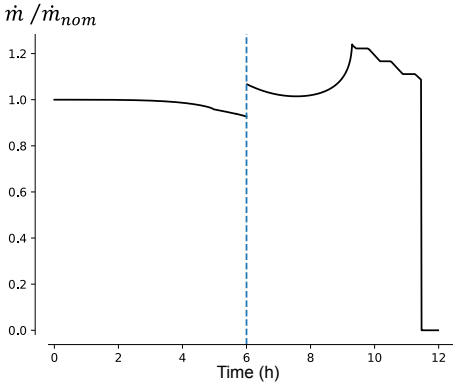

(b) Normalized mass flow rate $\frac{\dot{m}}{\dot{m}_{nom}}$.

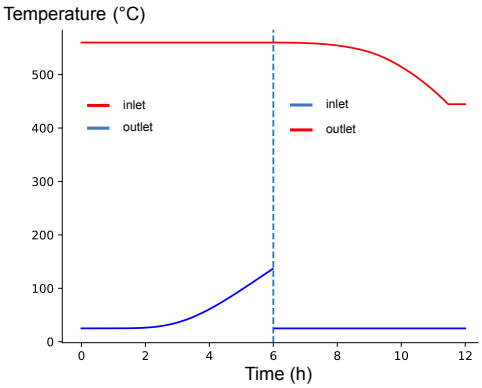

(c) Inlet and outlet temperatures of the HR.

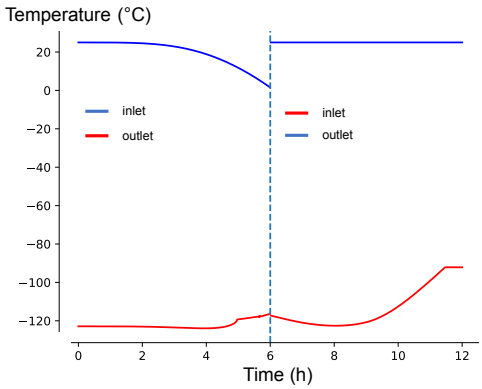

(d) Inlet and outlet temperature of the CR.

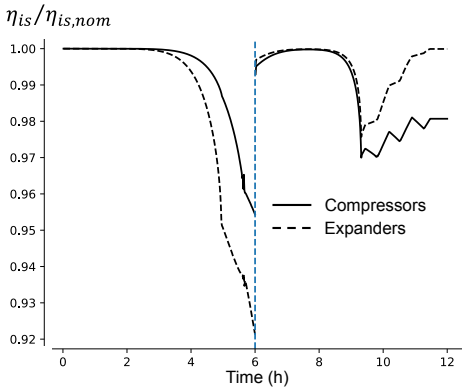

(e) Isentropic efficiencies of compressors and expanders.

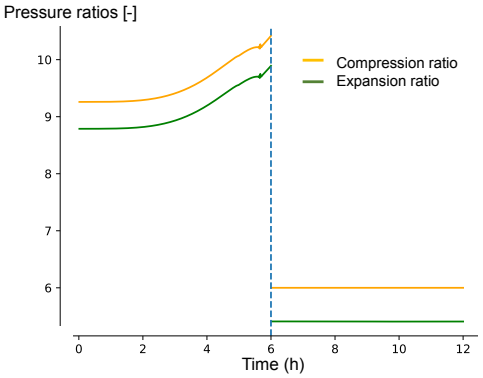

(f) Compression and expansion ratios.

Figure 5.6: Behavior of the PTES system over a full charging-discharging cycle with constant nominal power and varying mass flow rates and charging pressure ratios.

5.4.2 Including the LPHX in the charging loop

In the reference design presented in the chapter about the thermodynamic model (section 2.1), the LPHX is only present in the discharging loop while it is absent from the charging loop. However, some designs also consider the presence of the LPHX in the charging loop to keep the inlet temperature of the compressor (outlet of CR) constant when the outlet temperature of the CR starts decreasing. Most of them simply consider a rejection of cold from the working fluid to the atmosphere. However, this would require an ambient temperature always higher than $T_1 = 25[°C]$. Therefore, a most realistic design would include a heating system such as an electrical resistance (ER) as in the design proposed by Ameen et al. [59]. Including this electrical resistance allows to keep the inlet temperature of the compressor (CR outlet) constant, therefore keeping the compressor outlet temperature (HR inlet) constant while also keeping the compression ratio constant. This would however increase the energy input due to the electrical consumption of the ER.

Fig. 5.8 shows the evolution of the powers, mass flow rates, inlet and outlet temperatures of the HR and CR, isentropic efficiencies of the machines and compression/expansion ratios of the system throughout the whole 6h charge-6h discharge cycle. As expected, the inlet temperature of the HR (compressor outlet) remains constant during charging, even when the outlet temperature of the CR (compressor inlet) decreases. The outlet temperature of the HR (turbine inlet) is therefore higher and more stable during the discharge than in the ref-CPWR case, leading to a more stable output power. The other parameters during the discharge show the same trend as in the previous case with a constant compressor outlet temperature and varying compression ratio (CST-T2-β).

As it can be seen in table 5.5, including the LPHX with the ER in the charging loop gives raise to a significant improvement of $\tau_{P_{nom}}$, although less important than in the previous case without the ER and varying compression ratio. The round trip efficiency also shows a slight increase. The electrical consumption of the ER is 22 [kWh], which is relatively small compared to the total energy input of 1558 [kWh].

Performance metric	Ref-CPWR	CST-T2-ER	Unit
η_{rt}	30.3	31.8	%
$\tau_{P_{nom}}$	38.7	56.5	%
COP	1.29	1.30	-
η_{HE}	23.2	24.1	%
$P_{e,ch}$	255.3	255.3	kW
$P_{e,dc}$	88.4	89.0	kW
E_{input}	1536	1558	kWh_e
E_{output}	465	488	kWh_e
ρ_E	15.2	15.9	kWh_e/m^3

Table 5.5: Performances over a 6h charge-6h discharge cycle at nominal constant powers of the reference design case at constant charging compression ratio (Ref-CPWR) and constant compressor outlet temperature with an electrical resistance (CST-T2-ER).

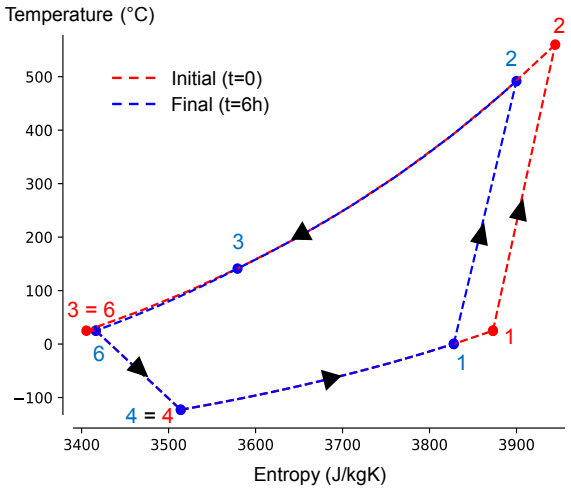

Figure 5.7: Initial and final charging T-s diagrams for the system operated at constant T_2 with an electrical resistance (CST-T2-ER). The ER allows to keep the cycle quasi-identical throughout the whole charge.

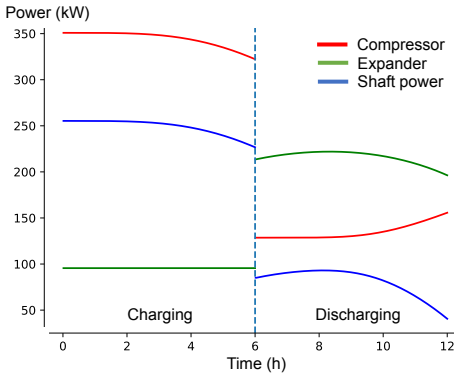

(a) Transient power.

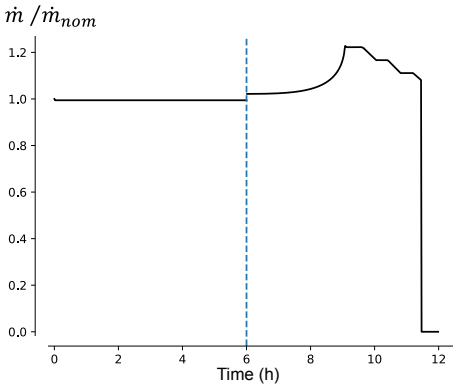

(b) Normalized mass flow rate $\frac{\dot{m}}{\dot{m}_{nom}}$.

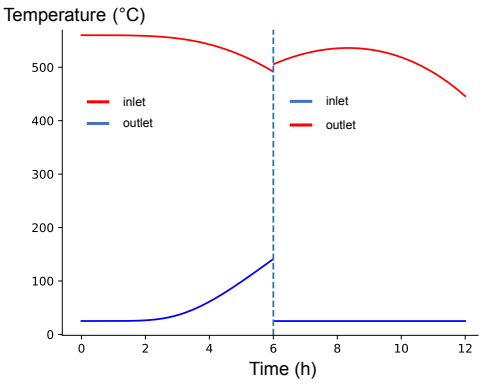

(c) Inlet and outlet temperatures of the HR.

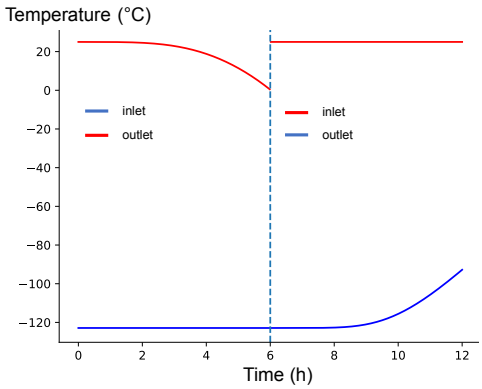

(d) Inlet and outlet temperature of the CR.

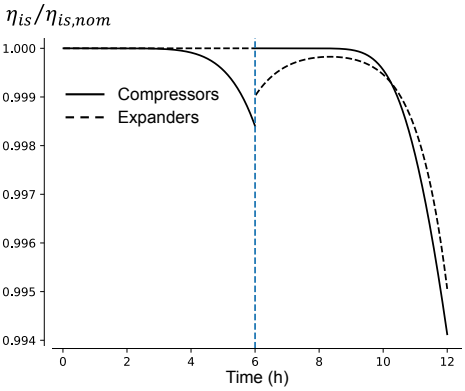

(e) Isentropic efficiencies of compressors and expanders.

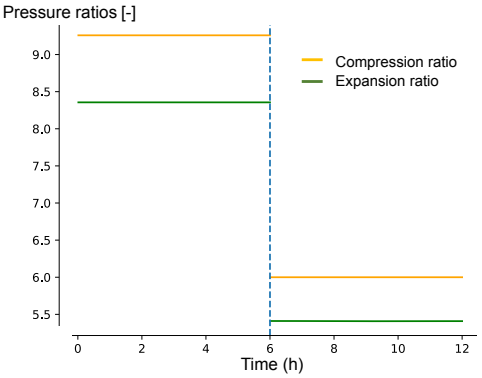

(f) Compression and expansion ratios.

Figure 5.8: Behavior of the PTES system over a full charging-discharging cycle with constant nominal power and varying mass flow rates and an electrical resistance in the charging loop.

5.5 Incomplete charge capabilities

In all the previous analysis of this thesis, the charge and discharge durations were both set to the nominal 6h duration. In this section, the performances of the nominal system (thus with the reservoirs volumes, energy capacity and mass flow rates kept constant) for equal charge and discharge duration of 1.5h, 3h and 4.5h are studied and compared with the nominal 6h case. In order to keep consistency with the other analysis of this chapter, the system is operated in constant power mode (CPWR) with constant compression ratios.

The results are shown in table 5.6. As it can be seen, the round trip efficiency is higher for charge/discharge times lower than the nominal one. The optimum between the 4 different cases displayed here is for t=3h. Again, the inlet/outlet temperatures of the compressor/expander during charge/discharge have an important role to play. Figs. 5.9a and 5.9b respectively show the HR inlet/outlet temperature during charge/discharge for the different charge-discharge durations studied and help better understand the following explanations.

For small durations as the 1.5h case, the phase at the end of charging when the compressor inlet (CR outlet) temperature decreases is avoided since the CR does not have enough time to discharge to this point, therefore keeping the outlet temperature of the compressor (HR inlet) constant. However, since the HR is only very partially charged, during the discharge, its outlet temperature (turbine inlet) directly decreases. For the 4.5h case, the charge is long enough to experience a non-negligible decrease in compressor inlet (CR outlet) temperature, therefore reducing the compressor outlet (HR inlet) temperature at the end of the charge, resulting in a lower HR outlet (turbine inlet) temperature at the beginning of the discharge. However, during discharge, as the HR is relatively full, the HR outlet (turbine inlet) temperature do not decrease before some time. The case with t=3h combines the advantages of the two other cases while minimizing the impact of the respective downsides. However, it is important to note that the differences in round trip efficiency between the three cases is relatively small and some part of it could also be explained by numerical imprecision due to the small durations of charge and discharge.

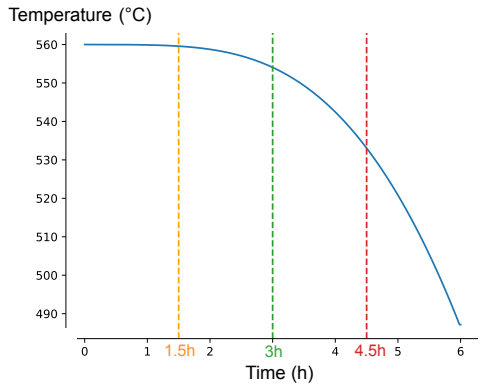

(a) HR inlet temperature during charging. The vertical lines indicate the time when the charging process ends for the different studied cases (1.5h, 3h, 4.5h). For each of the cases, the profile is thus the blue profile until the vertical line.

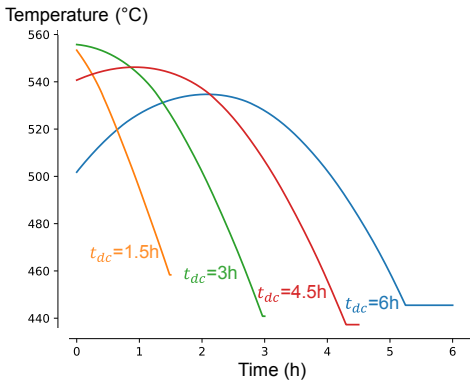

(b) HR outlet temperature during discharging for the different charge-discharge durations.

Figure 5.9: HR inlet/outlet temperature during charging/discharging for different charge-discharge durations.

Performance metric	**t=1.5h**	**t=3h**	**t=4.5h**	**Ref-CPWR**	**Unit**
η_{rt}	32.3	32.9	32.5	30.3	%
$\tau_{P_{nom}}$	30.0	44.1	51.0	38.7	%
COP	1.37	1.37	1.34	1.29	-
η_{HE}	22.3	23.2	23.6	23.2	%
$P_{e,ch}$	255.3	255.3	255.3	255.3	kW
$P_{e,dc}$	83.3	84.9	86.7	88.4	kW
E_{input}	387	770	1153	1536	kWh_e
E_{output}	125	253	374	465	kWh_e

Table 5.6: Performances for different charge-discharge durations at nominal constant powers. The Ref-CPWR case refers to the reference design for which t=6h.

5.6 Conclusions about operational considerations

A lot of conclusions and discussions can be drawn from the analyses of this chapter. The first one is that the Brayton PTES system of the reference design operated at constant compression ratio (and either constant or varying mass flow rate) shows a great lack of flexibility. When operated with a varying mass flow rate and keeping the other parameters at their design values, it is shown in section 5.1 that the part load capabilities of the system during charge are very limited.

During discharge, when operated in CMFR mode as in chapter 3, the power profile shows important variations and never reaches the nominal power. When operated in CPWR mode as done in this chapter (section 5.2), the system is only able to operate at nominal discharge power during less than 40 [%] of the discharge time.

In this thesis, the possible solutions to improve the part load capabilities during charge are not explored. Some solutions have already been proposed in the literature. Frate et al. [48] developed an efficient method to allow to operate the system as low as 40% of the nominal power without efficiency losses for both the charge and discharge, when the inlet temperatures of the machines and pressure ratios are kept constant. This is done by varying the pressure in the low-pressure part of the system in accordance with the variation of the mass flow rate. Since the off-design efficiency of the machines depends on the reduced mass flow rate $\frac{\dot{m}\sqrt{T_{in}}}{P_{in}}$ and the pressure ratio, it is possible to vary the mass flow rate and therefore the power while keeping the efficiency at its design point by adjusting the pressure with a buffer vessel.

Concerning the capacity of the system to operate at constant nominal power during discharge, different solutions are proposed and studied in this chapter to improve the performances of the system.

Two solutions relying on design parameters of the packed bed reservoirs are proposed, namely oversizing the reservoirs and increasing their length-to-diameter ratio. Oversizing the reservoirs results in substantial improvements of the system capabilities. However, oversizing the reservoirs raises the cost of the system and its space requirements. On the other hand, increasing the length-to-diameter ratio also brings some appreciable improvement while keeping the volume of the tanks constant.

Two other solutions based on the idea of maintaining a constant compressor outlet temperature (HR inlet) during charge are proposed. The first one is based on varying the compression ratio when the inlet temperature (CR outlet) decreases. The second one relies on the use of an electrical resistance between the CR outlet and the compressor inlet to warm the fluid when the CR outlet temperature decreases

and keep the compressor inlet temperature constant. Both method are found to improve significantly the constant nominal power capabilities of the system. The method with varying compression ratio still shows better results than the electrical resistance, increasing both $\tau_{P_{nom}}$ and η_{RT} in bigger extents. However, the maximum $\tau_{P_{nom}}$ is found to be 60.5 [%] for this solution, meaning that a non-negligible part of the discharge is still operated at a power lower than the nominal one.

With his approach of varying both the mass flow rate and low pressure of the system, Frate et al. [48] also found that the discharging cycle requires substantial mass flow rate and pressure adjustments to continue operating at the desired load level when the temperature at the reservoirs outlet vary.

The performances of the system for incomplete charge-discharge durations are also studied. It is found that for charge-discharge durations lower than the nominal ones, not only do the performances remain good but the round trip efficiency even increases for all the studied durations and $\tau_{P_{nom}}$ increases for durations of 3h and 4.5h. Frate et al. [48] also arrives to the conclusion that the use of reduced discharging phase durations could help avoiding the efficiency reduction due to the temperature variations at the reservoirs outlet.

Finally, it is noteworthy that all the analyses presented in this chapter are using the off design model of the compressors and expanders without considering the limitations of real machines. Indeed, when considering real machines, limitations such as the surge or choke restrain the conditions at which they can operate. The results shown in this chapter should therefore be verified with real machines characteristics in order to be validated.

CHAPTER 6

ECONOMIC DISCUSSION

The purpose of this chapter is to share a discussion on the economic aspects related to packed bed PTES both from the point of view of the literature and the intuitions related to thermodynamic analyses.
All the intuitions that are proposed are to be verified and the idea is not to draw conclusions on the basis of these intuitions.

6.1 Point of view of the literature

Until now, the vast majority of the literature about Brayton-based PTES has been focusing on large-scale systems. Estimating the costs for a small-scale system as the one in this thesis is therefore no easy task given that the costs between two scales are generally very disparate. As an example, the cost of storage at 10 $[MWh_t]$ and 100 $[MWh_t]$ presented by Allen et al. [60] goes respectively from 16.7[\$/kWh_t] to 7.7[\$/kWh_t]. Furthermore, Brayton-cycle PTES systems are still in the development stage, and there are several components that are not yet commercially available. As a result, there is limited data available on the investment costs associated with these systems. This section aims at reviewing the costs estimations provided by the literature for large-scale systems and individual components as well as highlighting the difficulties related to the estimation of these costs and their uncertainties.

Vecchi et al. (2022) [5] reviewed and compared the different packed-bed PTES systems present in the literature and the most recent commercial developments in Carnot Battery technologies. The main packed-bed PTES systems presented in

the review are shown in table 6.1.

For packed-bed Brayton-based PTES, the range of power specific cost and energy specific cost of the reviewed systems were found to be 470-6300 [$/kW] and 17–1570 [$/kWh]. These systems range in power from 2 to 10 [MW] and capacity from 2 to 40 [MWh]. These wide ranges of costs are explained by the different assumptions made by each study on the equipment involved but also the uncertainties on the cost of the components. For example, for the same system, Zhang, Wang, Lin et al. [38] found costs ranging from 460-1570 [$/kWh] and 1830-6300 [$/kW]. This shows that even for a given system, cost variations can be significant also due to variations in parameters (such as charge/discharge durations). In an attempt to compare the techno-economic aspects of packed bed and molten salts PTES, Olympios et al. [61] also noted that the use of different costing techniques leads to remarkably different estimates.

Author	Year	Energy specific cost [$/kWh$_e$]		Power specific cost [$/kW]		Power [MW]	Capacity [MWh$_{el}$]	Ref.
		min	MAX	min	MAX			
Howes	2012	17	17	470	470	2	16	[62]
Benato et al.	2017	57	203	-	-	1.7	2.72	[63]
Georgiou et al.	2018	530	1080	3000	6090	-	-	[64]
Zhang et al.	2021	460-640	1540-1570	1830-2570	6160-6300	10.0	40.0	[38]

Table 6.1: Energy and power capital costs from different studies

All of this highlights the fact that the large variety of cost functions used, the uncertainties about the costs, the choice of parameters for each study and the limited number of studies addressing the costs of packed bed PTES make it very difficult to express the capital cost of a system as a function of its power and capacity or evaluate the cost of a small-scale system.

In order to perform a plausible economic analysis, necessary for the development of Brayton PTES, reducing the uncertainties around their cost is crucial, as well as developing a more rigorous methodology to compare the different studies and power scales.

6.2 Point of view of the thermodynamic analysis

In this section, the economic insights gained from the thermodynamic and operational analysis carried out in the previous chapters are presented.

Considering the relatively lower round trip efficiency observed in this study compared to large-scale systems reported in the literature, the economic feasibility of small-scale Brayton PTES systems appears to be more challenging to attain. This intuition is reinforced by the fact that the cost of storage per unit energy

increases when decreasing the capacity of the storage [60]. Similarly, when the installed power decreases, there is a noticeable rise in the cost per unit of power for the machines [65].

Considering the quite important temperature constraints on the machines, it is easy to understand that their cost will be important and that it will drive the overall cost of the system since other components are less subject to constraints. Moreover, as the thermodynamic analysis has shown, the need to have machines with high isentropic efficiency also goes in this direction.
The literature often tends to take maximum temperatures for the hot reservoir quite high (such as 1000 [°C] in Zhang et al. [36]). Although these temperatures allow high efficiencies to be obtained, the temperature constraints on the machines seem complicated to satisfy especially in the case of small-scale machines where a cooling solution is difficult to imagine.
Moreover, the storage cost for this temperature range is likely to be quite high in view of the necessary isolation from the environment. Concerning the geometrical optimization of the storage, it is quite simple to understand that the surface/volume ratio must be minimized, as the losses are located at the walls of the tank. This optimization will be logically more important than at large scale.

Working on small-scale power/capacity seems to involve higher costs than on a large scale but may remain economically interesting if small-scale machines were more widely used and economies of scale would decrease the cost.

CONCLUSION

In this thesis, the thermodynamic numerical model of a Brayton cycle based Carnot battery with packed bed heat storage was constructed.

A design case with 100 [kW]/6 [h] nominal discharge power and charge/discharge durations was presented. Firstly, the behavior and performance of the system over a full charge-discharge cycle operated at constant mass flow rate were studied. It was shown that due to the temperature variations at the packed bed reservoirs outlets, the input/output powers and system performances experience important variations throughout the cycle. The output power never reaches the nominal power during discharge. The round trip efficiency was found to be 32.7 [%].

Parametric analysis were subsequently carried out to understand the impact of the different parameters on the system performances.

As already observed in the literature, the isentropic efficiency of the machines was found to have a significant impact on the round trip efficiency.

The length-to-diameter ratio of the packed bed reservoirs as well as the solid material particle diameter were found to have an influence on the round trip efficiency due to their effect on the pressure drops and thermal efficiencies of the reservoirs. However, the impact of the length-to-diameter ratio is relatively small while the effect of the particle diameter is more pronounced and their diameter can be lower than in large-scale applications due to the lower pressure losses.

Concerning the choice of working fluid, it was found that air should be preferred over argon, given its similar performances, lower cost and easier operation. Helium should be avoided given its poor performances.

Furthermore, an uncertainty analysis was carried out. The uncertainties associated with the properties of the solid material of the packed bed were found to have a negligible impact on the uncertainty of the round trip efficiency.

Some operational considerations were then studied. It was found that to date, the literature still lacks of researches and studies about the operational limitations and control strategies of packed bed PTES. The part load capabilities of the system during charge were found to be very limited. During discharge, the system demonstrated ability to operate at constant nominal power only 38.7 [%] of the time. The rest of the time, the power is limited by a maximum power curve.

The solutions to improve the part load capabilities were not studied but some solutions proposed in the literature were reviewed.

Some solutions to extend the duration at which the system is able to operate at nominal power during discharge were proposed and studied. It was found that oversizing the packed bed reservoirs as well as increasing their length-to-diameter ratio leads to significant improvements. Two solutions based on the idea of keeping a constant compressor outlet temperature during charge were also proposed, namely varying the compression ratio or including the LPHX with an electrical resistance in the charging loop. Both techniques led to appreciable improvements of the discharge time operated at nominal power, with the varying compression ratio yielding the best results.

The performance of the system for incomplete charges was analyzed. The results showed that for incomplete charge cycles, the round trip efficiency is improved. For charge-discharge durations of 3 hours and longer, the time operated at nominal power during discharge was also found to be enhanced.

Finally, a discussion about the economic aspect of packed bed PTES was carried out. The high level of uncertainty about the cost of these systems was highlighted. Additionally, the need for a common basis and methodology to compare cost estimations was put forward.

From the conclusions drawn from this thesis, several future lines of research could be developed. The development of methodologies for more precise and rigorous cost estimations would allow to reduce the uncertainties around the economics of the technology. This would allow to study if, in view of its low round trip efficiency, the system could still be competitive with other types of storage technologies. Future work should also focus on the study of the operational control strategies of the system as well as their physical implementation, especially since the operational limitations deduced from this thesis should also apply to large-scale systems. Finally, a study of different possible integration scenarios of the technology in the energy system would help understand in which applications they could be techno-economically attractive.

BIBLIOGRAPHY

[1] "Doe global energy storage database," http://www.energystorageexchange.org/projects/data_visualization/, accessed: 2023-28-05.

[2] F. Cebulla, J. Haas, J. Eichman, W. Nowak, and P. Mancarella, "How much electrical energy storage do we need? a synthesis for the u.s., europe, and germany," *Journal of Cleaner Production*, vol. 181, pp. 449–459, 2018. [Online]. Available: https://www.sciencedirect.com/science/article/pii/S0959652618301665

[3] A. Benato and A. Stoppato, "Pumped thermal electricity storage: A technology overview," *Thermal Science and Engineering Progress*, vol. 6, pp. 301–315, 2018. [Online]. Available: https://www.sciencedirect.com/science/article/pii/S2451904917303700

[4] X. Luo, J. Wang, M. Dooner, and J. Clarke, "Overview of current development in electrical energy storage technologies and the application potential in power system operation," *Applied Energy*, vol. 137, pp. 511–536, 2015. [Online]. Available: https://www.sciencedirect.com/science/article/pii/S0306261914010290

[5] A. Vecchi, K. Knobloch, T. Liang, H. Kildahl, A. Sciacovelli, K. Engelbrecht, Y. Li, and Y. Ding, "Carnot battery development: A review on system performance, applications and commercial state-of-the-art," *Journal of Energy Storage*, vol. 55, p. 105782, 2022. [Online]. Available: https://www.sciencedirect.com/science/article/pii/S2352152X22017704

[6] T. Liang, A. Vecchi, K. Knobloch, A. Sciacovelli, K. Engelbrecht, Y. Li, and Y. Ding, "Key components for carnot battery: Technology review, technical barriers and selection criteria," *Renewable and Sustainable*

Energy Reviews, vol. 163, p. 112478, 2022. [Online]. Available: https://www.sciencedirect.com/science/article/pii/S1364032122003823

[7] O. Dumont, G. F. Frate, A. Pillai, S. Lecompte, M. De paepe, and V. Lemort, "Carnot battery technology: A state-of-the-art review," *Journal of Energy Storage*, vol. 32, p. 101756, 2020. [Online]. Available: https://www.sciencedirect.com/science/article/pii/S2352152X20315930

[8] S. Staub, P. Bazan, K. Braimakis, D. Müller, C. Regensburger, D. Scharrer, B. Schmitt, D. Steger, R. German, S. Karellas, M. Pruckner, E. Schlücker, S. Will, and J. Karl, "Reversible heat pump–organic rankine cycle systems for the storage of renewable electricity," *Energies*, vol. 11, no. 6, 2018. [Online]. Available: https://www.mdpi.com/1996-1073/11/6/1352

[9] J. Howes, "Concept and development of a pumped heat electricity storage device," *Proceedings of the IEEE*, vol. 100, no. 2, pp. 493–503, 2012.

[10] A. Smallbone, V. Jülch, R. Wardle, and A. P. Roskilly, "Levelised cost of storage for pumped heat energy storage in comparison with other energy storage technologies," *Energy Conversion and Management*, vol. 152, pp. 221–228, 2017. [Online]. Available: https://www.sciencedirect.com/science/article/pii/S0196890417308713

[11] V. Novotny, V. Basta, P. Smola, and J. Spale, "Review of carnot battery technology commercial development," *Energies*, vol. 15, no. 2, 2022. [Online]. Available: https://www.mdpi.com/1996-1073/15/2/647

[12] G. F. Frate, L. Ferrari, and U. Desideri, "Techno-economic comparison of brayton pumped thermal electricity storage (ptes) systems based on solid and liquid sensible heat storage," *Energies*, vol. 15, no. 24, 2022. [Online]. Available: https://www.mdpi.com/1996-1073/15/24/9595

[13] M. Mercangöz, J. Hemrle, L. Kaufmann, A. Z'Graggen, and C. Ohler, "Electrothermal energy storage with transcritical co2 cycles," *Energy*, vol. 45, no. 1, pp. 407–415, 2012, the 24th International Conference on Efficiency, Cost, Optimization, Simulation and Environmental Impact of Energy, ECOS 2011. [Online]. Available: https://www.sciencedirect.com/science/article/pii/S0360544212002046

[14] S. SAVÀ, "Joule-brayton pumped thermal electricity storage based on packed beds," 2021.

[15] M. Morandin, F. Maréchal, M. Mercangöz, and F. Buchter, "Conceptual design of a thermo-electrical energy storage system based on heat

integration of thermodynamic cycles – part a: Methodology and base case," *Energy*, vol. 45, no. 1, pp. 375–385, 2012, the 24th International Conference on Efficiency, Cost, Optimization, Simulation and Environmental Impact of Energy, ECOS 2011. [Online]. Available: https://www.sciencedirect.com/science/article/pii/S0360544212002228

[16] Y.-M. Kim, D.-G. Shin, S.-Y. Lee, and D. Favrat, "Isothermal transcritical co2 cycles with tes (thermal energy storage) for electricity storage," *Energy*, vol. 49, pp. 484–501, 2013. [Online]. Available: https://www.sciencedirect.com/science/article/pii/S0360544212007360

[17] F. Ayachi, N. Tauveron, T. Tartière, S. Colasson, and D. Nguyen, "Thermo-electric energy storage involving co2 transcritical cycles and ground heat storage," *Applied Thermal Engineering*, vol. 108, pp. 1418–1428, 2016. [Online]. Available: https://www.sciencedirect.com/science/article/pii/S1359431116311942

[18] W. Steinmann, "The chest (compressed heat energy storage) concept for facility scale thermo mechanical energy storage," *Energy*, vol. 69, pp. 543–552, 2014. [Online]. Available: https://www.sciencedirect.com/science/article/pii/S0360544214003132

[19] H. Gu, Y. Chen, X. Yao, L. Huang, and D. Zou, "Review on heat pump (hp) coupled with phase change material (pcm) for thermal energy storage," *Chemical Engineering Journal*, vol. 455, p. 140701, 2023. [Online]. Available: https://www.sciencedirect.com/science/article/pii/S1385894722061812

[20] R. Jacob and M. Liu, "Design and evaluation of a high temperature phase change material carnot battery," *Energies*, vol. 16, no. 1, 2023. [Online]. Available: https://www.mdpi.com/1996-1073/16/1/189

[21] T. Desrues, J. Ruer, P. Marty, and J. Fourmigué, "A thermal energy storage process for large scale electric applications," *Applied Thermal Engineering*, vol. 30, no. 5, pp. 425–432, 2010. [Online]. Available: https://www.sciencedirect.com/science/article/pii/S1359431109002932

[22] J. D. McTigue, A. J. White, and C. N. Markides, "Parametric studies and optimisation of pumped thermal electricity storage," *Applied Energy*, vol. 137, pp. 800–811, 2015. [Online]. Available: https://www.sciencedirect.com/science/article/pii/S0306261914008423

[23] R. B. Laughlin, "Pumped thermal grid storage with heat exchange," *Journal of Renewable and Sustainable Energy*, vol. 9, no. 4, 08 2017, 044103. [Online]. Available: https://doi.org/10.1063/1.4994054

[24] A. Benato and A. Stoppato, "Heat transfer fluid and material selection for an innovative pumped thermal electricity storage system," *Energy*, vol. 147, pp. 155–168, 2018. [Online]. Available: https://www.sciencedirect.com/science/article/pii/S0360544218300562

[25] L. Wang, X. Lin, L. Chai, L. Peng, D. Yu, and H. Chen, "Cyclic transient behavior of the joule–brayton based pumped heat electricity storage: Modeling and analysis," *Renewable and Sustainable Energy Reviews*, vol. 111, pp. 523–534, 2019. [Online]. Available: https://www.sciencedirect.com/science/article/pii/S1364032119301960

[26] L. Wang, X. Lin, L. Chai, L. Peng, D. Yu, J. Liu, and H. Chen, "Unbalanced mass flow rate of packed bed thermal energy storage and its influence on the joule-brayton based pumped thermal electricity storage," *Energy Conversion and Management*, vol. 185, pp. 593–602, 2019. [Online]. Available: https://www.sciencedirect.com/science/article/pii/S0196890419302043

[27] P. Sapin, M. C. Simpson, A. V. Olympios, M. Mersch, and C. N. Markides, "Cost-benefit analysis of reversible reciprocating-piston engines with adjustable volume ratio in pumped thermal electricity storage," 2020, Conference paper, p. 1534 – 1545, cited by: 3. [Online]. Available: https://www.scopus.com/inward/record.uri?eid=2-s2.0-85095765452&partnerID=40&md5=b7167beb09d3b405c51d4223f9fd2439

[28] T. R. Davenne and B. M. Peters, "An analysis of pumped thermal energy storage with de-coupled thermal stores," *Frontiers in Energy Research*, vol. 8, 2020. [Online]. Available: https://www.frontiersin.org/articles/10.3389/fenrg.2020.00160

[29] J. D. McTigue, P. Farres-Antunez, K. S. J, C. N. Markides, and A. J. White, "Techno-economic analysis of recuperated joule-brayton pumped thermal energy storage," *Energy Conversion and Management*, vol. 252, p. 115016, 2022. [Online]. Available: https://www.sciencedirect.com/science/article/pii/S0196890421011924

[30] D. Salomone-González, J. González-Ayala, A. Medina, J. Roco, P. Curto-Risso, and A. Calvo Hernández, "Pumped heat energy storage with liquid media: Thermodynamic assessment by a brayton-like model," *Energy Conversion and Management*, vol. 226, p. 113540, 2020. [Online]. Available: https://www.sciencedirect.com/science/article/pii/S0196890420310694

[31] H. Zhou, Z. Lai, and K. Cen, "Experimental study on energy storage performances of packed bed with different solid materials," *Energy*, vol. 246,

p. 123416, 2022. [Online]. Available: https://www.sciencedirect.com/science/article/pii/S036054422200319X

[32] E. Oró, A. Gil, A. de Gracia, D. Boer, and L. F. Cabeza, "Comparative life cycle assessment of thermal energy storage systems for solar power plants," *Renewable Energy*, vol. 44, pp. 166–173, 2012. [Online]. Available: https://www.sciencedirect.com/science/article/pii/S0960148112000195

[33] M. Goedkoop and R. Spriensma, "The eco-indicator 99: A damage oriented method for life cycle impact assessment," 01 2001.

[34] Y. Wickramasinghe and L. Zhang, "Life cycle assessment of sensible, latent and thermochemical thermal energy storage systems for climate change mitigation -a systematic review," *Journal of Energy Technologies and Policy*, vol. 12, pp. 17–31, 11 2022.

[35] T. Nahhas, X. Py, and R. Olives, "Life cycle assessment of air-rock packed bed storage system and its comparison with other available storage technologies for concentrating solar power plants," *Waste and Biomass Valorization*, vol. 11, no. 5, pp. 2357–2365, dec 2018. [Online]. Available: https://doi.org/10.1007%2Fs12649-018-0529-x

[36] H. Zhang, L. Wang, X. Lin, and H. Chen, "Parametric optimisation and thermo-economic analysis of joule–brayton cycle-based pumped thermal electricity storage system under various charging–discharging periods," *Energy*, vol. 263, p. 125908, 2023. [Online]. Available: https://www.sciencedirect.com/science/article/pii/S0360544222027943

[37] L. Wang, X. Lin, H. Zhang, L. Peng, X. Zhang, and H. Chen, "Analytic optimization of joule–brayton cycle-based pumped thermal electricity storage system," *Journal of Energy Storage*, vol. 47, p. 103663, 2022. [Online]. Available: https://www.sciencedirect.com/science/article/pii/S2352152X21013384

[38] H. Zhang, L. Wang, X. Lin, and H. Chen, "Technical and economic analysis of brayton-cycle-based pumped thermal electricity storage systems with direct and indirect thermal energy storage," *Energy*, vol. 239, p. 121966, 2022. [Online]. Available: https://www.sciencedirect.com/science/article/pii/S0360544221022143

[39] T. R. Davenne and B. M. Peters, "An analysis of pumped thermal energy storage with de-coupled thermal stores," *Frontiers in Energy Research*, vol. 8, 2020. [Online]. Available: https://www.frontiersin.org/articles/10.3389/fenrg.2020.00160

[40] M. Hänchen, S. Brückner, and A. Steinfeld, "High-temperature thermal storage using a packed bed of rocks – heat transfer analysis and experimental validation," *Applied Thermal Engineering*, vol. 31, no. 10, pp. 1798–1806, 2011. [Online]. Available: https://www.sciencedirect.com/science/article/pii/S1359431111001062

[41] J. Coutier and E. Farber, "Two applications of a numerical approach of heat transfer process within rock beds," *Solar Energy*, vol. 29, no. 6, pp. 451–462, 1982. [Online]. Available: https://www.sciencedirect.com/science/article/pii/0038092X82900536

[42] "High-Level Interface — CoolProp 6.4.3 documentation." [Online]. Available: http://www.coolprop.org/coolprop/HighLevelAPI.html

[43] S. Ergun, "Fluid flow through packed columns," 1952.

[44] O. Dumont, A. Parthoens, R. Dickes, and V. Lemort, "Experimental investigation and optimal performance assessment of four volumetric expanders (scroll, screw, piston and roots) tested in a small-scale organic rankine cycle system," *Energy*, vol. 165, pp. 1119–1127, 2018. [Online]. Available: https://www.sciencedirect.com/science/article/pii/S0360544218312477

[45] W. Wang, R. Cai, and N. Zhang, "General characteristics of single shaft microturbine set at variable speed operation and its optimization," *Appl. Therm. Eng.*, vol. 24, no. 13, pp. 1851–1863, Sep. 2004.

[46] R. Tassenoy, K. Couvreur, W. Beyne, M. De Paepe, and S. Lecompte, "Techno-economic assessment of carnot batteries for load-shifting of solar pv production of an office building," *Renewable Energy*, vol. 199, pp. 1133–1144, 2022. [Online]. Available: https://www.sciencedirect.com/science/article/pii/S0960148122013891

[47] M. Montero Carrero, *Decoupling heat and electricity production from micro gas turbines: numerical, experimental and economic analysis of the micro humid air turbine cycle (Unpublished doctoral dissertation)*, Bruxelles, 2018.

[48] G. F. Frate, L. Paternostro, L. Ferrari, and U. Desideri, "Off-Design of a Pumped Thermal Energy Storage Based on Closed Brayton Cycles," *Journal of Engineering for Gas Turbines and Power*, vol. 144, no. 2, 11 2021, 021016. [Online]. Available: https://doi.org/10.1115/1.4052426

[49] P. F. C. A. Laterre, "Towards dynamic modelling of micro gas turbines,ecole polytechnique de louvain," 2021. [Online]. Available: http://hdl.handle.net/2078.1/thesis:30651

[50] X. Xue and C. Zhao, "Transient behavior and thermodynamic analysis of brayton-like pumped-thermal electricity storage based on packed-bed latent heat/cold stores," *Applied Energy*, vol. 329, p. 120274, 2023. [Online]. Available: https://www.sciencedirect.com/science/article/pii/S0306261922015318

[51] L. Li and W. Ma, "Experimental study on the effective particle diameter of a packed bed with non-spherical particles," *Transp. Porous Media*, vol. 89, no. 1, pp. 35–48, Aug. 2011.

[52] Y. Zhao, J. Song, M. Liu, K. Zhang, C. N. Markides, and J. Yan, "Multi-objective thermo-economic optimisation of joule-brayton pumped thermal electricity storage systems: Role of working fluids and sensible heat storage materials," *Applied Thermal Engineering*, vol. 223, p. 119972, 2023. [Online]. Available: https://www.sciencedirect.com/science/article/pii/S1359431123000017

[53] K. Knobloch, T. Ulrich, C. Bahl, and K. Engelbrecht, "Degradation of a rock bed thermal energy storage system," *Applied Thermal Engineering*, vol. 214, p. 118823, 2022. [Online]. Available: https://www.sciencedirect.com/science/article/pii/S1359431122007633

[54] K. Allen, T. von Backström, and D. Kröger, "Packed bed pressure drop dependence on particle shape, size distribution, packing arrangement and roughness," *Powder Technology*, vol. 246, pp. 590–600, 2013. [Online]. Available: https://www.sciencedirect.com/science/article/pii/S0032591013004312

[55] A. Ege and H. M. Şahin, "Uncertainties in energy and exergy efficiency of a high pressure turbine in a thermal power plant," *International Journal of Hydrogen Energy*, vol. 41, no. 17, pp. 7197–7205, 2016, special Issue on 17th International Conference on Emerging Nuclear Energy Systems (ICENES'2015), 4-8 October 2015, Istanbul, Turkey. [Online]. Available: https://www.sciencedirect.com/science/article/pii/S0360319915314890

[56] M. Erdogan, U. Bau, and A. Bardow, "Benchmarking commercial adsorbents for drying air in a packed bed," *Applied Thermal Engineering*, vol. 160, p. 113942, 2019. [Online]. Available: https://www.sciencedirect.com/science/article/pii/S1359431119306556

[57] J. Lambert and L. Gosselin, "Sensitivity analysis of heat exchanger design to uncertainties of correlations," *Applied Thermal Engineering*, vol. 136, pp. 531–540, 2018. [Online]. Available: https://www.sciencedirect.com/science/article/pii/S1359431117348925

[58] H. Zhang, L. Wang, X. Lin, and H. Chen, "Operating mode of brayton-cycle-based pumped thermal electricity storage system: Constant compression ratio or constant rotational speed?" *Applied Energy*, vol. 343, p. 121107, 2023. [Online]. Available: https://www.sciencedirect.com/science/article/pii/S0306261923004713

[59] M. T. Ameen, Z. Ma, A. Smallbone, R. Norman, and A. P. Roskilly, "Demonstration system of pumped heat energy storage (phes) and its round-trip efficiency," *Applied Energy*, vol. 333, p. 120580, 2023. [Online]. Available: https://www.sciencedirect.com/science/article/pii/S0306261922018372

[60] K. Allen, T. von Backström, E. Joubert, and P. Gauché, "Rock bed thermal storage: Concepts and costs," *AIP Conference Proceedings*, vol. 1734, no. 1, 05 2016, 050003. [Online]. Available: https://doi.org/10.1063/1.4949101

[61] A. Olympios, J. McTigue, P. Sapin, and C. Markides, *Pumped-Thermal Electricity Storage Based on Brayton Cycles*, 07 2021.

[62] J. Howes, "Concept and development of a pumped heat electricity storage device," *Proc. IEEE Inst. Electr. Electron. Eng.*, vol. 100, no. 2, pp. 493–503, Feb. 2012.

[63] A. Benato, "Performance and cost evaluation of an innovative pumped thermal electricity storage power system," *Energy*, vol. 138, pp. 419–436, 2017. [Online]. Available: https://www.sciencedirect.com/science/article/pii/S0360544217312422

[64] S. Georgiou, N. Shah, and C. N. Markides, "A thermo-economic analysis and comparison of pumped-thermal and liquid-air electricity storage systems," *Applied Energy*, vol. 226, pp. 1119–1133, 2018. [Online]. Available: https://www.sciencedirect.com/science/article/pii/S0306261918306627

[65] R. Banihabib and M. Assadi, "The role of micro gas turbines in energy transition," *Energies*, vol. 15, no. 21, 2022. [Online]. Available: https://www.mdpi.com/1996-1073/15/21/8084

Appendices

APPENDIX A

PERFORMANCE MAP FOR THE CST-T2-β CASE

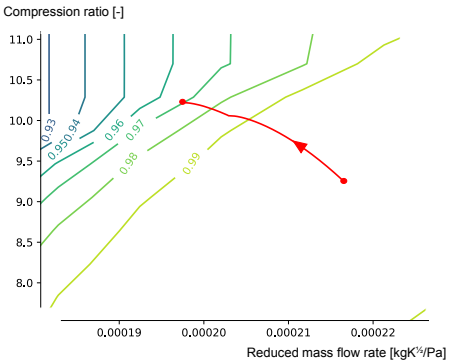

(a) Red line corresponds to the compressor isentropic variation during the charging phase, red arrow show the time evolution.

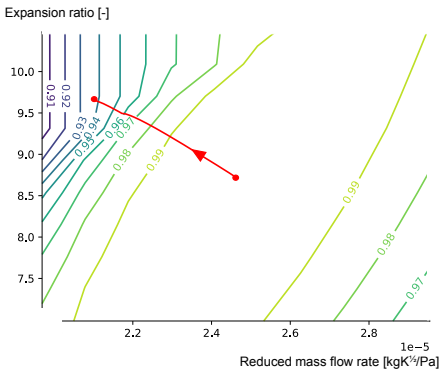

(b) Red line corresponds to the expander isentropic variation during the charging phase,red arrow show the time evolution.

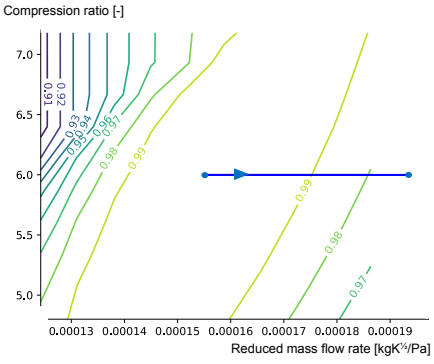

(c) Blue line corresponds to the compressor isentropic variation during the discharging phase,blue arrow show the time evolution.

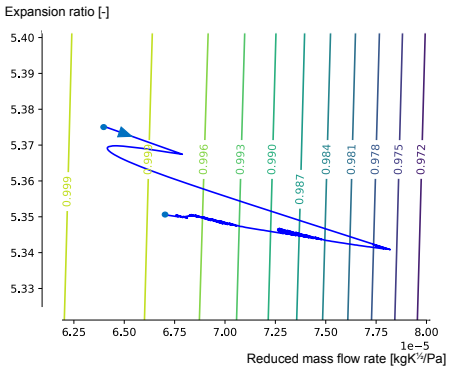

(d) Blue line corresponds to the expander isentropic variation during the discharging phase,blue arrow show the time evolution. The map is zoomed in order to be able to visualize the slight variations of expansion ratio.

UNIVERSITÉ CATHOLIQUE DE LOUVAIN
École polytechnique de Louvain
Rue Archimède, 1 bte L6.11.01, 1348 Louvain-la-Neuve, Belgique | **www.uclouvain.be/epl**